Deeply Virtual Compton Scattering off Longitudinally Polarised Protons at HERMES

David Francis Mahon

A thesis presented for the degree of

Doctor of Philosophy

University of Glasgow

Nuclear Physics Experimental Research Group
Department of Physics & Astronomy
University of Glasgow
Scotland

March 2010

Deeply Virtual Compton Scattering off Longitudinally Polarised Protons at HERMES

David Francis Mahon

Submitted for the degree of Doctor of Philosophy

March 2010

Abstract

This thesis details the simultaneous extraction of three polarisation-dependent asymmetries in the distribution of real photons from the $e\,p \to e\,p\,\gamma$ interaction and its indistinguishable deeply virtual Compton scattering and Bethe-Heitler processes at the HERMES fixed-target experiment at DESY. The data analysed were taken using a longitudinally polarised $27.57\,\mathrm{GeV}$ positron beam incident on a longitudinally polarised hydrogen gas target. The extracted asymmetries include two single-spin asymmetries $\mathcal{A}_{\mathrm{UL}}$ and $\mathcal{A}_{\mathrm{LU}}$ which depend on the polarisation of the target and beam respectively, averaged over all other polarisation states. The double-spin asymmetry $\mathcal{A}_{\mathrm{LL}}$ dependent on the product of the beam and target polarisations is extracted for the first time.

The asymmetry amplitudes extracted relate to combinations of Generalised Parton Distributions (GPDs), predominantly $\widetilde{H}$ and H. The extracted amplitudes will be presented across the HERMES kinematic range alongside theoretical predictions from a GPD model based on double distributions.

Large $\sin\phi$ and $\cos(0\phi)$ amplitudes are observed for $\mathcal{A}_{\mathrm{UL}}$ and $\mathcal{A}_{\mathrm{LL}}$ respectively, with an unexpectedly large $\sin(2\phi)$ amplitude for $\mathcal{A}_{\mathrm{UL}}$. The results for the $\mathcal{A}_{\mathrm{UL}}$ and $\mathcal{A}_{\mathrm{LL}}$ asymmetries are broadly compatible with theory predictions, and the extracted $\mathcal{A}_{\mathrm{LU}}$ amplitudes are compatible with HERMES results extracted from a significantly larger data set.

It is foreseen that these results will form input to future global data-based GPD models which aim to provide a better understanding of GPDs.

Declaration

The work in this thesis is based on research carried out at the Nuclear Physics Experimental Research Group, Department of Physics & Astronomy, University of Glasgow, Scotland. No part of this thesis has been submitted elsewhere for any other degree or qualification and is all my own work unless referenced to the contrary in the text.

Acknowledgements

I have thoroughly enjoyed my Ph.D. experience and that is, in no small part, down to the following people.

First of all I'd like to thank my supervisors, Prof. Ralf Kaiser and Dr. Bjoern Seitz. Over the last four years, their help and support has given me the opportunity to travel to some great places, and during this time, I have acquired skills which will undoubtedly benefit me in the future. Thanks also to Prof. Guenther Rosner for offering me a Ph.D. in the Nuclear Physics Experimental group in the first place, and for insisting I accept one of the HERMES positions.

I am indebted to Gordon Hill for his continuous help and ever-willing support throughout my Ph.D., but especially during the early stages. My development as a physicist and programmer has benefitted greatly from working alongside him. Cheers Dr. Hill.

During these first couple of years, and my long spells in Hamburg, I also worked closely with Sergey Yaschenko, Caroline Riedl and Aram Movsisyan. I'd like to thank them all for their help and advice at various stages of my analysis. I'd also like to thank the other members of the HERMES DVCS group, and everyone involved with DC80, for their ideas, suggestions and comments during my analysis and the drafting of our paper. Although at times this process was frustrating, I am in no doubt that my thesis is better off for it.

A great deal of thanks must also go to the other Hermesians in Glasgow: Jennifer Bowles, Jonathan Burns, Inti Lehmann and Morgan Murray. I consider myself extremely fortunate that I was able to share this experience with Jonathan. Not only did his company make my time in Hamburg a lot more bearable, but the discussions we had, analysis-related or otherwise, were invaluable. Thanks to Morgan for not only enduring the drafting experience with me, but for expanding my theoretical understanding and for proof-reading this thesis along with Gordon, Ralf and Inti.

I'm privileged to have shared an office with a lot of people over the last four years. Special thanks go to Neil "The Ride" Thompson, Richard Codling, David "Burger" Howdle, Neil

Contents

List of Figures

List of Tables

Chapter 1

Introduction

Since Dennison's discovery of the spin $\frac{1}{2}$ property of the proton [1], there has been a lot of experimental activity aimed at understanding its complex spin structure. Spin, the intrinsic angular momentum, is one of the fundamental properties of the nucleon. It can be decomposed into contributions from its constituent partons [2] *i.e.* quarks and gluons, in the Ji interpretation [3] as

$$\frac{1}{2} = \underbrace{\frac{1}{2}\overbrace{(\Delta u + \Delta d + \Delta s)}^{\Delta \Sigma} + L_q}_{J_q} + J_{\mathrm{g}}, \tag{1.1}$$

where $\Delta \Sigma$ (L_q) represents the contributions from the spin (orbital angular momenta) of the spin $\frac{1}{2}$ quarks. Here, J_q and J_{g} denote the total angular momenta of the quarks and the spin 1 gluons respectively. In the Jaffe-Manohar decomposition [4,5], J_{g} is thought to consist of contributions from the orbital angular momenta of the gluons L_{g} and the sum of their spins ΔG. The definitions of L_q are shown to differ between the two approaches [6]. These nucleon spin contributions are illustrated in Fig. 1.1.

Interest was sparked when the European Muon Collaboration (EMC) at CERN published measurements of the spin-dependent structure function g_1 and constituent quark decompositions of the proton spin [7,8]. These results suggested the sum of the spin contributions from the u, d and s valence quarks was compatible with zero, in contradiction with relativistic constituent quark models which predicted a value of $\simeq 60\%$.

The HERMES Collaboration [9] was formed to resolve the 'Spin Crisis' [10] that arose from these EMC findings. HERMES published complementary, precise measurements of the total quark spin contribution $\Delta \Sigma$ [11] and the contribution from individual constituent quark flavours, *i.e.* $(\Delta u + \Delta d + \Delta s)$ [12], which showed the quark spin contribution to be
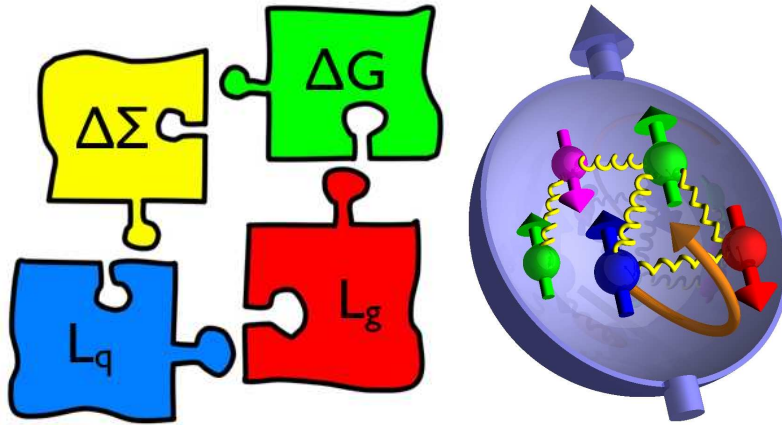
Figure 1.1: (left): Spin Puzzle diagram [13] showing the contributions to the nucleon spin from the orbital angular momenta of the quarks and gluons, L_q and L_g respectively, and from the sums of their intrinsic spins, $\Delta\Sigma$ and ΔG. (right): Representation of the partonic structure of the nucleon [14].

$\simeq 33\%$ of the total proton spin.

The most promising way to investigate the subsequent 'Spin Puzzle' was postulated by Xiangdong Ji [3] in his relation between the total angular momentum $J_q\,(J_\mathrm{g})$ of quarks (gluons) in the nucleon and quark spin $\frac{1}{2}$ (gluon spin 1) Generalised Parton Distributions [15–19] H and E. These 'GPDs' provide the possibility to experimental access the quark contribution L_q via Eq. 1.1.

The simplest way to access information on GPDs is through Deeply Virtual Compton Scattering (DVCS) *i.e.* the hard exclusive leptoproduction of a real photon, represented by $e\,p \to e\,p\,\gamma$. The Bethe-Heitler (BH) process has identical initial and final states as DVCS and as a result both are experimentally indistinguishable. Useful GPD-related information arises via the consequent interference term in the $e\,p \to e\,p\,\gamma$ cross-section. This can be accessed by forming asymmetries in the distribution of real photons with respect to the azimuthal angle between the scattering and photoproduction planes.

HERMES has published results of DVCS-related asymmetries from a variety of gaseous targets [20–25] providing valuable input for future global GPD models based on experimental data. These measurements will be used alongside results from other DVCS experiments to help provide further insight into the spin structure of the nucleon.

This thesis will outline the theoretical framework of GPDs and some of their relations to known distributions in Chapter 2. The GPD model used for comparison with the results presented in this thesis, will also be introduced. In Chapter 3, the $e\,p \to e\,p\,\gamma$ process

will be detailed. Three polarisation-dependent asymmetries in the cross-section will be examined for positron scattering on a longitudinally polarised proton target. These are sensitive in particular to GPDs H and $\widetilde{H}$. The HERMES experimental setup will be outlined in Chapter 4 with detailed descriptions of the relevant detector components vital for this analysis.

The experimental data selection and asymmetry extraction method will be presented in Chapter 5. Chapter 6 details the numerous contributions to the systematic uncertainty and the steps taken to account for them. All steps in the analytical procedure will be detailed in these two chapters. Final results will be presented in Chapter 7 alongside theoretical predictions from the GPD model previously discussed. There will be detailed discussion of these results, their relationship to GPDs, and comparison with previous measurements.

Chapter 2

Generalised Parton Distributions

The internal structure of the nucleon is conventionally described in terms of Parton Distribution Functions (PDFs) and nucleon Form Factors (FFs). These PDFs outline the probability of having a parton (*i.e.* quark or gluon) with longitudinal momentum fraction x in the 'infinite' momentum frame of the nucleon. Form factors convey information on the spatial charge distribution in the transverse plane. This is characterised by the impact parameter $r_\perp$, defined as the distance from the centre of mass of the nucleon. Information on both PDFs and FFs can be obtained from Deep Inelastic Scattering (DIS) and elastic scattering experiments respectively.

A more comprehensive description of nucleon structure has emerged within the framework of Generalised Parton Distributions (GPDs). These are considered to be an amalgamation of PDFs and FFs, providing a multi-dimensional description of the partonic structure of the nucleon. This chapter will investigate these relationships, illustrated in Fig. 2.1, and introduce the relevant GPDs which are central to the analysis presented in this thesis.

2.1 Useful DIS Variable Definitions for GPDs

When considering DIS of an electron or positron (e) off a proton target (p) *i.e.*

$$e\left(\mathbf{k}\right) p\left(\mathbf{p}\right) \overset{\gamma^*(\mathbf{q})}{\to} e\left(\mathbf{k}'\right) X \,, \tag{2.1}$$

where X represents all final state products, it is important to define several kinematic quantities. These are used to describe the process and are calculable from the four-momenta of the incoming $\mathbf{k}$ and scattered $\mathbf{k}'$ leptons, the target proton $\mathbf{p}$ and the virtual photon (γ^*) $\mathbf{q}$ which couples to the target.

4
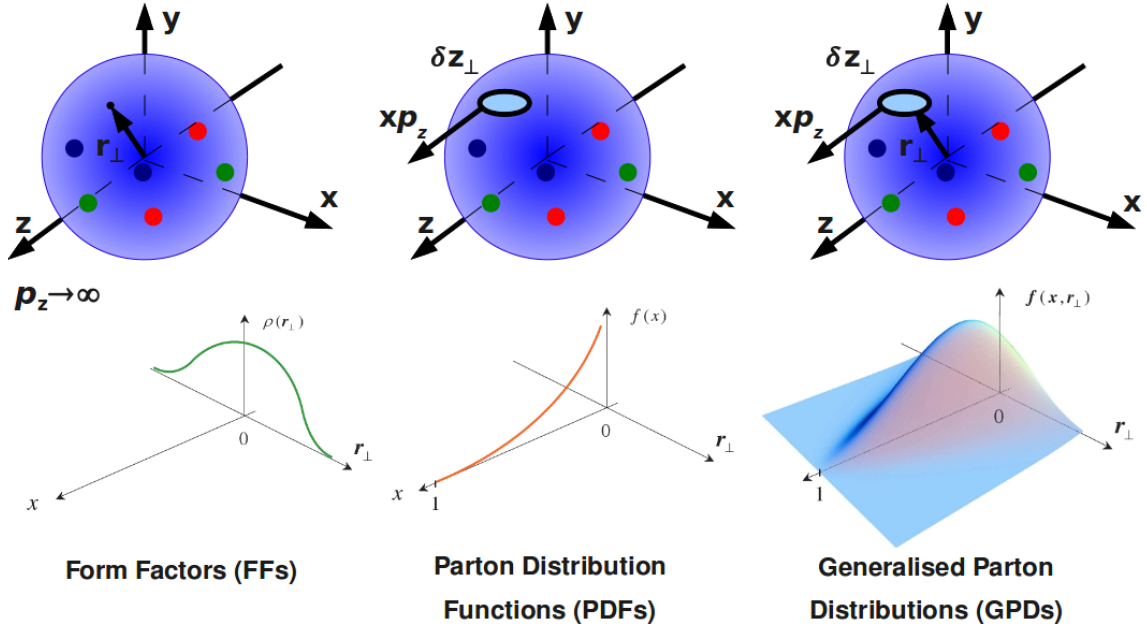
Figure 2.1: Illustration of the relationship of nucleon FFs and PDFs to GPDs in the infinite momentum frame of the nucleon. Figure amended from Ref. [26].

The Lorentz-invariant variables Q^2 and W^2 are defined as

$$Q^2 \equiv -\mathbf{q}^2 \equiv -\left(\mathbf{k} - \mathbf{k}'\right)^2 , \tag{2.2}$$

$$W^2 \equiv \left(\mathbf{p} + \mathbf{q}\right)^2 , \tag{2.3}$$

where Q^2 is the negative squared four-momentum transfer to the virtual photon (alternatively referred to as the 'photon virtuality') and W^2 is the squared invariant mass of the $\gamma^* p$ system. The quantity ν is expressed as

$$\nu \equiv \frac{\mathbf{p} \cdot \mathbf{q}}{M_p} , \tag{2.4}$$

where M_p is the rest mass of the proton. As this thesis presents results from the HERMES fixed-target experiment (see Chapter 4), the variables in Eqs. $2.2 - 2.4$ can be expressed in the lab frame, where the target proton is at rest, as

$$Q^2 \overset{\text{lab}}{=} 4EE' \sin^2\left(\frac{\theta_\ell}{2}\right) , \tag{2.5}$$

$$W^2 \overset{\text{lab}}{=} M_p^2 + 2M_p\nu - Q^2 , \tag{2.6}$$

$$\nu \overset{\text{lab}}{=} E - E' , \tag{2.7}$$

where the angle θ_ℓ is the polar lepton-scattering angle with respect to the initial lepton direction, and ν is interpreted as the difference between the initial (E) and final (E') state lepton energies, *i.e.* the energy lost by the lepton during scattering.

The Mandelstam t variable, defined as the square of the transverse momentum transfer to the proton during the scattering process, is quantified by

$$t \equiv \left(\mathbf{p} - \mathbf{p}'\right)^2 . \tag{2.8}$$

Here, $\mathbf{p}'$ denotes the four-momentum of the recoiling proton in the final state for the case when the target proton remains intact.

It is also necessary to introduce a number of dimensionless quantities: Bjorken variable x_{B}, y, and 'skewedness' parameters ξ and η. These are defined as

$$x_{\mathrm{B}} \quad \equiv \quad \frac{Q^2}{2\left(\mathbf{p} \cdot \mathbf{q}\right)} \overset{\mathrm{lab}}{=} \frac{Q^2}{2\,M_p\,\nu} , \tag{2.9}$$

$$y \quad \equiv \quad \frac{\mathbf{p} \cdot \mathbf{q}}{\mathbf{p} \cdot \mathbf{k}} \overset{\mathrm{lab}}{=} \frac{\nu}{E} , \tag{2.10}$$

$$\xi \quad \overset{\mathrm{lab}}{=} \quad \frac{x_{\mathrm{B}}\left(1 + \frac{t}{2Q^2}\right)}{2 - x_{\mathrm{B}} + x_{\mathrm{B}}\frac{t}{Q^2}} , \tag{2.11}$$

$$\eta \quad \overset{\mathrm{lab}}{=} \quad \frac{-\xi}{1 + \frac{t}{2Q^2}} , \tag{2.12}$$

where η is a measure of the deviation of the x-dependence of GPDs from PDFs, alternatively referred to as the 'off-forwardness' [17]. In the Bjorken-limit ($Q^2 \to \infty$, fixed x_{B} and small t) this is equal in magnitude to ξ, referred to as the skewness parameter. The ξ definition from Ref. [27] is adopted.

The Concept of Twist

When considering GPDs, a knowledge of the term 'twist' is also essential. Twist is defined as the dimension of the hadronic tensor operator minus its spin [28] and is used throughout this thesis to quantify the order of suppression of GPDs by kinematic factors of $\mathcal{O}\left(\frac{1}{Q}\right)$. Leading-twist, *i.e.* twist–2, terms have no such suppression arising from twist effects and in general, the level of twist t_θ corresponds to a suppression of $\mathcal{O}\left(Q^{2-t_\theta}\right)$.

The level of twist can be further understood in terms of the helicities of the virtual and produced real photons [19] in the case of Deeply Virtual Compton Scattering (DVCS). This process will be covered in Chapter 3. For quark GPDs, leading twist relates to the case where there is no change in helicity between the virtual and real photons. Twist–3 coincides with a change by one unit of helicity and twist–4 by two units. The latter case is represented by twist–2 gluon-helicity-flip GPDs which rely on gluon operators to account for the necessary 'flip' of the hadron helicity, which would otherwise violate angular momentum conservation laws. These are illustrated in Fig. 2.2.
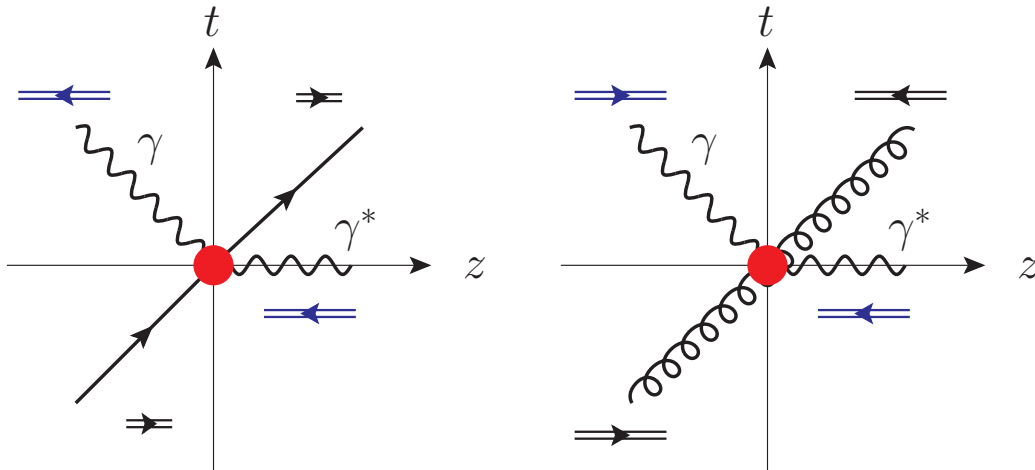
Figure 2.2: Minkowski diagrams for the DVCS process at leading-twist level for quarks (left) and gluons (right) [29]. The double arrows represent the helicity orientations of the partons and photons where for quarks (gluons) there is no change (a change by two helicity units) between the virtual and real photons. For the twist–3 quark case, the virtual photon has no transverse component of helicity.

The discussion throughout this thesis will focus on twist–2 and twist–3 quark GPDs unless otherwise stated.

2.2 Interpretations of GPDs

The interpretation of GPDs is dependent on the kinematic region in which they are studied. The DGLAP region of $x \geq \xi$ ($x \leq -\xi$) describes the removal and absorption of quarks (antiquarks) with respect to the nucleon, whereas the ERBL region of $-\xi \leq x \leq \xi$, is characterised by the removal of a quark-antiquark pair. These two interpretations are based on evolution equations from Refs. [30–33] and Refs. [34,35] respectively, which govern the QCD Q^2-evolution of the GPDs within each region. The leading-order 'handbag' diagrams are illustrated in Fig. 2.3 with the corresponding quark momentum fractions highlighted.

For the analysis presented in this thesis, the DGLAP quark region is considered.

2.3 GPDs of Particular Interest

Generalised parton distributions depend on four kinematic variables: x, ξ, Q^2, and t. In the infinite momentum frame, x represents the average longitudinal momentum fraction of the
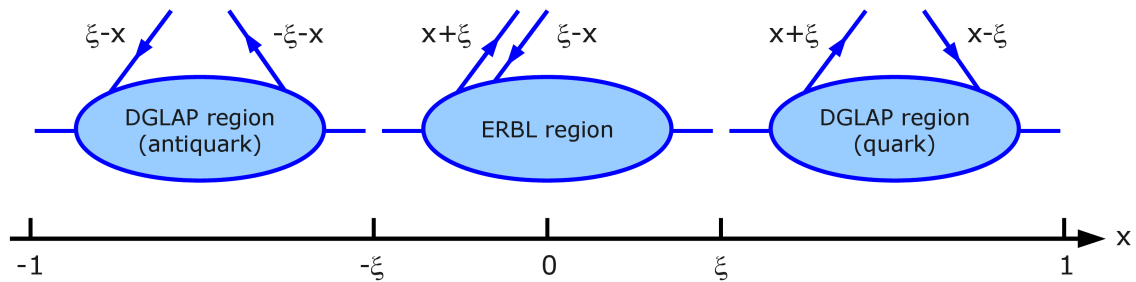
Figure 2.3: Illustration of the DGLAP and ERBL x-regions which offer different interpretations of GPDs.

struck quark in a nucleon travelling in that direction. It is not currently possible to directly measure x. The skewness ξ is half the difference of the longitudinal momentum fractions of quarks with respect to the nucleon momentum between the initial and final states, as shown in Fig. 2.3. This is related to the well-defined x_{B} from Eq. 2.11. The dependence on Q^2 is omitted in the following discussion as the QCD-evolution with Q^2 is well understood and has been calculated perturbatively to leading order (LO) [3, 16–18, 36] and next-to-leading order (NLO) [37–39] in the strong coupling constant α_{s}. However, the results of this thesis will be presented as a function of Q^2 to provide as comprehensive an analysis as possible. The results will also be plotted against $-t$ and x_{B} to provide useful information for ongoing and future GPD models based on experimental data [40–42]. The limited x-range of the HERMES experiment serves only to constrain GPDs. Future measurements from other experiments [43–45] spanning a wider range in x will be invaluable in the attempt to determine J_q.

At leading-twist and for each quark flavour q there are four chirality-conserving, spin $\frac{1}{2}$ GPDs to consider: the helicity-averaged 'unpolarised' H^q and E^q, and the helicity-dependent 'polarised' $\widetilde{H}^q$ and $\widetilde{E}^q$. In addition, GPDs H^q and $\widetilde{H}^q$ conserve nucleon helicity whereas E^q and $\widetilde{E}^q$ are associated with a change in helicity. Throughout this discussion the convention $F^q \in \left\{ H^q,\, E^q,\, \widetilde{H}^q,\, \widetilde{E}^q \right\}$ will be used.

Gluon GPDs are considered to be beyond the scope of this thesis. However, reference will be made to the gluon-helicity-flip GPDs $F_{\mathrm{T}} \in \left\{ H_{\mathrm{T}},\, E_{\mathrm{T}},\, \widetilde{H}_{\mathrm{T}},\, \widetilde{E}_{\mathrm{T}} \right\}$ which deal with flips in gluon helicity. These appear at gluon leading-twist and are suppressed by $\frac{\alpha_{\mathrm{s}}}{\pi}$ compared to the quark leading-twist GPDs.

A summary of the relevant GPDs and their properties can be found in Table 2.1 and a more comprehensive summary, including spin 1 GPDs associated with scattering off a deuteron, can be found in Refs. [19, 24].

Spin $\frac{1}{2}$ GPD	Nucleon-helicity conserving	Quark-helicity dependent
H	$\checkmark$	x
$\widetilde{H}$	$\checkmark$	$\checkmark$
E	x	x
$\widetilde{E}$	x	$\checkmark$

Table 2.1: Summary of the leading-twist quark-chirality conserving GPDs and their various properties.

2.4 GPDs and the Spin of the Nucleon

Interest in GPDs was sparked after it was postulated by Xiangdong Ji [3] that they provide the opportunity to calculate the total angular momentum carried by quarks in the nucleon. According to the Ji Relation, J_q can be determined in the forward limit of vanishing momentum transfer as the second x-moment of the linear combination of GPDs H^q and E^q, *i.e.*

$$J_q = \frac{1}{2} \lim_{t \to 0} \int_{-1}^{1} \left[H^q\left(x, \xi, t\right) + E^q\left(x, \xi, t\right) \right] x \, dx \, . \tag{2.13}$$

Here, the x-ranges (0,1] and [-1,0) relate to distributions of quarks and antiquarks respectively.

2.5 Relating GPDs to Other Functions

At the start of this chapter the relationships between GPDs and the monodimensional PDF and FF distributions were illustrated. Here, the explicit relations between these sets of functions are outlined with additional important relations that arise from expressing GPDs in terms of Compton Form Factors (CFFs) and Gegenbauer polynomials.

Parton Distribution Functions

In the forward limit ($t \to 0$ and $\xi = 0$), the nucleon-helicity-conserving GPDs reduce to measured PDFs for quark and antiquark distributions as [19, 27]

$$H^q(x, 0, 0) \quad = \quad q(x) \, , \qquad \widetilde{H}^q(x, 0, 0) = \Delta q(x) \, , \tag{2.14}$$

$$H^{\bar{q}}(-x, 0, 0) \quad = \quad -\bar{q}(-x) \, , \qquad \widetilde{H}^{\bar{q}}(-x, 0, 0) = \Delta \bar{q}(-x) \, , \tag{2.15}$$

where $q(x)$ and $\bar{q}(-x)$ are respectively, the longitudinal distribution of quarks and antiquarks of flavour q in the nucleon. The corresponding quark and antiquark helicity distributions are given as $\Delta q(x)$ and $\Delta\bar{q}(-x)$. In the forward limit, $E(x, \xi, t)$ and $\widetilde{E}(x, \xi, t)$, which do not conserve nucleon helicity, are not defined and consequently have no relation to PDFs.

Nucleon Form Factors

The first Mellin x-moment of the four leading-twist quark GPDs reduce to [3, 46]:

$$\int_{-1}^{1} dx\, H(x, \xi, t) = F_1(t)\,, \tag{2.16}$$

$$\int_{-1}^{1} dx\, E(x, \xi, t) = F_2(t)\,, \tag{2.17}$$

$$\int_{-1}^{1} dx\, \widetilde{H}(x, \xi, t) = G_A(t)\,, \tag{2.18}$$

$$\int_{-1}^{1} dx\, \widetilde{E}(x, \xi, t) = G_P(t)\,, \tag{2.19}$$

where F_1, F_2, G_A and G_P are the Dirac, Pauli, axial and pseudoscalar parton FFs of the nucleon, respectively. The dependence on ξ drops out with integration over the range in x since ξ is a measure in the same degree of freedom as x.

Compton Form Factors

An important concept which is fundamental to the analysis presented in this thesis is that of CFFs. These provide the link between GPDs and scattering amplitudes. The CFF $\mathcal{F} \in \left\{ \mathcal{H}, \mathcal{E}, \widetilde{\mathcal{H}}, \widetilde{\mathcal{E}} \right\}$ is a convolution of the corresponding GPD F with a hard-scattering kernel, *i.e.*

$$\mathcal{F}(\xi, t) = \int_{-1}^{1} C^{\pm}(x,\, \xi)\, F(x,\, \xi,\, t)\, dx\,, \tag{2.20}$$

where the scattering kernels $C^{\pm}$ are complex functions and superscript $+$ $(-)$ relates to CFFs $\widetilde{\mathcal{H}}$ and $\widetilde{\mathcal{E}}$ ($\mathcal{H}$ and $\mathcal{E}$). These kernels are expanded in terms of real and imaginary components as

$$C^{\pm}(x,\, \xi) = \frac{1}{x - \xi - i\mu} \pm \frac{1}{x + \xi - i\mu} + \mathcal{O}(\alpha_s)\,, \tag{2.21}$$

where μ is a small, non-zero term which allows the kernel to exist when $x = \xi = 0$. From this, CFFs are related to their corresponding GPD at leading-twist and leading-order in

α_{s} as

$$\Im m\, \mathcal{F}(\xi,\, t) \quad = \quad F(\xi,\, \xi,\, t) \pm F(-\xi,\, \xi,\, t)\,, \tag{2.22}$$

$$\Re e\, \mathcal{F}(\xi,\, t) \quad = \quad \mathcal{P}_{\mathrm{C}} \int_{-1}^{1} \frac{F(x,\, \xi,\, t)}{x - \xi} \pm \frac{F(x,\, \xi,\, t)}{x + \xi}\, dx\,, \tag{2.23}$$

where $\mathcal{P}_{\mathrm{C}}$ denotes Cauchy's principle value integral.

There also exist 'effective' twist–3 CFFs, denoted $\mathcal{F}^{\mathrm{eff}}$, which arise via a combination of twist–2 and twist–3 CFFs as [37]

$$\mathcal{F}^{\mathrm{eff}} \equiv -2\xi \left(\frac{\mathcal{F}}{1 + \xi} + \mathcal{F}^3 \right). \tag{2.24}$$

Here, $\mathcal{F}^3$ are twist–3 CFFs which are expansible in terms of twist–2 Wandzura-Wilczek (WW) terms [47], suppressed by ξ, and twist–3 contributions which describe the correlations between antiquarks, gluons and quarks in the nucleon [27].

Higher-Order Mellin Moments

Another important property of GPDs is the polynomiality of their higher-order Mellin moments. The nth moment of H^q and E^q are expanded with Gegenbauer polynomials in ξ as

$$\int_{-1}^{1} dx\, x^n\, H^q(x, \xi, t) \quad = \quad \sum_{i=0,2,4\ldots}^{n} (2\xi)^i A_{i,n+1}^q(t) + (2\xi)^{n+1} C_{n+1}^q(t)\,, \tag{2.25}$$

$$\int_{-1}^{1} dx\, x^n\, E^q(x, \xi, t) \quad = \quad \sum_{i=0,2,4\ldots}^{n} (2\xi)^i B_{i,n+1}^q(t) - (2\xi)^{n+1} C_{n+1}^q(t)\,, \tag{2.26}$$

where the $C_{n+1}^q(t)$ terms exist only for odd powers of n. The polarised GPDs expand as

$$\int_{-1}^{1} dx\, x^n\, \widetilde{H}^q(x, \xi, t) \quad = \quad \sum_{i=0,2,4\ldots}^{n} (2\xi)^i \widetilde{A}_{i,n+1}^q(t)\,, \tag{2.27}$$

$$\int_{-1}^{1} dx\, x^n\, \widetilde{E}^q(x, \xi, t) \quad = \quad \sum_{i=0,2,4\ldots}^{n} (2\xi)^i \widetilde{B}_{i,n+1}^q(t)\,. \tag{2.28}$$

2.6 Double-Distribution GPD Parametrisation

In Chapter 7 the GPD-related results of this thesis are presented in comparison to calculations from the Vanderhaeghen-Guidal-Guichon 'VGG' computer code implementation [48] of the GPD model from Refs. [46, 49]. This is based on a 'Double-Distribution' (DD) parametrisation of GPDs detailed in Ref. [50]. This model evaluates GPDs up to twist–3 level in the WW-approximation with no treatment of gluon-helicity-flip terms.

The x and ξ dependences of the GPDs are disentangled using δ-functions, *i.e.*

$$F^q(x,\xi,t) = \int_{-1}^{1} d\beta \int_{-1+|\beta|}^{1-|\beta|} d\alpha \, \delta(\beta + \alpha\xi - x) \, F_{\mathrm{DD}}^q(\beta,\alpha,t) \, . \qquad (2.29)$$

Here $F_{\mathrm{DD}}^q(\beta,\alpha,t)$ represents the DD of GPD $F^q(x,\xi,t)$.

The DDs are separated into t-independent and t-dependent components, where the former is expressed as [50]

$$F_{\mathrm{DD}}(\beta,\alpha) = h(\beta,\alpha)f(\beta) \, , \qquad (2.30)$$

in terms of an ordinary PDF $f(\beta)$, specific to the GPD, and a profile function

$$h(\beta,\alpha) = \frac{\Gamma(2b-2)}{2^{2b+1}\Gamma^2(b+1)} \frac{\left[(1-|\beta|)^2 - \alpha^2\right]^b}{(1-|\beta|)^{2b+1}} \, . \qquad (2.31)$$

The b-parameter is decomposed into contributions b_{valence} and b_{sea} from the valence and sea quarks respectively, and governs the GPD dependence on ξ. These can be varied between unity and infinity (relating to the ξ-independent scenario) for the H^q and $\widetilde{H}^q$ contributions in theoretical calculations. For all other GPD parametrisations, the b-parameters are fixed to unity.

The t-dependent part uses the Regge-inspired prediction that structure functions vary as $x^{-\alpha'}$ with 'Regge-slope' $\alpha' = 0.8\,\mathrm{GeV}^2$. Therefore, the DD can be expressed as

$$F_{\mathrm{DD}}^q(\beta,\alpha,t) = h(\beta,\alpha)f(\beta)\frac{1}{|\beta|^{\alpha't}} \, , \qquad (2.32)$$

allowing the theoretical calculation of GPD $F^q(x,\xi,t)$.

Parametrisation of GPD H

Observing the polynomiality relation from Eq. 2.25, it is shown that for the highest power of ξ at odd n, GPD H^q is not fully described by Eq. 2.29. However, with the addition of the 'D term' [51], the parametrisation can be fully evaluated in terms of DDs as

$$H^q(x,\xi,t) = \int_{-1}^{1} d\beta \int_{-1+|\beta|}^{1-|\beta|} d\alpha \, \delta(\beta+\alpha\xi-x) \, H_{\mathrm{DD}}^q(\beta,\alpha,t) + \theta\left(1 - \frac{x^2}{\xi^2}\right) D\left(\frac{x}{\xi},t\right) \, , \quad (2.33)$$

where $f(\beta)$ in this case is the quark-density distribution $q(\beta)$, *i.e.* GPD H^q in the forward limit as shown in Eq. 2.14.

The D term is related to the Gegenbauer polynomials from the nth Mellin moment as

$$C_{n+1}(t) = \int_{-1}^{1} \left(\frac{x}{\xi}\right)^n D\left(\frac{x}{\xi},t\right) d\left(\frac{x}{\xi}\right) \, . \qquad (2.34)$$

Parametrisation of GPD E

Analogous to H^q, a similar double-distribution representation for E^q is constructed as

$$E^q(x,\xi,t) = \int_{-1}^{1} d\beta \int_{-1+|\beta|}^{1-|\beta|} d\alpha\, \delta(\beta + \alpha\xi - x)\, E^q_{\mathrm{DD}}(\beta,\alpha,t) - \theta\left(1 - \frac{x^2}{\xi^2}\right) D\left(\frac{x}{\xi},t\right). \quad (2.35)$$

As E^q has no physical interpretation in the forward limit, $f(\beta)$ is an unknown function. From Eq. 2.13 however, it is shown to exhibit a dependence on J_q which subsequently enters into this model as a free parameter, therefore allowing the values of J_q to be constrained [22].

In addition, the opposite signs of the D term contributions from Eqs. 2.33 and 2.35, result in these terms cancelling in the Ji Relation (Eq. 2.13).

Parametrisation of GPD $\widetilde{H}$

The dominant GPD contribution to the results extracted in this thesis is that from the polarised $\widetilde{H}^q$. In terms of DDs, and reducing to $\Delta q(\beta)$ in the forward limit, $\widetilde{H}^q$ is expressed as

$$\widetilde{H}^q(x,\xi,t) = \int_{-1}^{1} d\beta \int_{-1+|\beta|}^{1-|\beta|} d\alpha\, \delta(\beta + \alpha\xi - x)\, \widetilde{H}^q_{\mathrm{DD}}(\beta,\alpha,t). \quad (2.36)$$

The input $\Delta q(\beta)$ distributions have been determined from a next-to-leading order QCD analysis of inclusive polarised DIS at fixed $Q^2 = 1\,\mathrm{GeV}$ as [46]

$$\Delta u_{\mathrm{val}}(x) \;=\; \eta_u\, A_u\, x^{0.250}\, u_{\mathrm{val}}(x), \quad (2.37)$$

$$\Delta d_{\mathrm{val}}(x) \;=\; \eta_d\, A_d\, x^{0.231}\, d_{\mathrm{val}}(x), \quad (2.38)$$

$$\Delta S(x) \;=\; \eta_S\, A_S\, x^{0.576}\, S(x), \quad (2.39)$$

where S denotes all flavours of sea quark. The normalisation factors A_q are determined such that the first x-moment of Δq is given by the corresponding quark density η_q. The DD $\widetilde{H}^q_{\mathrm{DD}}$ is then expressed using a factorised t ansatz as

$$\widetilde{H}^q_{\mathrm{DD}}(\beta,\alpha,t) = h(\beta,\alpha)\, \Delta q(\beta)\, \frac{G^q_{\mathrm{A}}(t)}{G^q_{\mathrm{A}}(0)}. \quad (2.40)$$

This construction is limited to small values of t where the relation in Eq. 2.18 is satisfied to within 10%. As a result, the Regge-inspired ansatz is used. This is expressed as

$$\widetilde{H}^q_{\mathrm{DD}}(\beta,\alpha,t) = h(\beta,\alpha)\, \Delta q(\beta)\, \frac{1}{|\beta|^{\alpha' t}}. \quad (2.41)$$
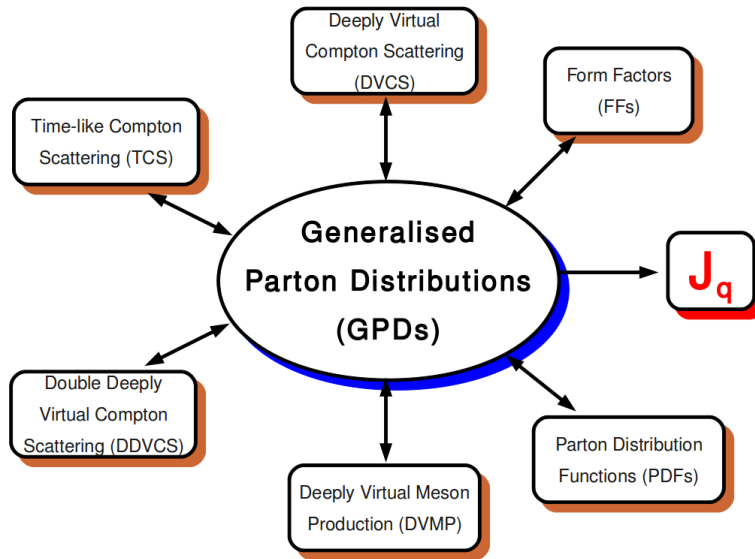
Figure 2.4: Illustration of some of the possible processes through which access to GPD information is possible. The link to FFs and PDFs have been described in the text, as has the possibility introduced by Ji [3] to determine the total angular momentum of the quarks in the nucleon, J_q.

Parametrisation of GPD $\widetilde{E}$

Similar to E^q, there is no physical interpretation for $\widetilde{E}^q$ in the forward limit. The only possible constraint which can be imposed is the relationship to G_P from the first x-moment shown in Eq. 2.19. At small values of t, this FF, and hence GPD $\widetilde{E}^q$, is dominated by the pion-pole contribution. This is modelled as in Ref. [46].

2.7   Experimental Access to GPDs

There are currently several experimental processes which offer the possibility to access information on GPDs and provide a means to determine J_q. Some of these are illustrated in Fig. 2.4 and are briefly described here for the case of a proton target:

- Time-like Compton Scattering (TCS) [52], represented by $\gamma\, p \to p\, l^+\, l^-$, involves the photoproduction of a lepton-antilepton pair.

- Deeply Virtual Meson Production (DVMP) [19], *i.e.* $e\, p \to e\, p\, M$, is the exclusive leptoproduction of a neutral meson M *e.g.* ρ, ω, π.

- Deeply Virtual Compton Scattering, the hard exclusive leptoproduction of a real

photon *i.e.* $e\,p \to e\,p\,\gamma$.

- Double Deeply Virtual Compton Scattering (DDVCS) [53], the scattering of a virtual photon from the proton with the production of a virtual photon in the final state. This subsequently decays into a lepton-antilepton pair *i.e.* $\gamma^* \, p \to p \, l^+ \, l^-$.

The DVCS process will be detailed in the following chapter.

Chapter 3

Deeply Virtual Compton Scattering

The most promising way to experimentally access information on GPDs is by studying hard exclusive processes. Hard exclusive leptoproduction of real photons, *i.e.* Deeply Virtual Compton Scattering (DVCS), is currently regarded as having the simplest theoretical interpretation in terms of GPDs as it has a single hadron in the final state and has been calculated perturbatively in QCD to next-to-next-to-leading order (NNLO) in α_{s} [54]. In addition, DVCS is unique in that the produced photon carries direct information about the partonic structure of the nucleon. This process can therefore be described solely with GPDs [55] under known kinematic conditions.

3.1 Accessing GPDs via DVCS

In the one-photon-exchange approximation, shown in Fig. 3.1, DVCS of an electron or positron off a proton target is represented by

$$e(\mathbf{k})\, p(\mathbf{p}) \stackrel{\gamma^*(\mathbf{q})}{\to} e(\mathbf{k}')\, p(\mathbf{p}')\, \gamma(\mathbf{q}') \,, \tag{3.1}$$

where $\mathbf{k}\,(\mathbf{k}')$ and $\mathbf{p}\,(\mathbf{p}')$ represent the four-momenta of the incoming (scattered) lepton and the target (recoiling) proton respectively. In this process, a virtual photon with four-momentum $\mathbf{q}$ couples to the nucleon as the incoming lepton Compton scatters [56] off a quasi-free parton in the nucleon. This parton (a quark at the kinematics involved in this thesis) is 'removed' from the nucleon with a longitudinal momentum fraction of $x + \xi$, where ξ is half the longitudinal momentum change of the parton throughout the process.

16
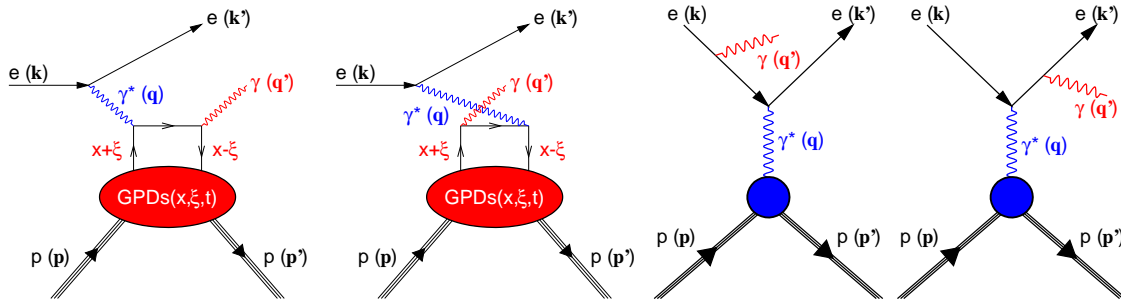
Figure 3.1: From left to right, the leading-order diagrams for the Deeply Virtual Compton Scattering (DVCS) and Bethe-Heitler (BH) processes where e (e') represents the incoming (scattered) lepton, p (p') is the struck target (recoiling) proton and γ^* (γ) is the virtual (real) photon. In DVCS, the structure of the probed nucleon can be described using the GPD framework parameterised by x, ξ and t. In BH, the real photon is emitted by the incoming or scattered lepton.

The struck parton is 'absorbed' with a momentum fraction $x - \xi$. The parton radiates a real photon with four-momentum $\mathbf{q}'$. The target nucleon is left intact throughout this process. Figure 3.1 also shows the elastic Bethe-Heitler (BH) [57] process where the incoming lepton scatters off the nucleon as a whole and not from a quark. A real photon is radiated from either the incoming or scattered lepton. This process is exactly calculable in the framework of Quantum Electrodynamics (QED) from the Dirac and Pauli FFs introduced in Section 2.5. The total four-fold differential cross-section of the $e\,p \to e\,p\,\gamma$ process, neglecting transverse target polarisation components, is given as [23]

$$\frac{\mathrm{d}\sigma}{\mathrm{d}x_{\mathrm{B}}\,\mathrm{d}Q^2\,\mathrm{d}|t|\,\mathrm{d}\phi} = \frac{x_{\mathrm{B}}\,e^6\,|\tau|^2}{32(2\pi)^4\,Q^4\,\sqrt{1+\epsilon^2}} , \tag{3.2}$$

where the angle ϕ is defined in accordance with the Trento convention [58] as the azimuthal angle between the lepton-scattering and photoproduction planes (shown in Fig. 3.2), e is the charge of the lepton beam and the kinematic variable $\epsilon = 2x_{\mathrm{B}}\frac{M_p}{Q}$.

As DVCS and BH have the same initial and final states, they are experimentally indistinguishable. Therefore the scattering amplitudes τ_{DVCS} and τ_{BH} add coherently in the squared scattering amplitude $|\tau|^2$, resulting in an interference term $\mathcal{I}$, *i.e.*

$$|\tau|^2 = |\tau_{\mathrm{BH}}|^2 + |\tau_{\mathrm{DVCS}}|^2 + \overbrace{\tau_{\mathrm{BH}}\tau^*_{\mathrm{DVCS}} + \tau^*_{\mathrm{BH}}\tau_{\mathrm{DVCS}}}^{\mathcal{I}} . \tag{3.3}$$

At HERMES kinematics, it has been shown [57] that the BH process is the dominant contribution to the scattering cross-section. This is illustrated in Fig. 3.3 which compares the differential cross-sections of the BH and DVCS processes at HERMES kinematics as a
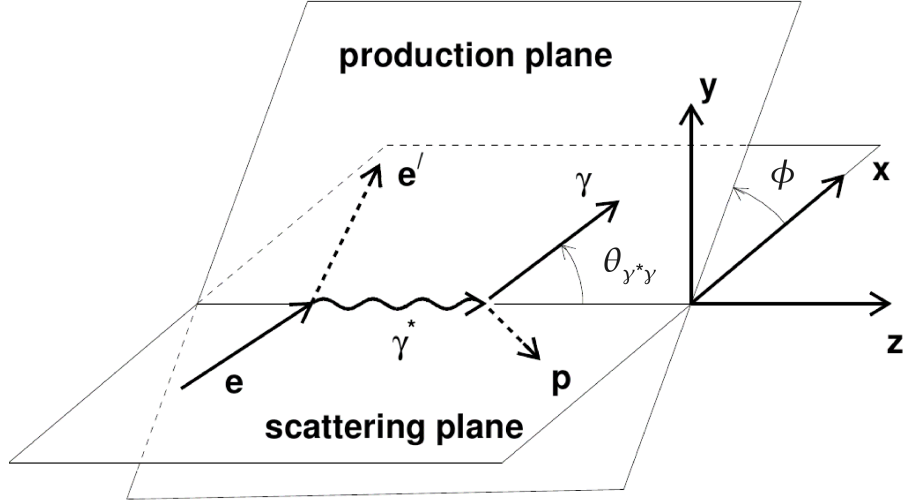
Figure 3.2: The lepton-scattering and photoproduction planes of the DVCS process. The lepton (e) scatters off a constituent quark in the proton (p) by means of virtual photon (γ^*) with the emission of a real photon (γ). The angles ϕ and $\theta_{\gamma^*\gamma}$ described in the text are labelled.

function of the polar angle $\theta_{\gamma^*\gamma}$ between the virtual and real photons (shown in Fig. 3.2). The DVCS cross-section has a maximum at $\theta_{\gamma^*\gamma} = 0$ corresponding to collinearity between the photons, whereas the BH process exhibits a three-peak cross-section where the peaks reflect the real photon being collinear with the virtual photon, the incoming lepton or the scattered lepton. The three peaks are commonly referred to, respectively, as the Compton peak and initial and final state radiation [59].

Although the squared-DVCS term $|\tau_{\mathrm{DVCS}}|^2$ is suppressed at HERMES kinematics with respect to the squared-BH term $|\tau_{\mathrm{BH}}|^2$ and therefore difficult to investigate directly, there is an opportunity to access DVCS amplitudes via $\mathcal{I}$. This has the effect of amplifying the suppressed DVCS amplitudes with dominant BH terms. The components of $|\tau|^2$ from Eq. 3.3 can be expanded in a Fourier series in ϕ as [27]

$$|\tau_{\mathrm{BH}}|^2 = \frac{K_{\mathrm{BH}}}{\mathcal{P}_1(\phi)\mathcal{P}_2(\phi)} \sum_{n=0}^{2} c_n^{\mathrm{BH}} \cos(n\phi) , \qquad (3.4)$$

$$|\tau_{\mathrm{DVCS}}|^2 = K_{\mathrm{DVCS}} \left(\sum_{n=0}^{2} c_n^{\mathrm{DVCS}} \cos(n\phi) + \sum_{n=1}^{2} s_n^{\mathrm{DVCS}} \sin(n\phi) \right) , \qquad (3.5)$$

$$\mathcal{I} = \frac{-e_\ell K_{\mathcal{I}}}{\mathcal{P}_1(\phi)\mathcal{P}_2(\phi)} \left(\sum_{n=0}^{3} c_n^{\mathcal{I}} \cos(n\phi) + \sum_{n=1}^{3} s_n^{\mathcal{I}} \sin(n\phi) \right) , \qquad (3.6)$$

where e_ℓ represents the charge of the lepton beam in units of the elementary charge and
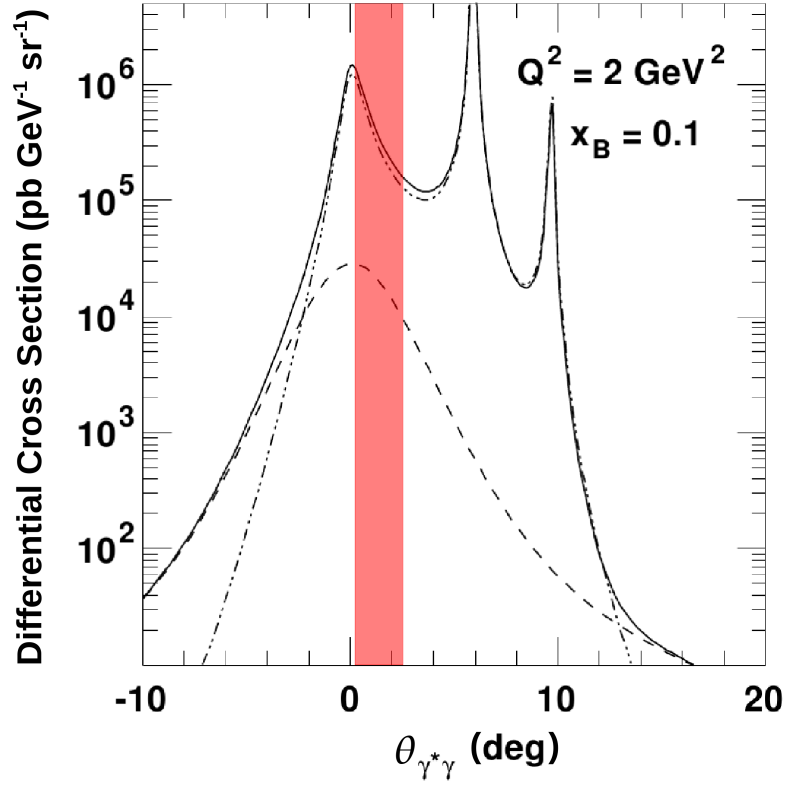
Figure 3.3: Differential cross-section of the total $ep \to ep\gamma$ interaction (solid line) at HERMES beam energy of $27.57\,\text{GeV}$ and contributions from the DVCS (dashed line) and BH (dot-dashed line) processes as a function of $\theta_{\gamma^*\gamma}$ at $Q^2 = 2\,\text{GeV}^2$ and $x_\text{B} = 0.1$. The shaded region highlights the analysed $\theta_{\gamma^*\gamma}$ DVCS range at HERMES, indicating the order of magnitude suppression of the DVCS process compared to BH. Figure amended from Ref. [57].

the terms K_BH, K_DVCS and $K_\mathcal{I}$ relate to kinematic factors as

$$K_\text{BH} \quad = \quad \frac{1}{x_\text{B}^2\, t\, (1 + \epsilon^2)^2}\,, \tag{3.7}$$

$$K_\text{DVCS} \quad = \quad \frac{1}{Q^2}\,, \tag{3.8}$$

$$K_\mathcal{I} \quad = \quad \frac{1}{x_\text{B}\, y\, t}\,. \tag{3.9}$$

The ϕ-dependent terms $\mathcal{P}_1(\phi)$ and $\mathcal{P}_2(\phi)$ are lepton propagators of the BH process. These are expressed as

$$\mathcal{P}_1(\phi) \quad \equiv \quad (\mathbf{k} - \mathbf{q}')^2 = -\frac{J + \mathcal{K}\cos\phi}{y\,(1 + \epsilon^2)}\,, \tag{3.10}$$

$$\mathcal{P}_2(\phi) \quad \equiv \quad (\mathbf{k}' + \mathbf{q}')^2 = 1 + \frac{t}{Q^2} - \mathcal{P}_1(\phi)\,, \tag{3.11}$$

where $\mathcal{K}$ is a $\frac{\sqrt{-t}}{Q}$ suppressed kinematic factor and

$$J = \left(1 - y - \frac{y\,\epsilon^2}{2}\right)\left(1 + \frac{t}{Q^2}\right) - (1 - x_\text{B})(2 - y)\frac{t}{Q^2}\,. \tag{3.12}$$

In the Bjorken-limit, the lepton propagators can be expanded in a power series with respect to $\frac{1}{Q}$. This results in the Fourier coefficients of higher harmonics suffering kinematic suppression by powers of $\mathcal{K}$. The Fourier expansion of $|\tau|^2$ is shown to terminate at twist–3 level ensuring a finite number of harmonics [27].

For a longitudinally polarised proton target, neglecting any transverse target polarisation components, this expansion reads

$$
|\tau_{\mathrm{BH}}|^2 = \frac{K_{\mathrm{BH}}}{\mathcal{P}(\phi)} \left(\sum_{n=0}^{2} c_{n,\mathrm{u}}^{\mathrm{BH}} \cos(n\phi) + P_\ell \, P_{\mathrm{L}} \sum_{n=0}^{1} c_{n,\mathrm{LP}}^{\mathrm{BH}} \cos(n\phi) \right) , \qquad (3.13)
$$

$$
\begin{aligned}
|\tau_{\mathrm{DVCS}}|^2 = K_{\mathrm{DVCS}} \bigg(& \sum_{n=0}^{2} c_{n,\mathrm{u}}^{\mathrm{DVCS}} \cos(n\phi) + P_\ell \, s_{1,\mathrm{u}}^{\mathrm{DVCS}} \sin\phi \\
& + P_\ell \, P_{\mathrm{L}} \sum_{n=0}^{1} c_{n,\mathrm{LP}}^{\mathrm{DVCS}} \cos(n\phi) + P_{\mathrm{L}} \sum_{n=1}^{2} s_{n,\mathrm{LP}}^{\mathrm{DVCS}} \sin(n\phi) \bigg) , \qquad (3.14)
\end{aligned}
$$

$$
\begin{aligned}
\mathcal{I} = \frac{-e_\ell \, K_{\mathcal{I}}}{\mathcal{P}(\phi)} \bigg(& \sum_{n=0}^{3} c_{n,\mathrm{u}}^{\mathcal{I}} \cos(n\phi) + P_\ell \sum_{n=1}^{2} s_{n,\mathrm{u}}^{\mathcal{I}} \sin(n\phi) \\
& + P_\ell \, P_{\mathrm{L}} \sum_{n=0}^{2} c_{n,\mathrm{LP}}^{\mathcal{I}} \cos(n\phi) + P_{\mathrm{L}} \sum_{n=1}^{3} s_{n,\mathrm{LP}}^{\mathcal{I}} \sin(n\phi) \bigg) , \qquad (3.15)
\end{aligned}
$$

where the subscript u (LP) represents the coefficients inherent from an unpolarised (a longitudinally polarised) target, and $\mathcal{P}(\phi) \equiv \mathcal{P}_1(\phi)\mathcal{P}_2(\phi)$. Here, P_ℓ and P_{L} denote the longitudinal polarisations of the beam and target respectively, both with respect to the beam direction. As the target polarisation is longitudinal with respect to the direction of the beam, there is a small transverse component ($\sim 8\%$) with respect to the direction of the virtual photon which will be neglected [60].

The propagators and Fourier coefficients appearing in $|\tau_{\mathrm{BH}}|^2$ can be calculated in QED from known kinematic conditions, with the latter also exhibiting a dependence on the Dirac and Pauli FFs. The Fourier coefficients from $|\tau_{\mathrm{DVCS}}|^2$ and $\mathcal{I}$ have different kinematic and GPD dependences that change with beam and target polarisation state. These provide information on GPDs at differing levels of twist, where leading-twist (twist–2) is least suppressed and next-to-leading twist (twist–3) is suppressed by a further factor of $\frac{1}{Q}$. These coefficients are expressed in terms of kinematic variables, FFs and the imaginary ($\Im\mathrm{m}$) or real ($\Re\mathrm{e}$) parts of CFFs.

3.2 Longitudinally Polarised Target Asymmetries

For the analysis presented in this thesis, three azimuthal asymmetries in the distribution of real photons from hard-exclusive leptoproduction using a longitudinally polarised positron beam and longitudinally polarised proton target are extracted: a single-spin asymmetry, $\mathcal{A}_{\mathrm{UL}}$ ($\mathcal{A}_{\mathrm{LU}}$) depending on the target (beam) polarisation averaged over all beam (target) polarisation states, and a double-spin asymmetry $\mathcal{A}_{\mathrm{LL}}$ dependent on the product of the beam and target polarisations.

The asymmetries are presented in this section alongside the related Fourier harmonics from $|\tau_{\mathrm{DVCS}}|^2$ and $\mathcal{I}$. In the case of $\mathcal{A}_{\mathrm{LL}}$, the first two harmonics also receive an additional sizable contribution from $|\tau_{\mathrm{BH}}|^2$. Their relation to twist–2 and twist–3 GPDs will also be examined.

Unlike previous HERMES analyses [22–25] using data taken with both electron and positron beams, the analysis presented in this thesis was performed with only positron data available. This has the disadvantage compared to the previous analyses in that the contributions from the Fourier amplitudes of $|\tau_{\mathrm{DVCS}}|^2$ and $\mathcal{I}$ cannot be disentangled.

The following Fourier coefficients appearing in $|\tau_{\mathrm{BH}}|^2$, $|\tau_{\mathrm{DVCS}}|^2$ and $\mathcal{I}$ are defined in Ref. [27] and those key to this analysis are given here with the signs of the odd cosinusoidal and even sinusoidal harmonics inverted to bring them into concordance with the ϕ convention used at HERMES, defined as $\phi_{\mathrm{HERMES}} = \pi - \phi_{[27]}$.

Target Single-Spin Asymmetry Arising from $|\tau_{\mathrm{DVCS}}|^2$ and $\mathcal{I}$.

The single-spin asymmetry $\mathcal{A}_{\mathrm{UL}}$ dependent on target polarisation is expressed in terms of the Fourier coefficients in Eqs. $3.13 - 3.15$ as

$$
\mathcal{A}_{\mathrm{UL}}(\phi) \equiv \frac{[\sigma^{\leftarrow\Rightarrow}(\phi) + \sigma^{\rightarrow\Rightarrow}(\phi)] - [\sigma^{\leftarrow\Leftarrow}(\phi) + \sigma^{\rightarrow\Leftarrow}(\phi)]}{[\sigma^{\leftarrow\Rightarrow}(\phi) + \sigma^{\rightarrow\Rightarrow}(\phi)] + [\sigma^{\leftarrow\Leftarrow}(\phi) + \sigma^{\rightarrow\Leftarrow}(\phi)]} \tag{3.16}
$$

$$
= \frac{K_{\mathrm{DVCS}} \sum_{n=1}^{2} s_{n,\mathrm{LP}}^{\mathrm{DVCS}} \sin(n\phi) - \dfrac{e_\ell K_{\mathcal{I}}}{\mathcal{P}(\phi)} \sum_{n=1}^{3} s_{n,\mathrm{LP}}^{\mathcal{I}} \sin(n\phi)}{\dfrac{1}{\mathcal{P}(\phi)} \left[K_{\mathrm{BH}} \sum_{n=0}^{2} c_{n,\mathrm{u}}^{\mathrm{BH}} \cos(n\phi) - e_\ell K_{\mathcal{I}} \sum_{n=0}^{3} c_{n,\mathrm{u}}^{\mathcal{I}} \cos(n\phi) \right] + K_{\mathrm{DVCS}} \sum_{n=0}^{2} c_{n,\mathrm{u}}^{\mathrm{DVCS}} \cos(n\phi)},
$$

where σ is the four-fold cross-section from Eq. 3.2, $\rightarrow$ ($\leftarrow$) denotes the beam helicity parallel (anti-parallel) and $\Leftarrow$ ($\Rightarrow$) represents the target polarisation parallel (anti-parallel) to the direction of the beam momentum. The Fourier coefficients arising from $|\tau_{\mathrm{DVCS}}|^2$

and $\mathcal{I}$ contained in the numerator of Eq. 3.16 are explicitly expressed as

$$s_{1,\text{LP}}^{\text{DVCS}} = -\frac{8\Lambda\mathcal{K}}{2-x_{\text{B}}} \Im m\, \mathcal{C}_{\text{LP}}^{\text{DVCS}} \left(\mathcal{F}^{\text{eff}}, \mathcal{F}^*\right), \tag{3.17}$$

$$s_{2,\text{LP}}^{\text{DVCS}} = \frac{4\Lambda\mathcal{K}^2 Q^2}{M^2(2-x_{\text{B}})} \Im m\, \mathcal{C}_{\text{T}}^{\text{DVCS}}(\mathcal{F}_{\text{T}}, \mathcal{F}^*), \tag{3.18}$$

$$s_{1,\text{LP}}^{\mathcal{I}} = 8\Lambda\mathcal{K}\left(2-2y+y^2\right) \Im m\, \mathcal{C}_{\text{LP}}^{\mathcal{I}}(\mathcal{F}), \tag{3.19}$$

$$s_{2,\text{LP}}^{\mathcal{I}} = -\frac{16\Lambda\mathcal{K}^2(2-y)}{2-x_{\text{B}}} \Im m\, \mathcal{C}_{\text{LP}}^{\mathcal{I}} \left(\mathcal{F}^{\text{eff}}\right), \tag{3.20}$$

$$s_{3,\text{LP}}^{\mathcal{I}} = \frac{8\Lambda\mathcal{K}^3 Q^2}{M^2(2-x_{\text{B}})^2} \Im m\, \mathcal{C}_{\text{T}}^{\mathcal{I}}(\mathcal{F}_{\text{T}}, \mathcal{F}^*), \tag{3.21}$$

where $\Lambda = \pm 1$ denotes the sign of the target polarisation. The '$\mathcal{C}$-functions' are expressed in terms of twist–2 ($\mathcal{F}$, $\mathcal{F}^*$ and $\mathcal{F}_{\text{T}}$) and/or effective twist–3 ($\mathcal{F}^{\text{eff}}$) CFFs and are explained in Section 3.3. The Fourier coefficients $c_{n,\text{u}}^{\text{R}}$ appearing in the denominator from the unpolarised cross-section, where $\text{R} \in \{\text{BH}, \text{DVCS}, \mathcal{I}\}$, introduce a further ϕ-dependent contribution.

Double-Spin Asymmetry Arising from $|\tau_{\text{BH}}|^2$, $|\tau_{\text{DVCS}}|^2$ and $\mathcal{I}$.

The double-spin asymmetry $\mathcal{A}_{\text{LL}}$ dependent on the product of the beam and target polarisations, is expressed in terms of the Fourier coefficients from $|\tau|^2$ as

$$\mathcal{A}_{\text{LL}}(\phi) \equiv \frac{[\sigma^{\rightarrow\Rightarrow}(\phi) + \sigma^{\leftarrow\Leftarrow}(\phi)] - [\sigma^{\leftarrow\Rightarrow}(\phi) + \sigma^{\rightarrow\Leftarrow}(\phi)]}{[\sigma^{\rightarrow\Rightarrow}(\phi) + \sigma^{\leftarrow\Leftarrow}(\phi)] + [\sigma^{\leftarrow\Rightarrow}(\phi) + \sigma^{\rightarrow\Leftarrow}(\phi)]} \tag{3.22}$$

$$= \frac{\dfrac{K_{\text{BH}}}{\mathcal{P}(\phi)} \displaystyle\sum_{n=0}^{1} c_{n,\text{LP}}^{\text{BH}} \cos(n\phi) + K_{\text{DVCS}} \displaystyle\sum_{n=0}^{1} c_{n,\text{LP}}^{\text{DVCS}} \cos(n\phi) - \dfrac{e_\ell K_{\mathcal{I}}}{\mathcal{P}(\phi)} \displaystyle\sum_{n=0}^{2} c_{n,\text{LP}}^{\mathcal{I}} \cos(n\phi)}{\dfrac{1}{\mathcal{P}(\phi)} \left[K_{\text{BH}} \displaystyle\sum_{n=0}^{2} c_{n,\text{u}}^{\text{BH}} \cos(n\phi) - e_\ell K_{\mathcal{I}} \displaystyle\sum_{n=0}^{3} c_{n,\text{u}}^{\mathcal{I}} \cos(n\phi)\right] + K_{\text{DVCS}} \displaystyle\sum_{n=0}^{2} c_{n,\text{u}}^{\text{DVCS}} \cos(n\phi)}.$$

It receives contributions in the numerator from the $c_{n,\text{LP}}^{\text{BH}}$ coefficients from $|\tau_{\text{BH}}|^2$ which will not be presented here. The coefficients from $|\tau_{\text{DVCS}}|^2$ and $\mathcal{I}$ are written as

$$c_{0,\text{LP}}^{\text{DVCS}} = 2\lambda\Lambda y(2-y)\, \Re e\, \mathcal{C}_{\text{LP}}^{\text{DVCS}}(\mathcal{F}, \mathcal{F}^*), \tag{3.23}$$

$$c_{1,\text{LP}}^{\text{DVCS}} = \frac{8\lambda\Lambda\mathcal{K}y}{(2-x_{\text{B}})(2-y)}\, \Re e\, \mathcal{C}_{\text{LP}}^{\text{DVCS}} \left(\mathcal{F}^{\text{eff}}, \mathcal{F}^*\right), \tag{3.24}$$

$$c_{0,\text{LP}}^{\mathcal{I}} = -8\lambda\Lambda\mathcal{K}^2 y \left(\frac{(2-y)^2}{1-y} + 2\right) \Re e\, \mathcal{C}_{\text{LP}}^{\mathcal{I}}(\mathcal{F}), \tag{3.25}$$

$$c_{1,\text{LP}}^{\mathcal{I}} = 8\lambda\Lambda\mathcal{K}y(2-y)\, \Re e\, \mathcal{C}_{\text{LP}}^{\mathcal{I}}(\mathcal{F}), \tag{3.26}$$

$$c_{2,\text{LP}}^{\mathcal{I}} = -\frac{16\lambda\Lambda\mathcal{K}^2 y}{2-x_{\text{B}}}\, \Re e\, C_{\text{LP}}^{\mathcal{I}} \left(\mathcal{F}^{\text{eff}}\right), \tag{3.27}$$

where $\lambda = \pm 1$ denotes the sign of the beam helicity. The $c_{0,\text{LP}}^{\mathcal{I}}$ amplitude receives an additional twist–2 contribution from $\mathcal{C}_{\text{LP}}^{\mathcal{I}}$, which is suppressed by a factor of $\frac{x_{\text{B}}}{Q^2}$, and as such is neglected in this discussion.

Beam-Helicity Asymmetry Arising from $|\tau_{\mathbf{DVCS}}|^2$ and $\mathcal{I}$.

The beam-helicity asymmetry $\mathcal{A}_{\mathrm{LU}}$ is dependent on the beam polarisation averaged over all target states. This asymmetry is expressed in terms of the Fourier coefficients from $|\tau_{\mathrm{DVCS}}|^2$ and $\mathcal{I}$ as

$$\mathcal{A}_{\mathrm{LU}}(\phi) \equiv \frac{[\sigma^{\rightarrow\Leftarrow}(\phi) + \sigma^{\rightarrow\Rightarrow}(\phi)] - [\sigma^{\leftarrow\Leftarrow}(\phi) + \sigma^{\leftarrow\Rightarrow}(\phi)]}{[\sigma^{\rightarrow\Leftarrow}(\phi) + \sigma^{\rightarrow\Rightarrow}(\phi)] + [\sigma^{\leftarrow\Leftarrow}(\phi) + \sigma^{\leftarrow\Rightarrow}(\phi)]} \tag{3.28}$$

$$= \frac{K_{\mathrm{DVCS}}\, s_{1,\mathrm{u}}^{\mathrm{DVCS}} \sin\phi - \dfrac{e_\ell K_{\mathcal{I}}}{\mathcal{P}(\phi)} \displaystyle\sum_{n=1}^{2} s_{n,\mathrm{u}}^{\mathcal{I}} \sin(n\phi)}{\dfrac{1}{\mathcal{P}(\phi)}\left[K_{\mathrm{BH}}\displaystyle\sum_{n=0}^{2} c_{n,\mathrm{u}}^{\mathrm{BH}} \cos(n\phi) - e_\ell K_{\mathcal{I}}\displaystyle\sum_{n=0}^{3} c_{n,\mathrm{u}}^{\mathcal{I}} \cos(n\phi)\right] + K_{\mathrm{DVCS}}\displaystyle\sum_{n=0}^{2} c_{n,\mathrm{u}}^{\mathrm{DVCS}} \cos(n\phi)},$$

with the relevant Fourier coefficients

$$s_{1,\mathrm{u}}^{\mathrm{DVCS}} = \frac{-8\lambda\mathcal{K}y}{2-x_{\mathrm{B}}}\,\Im m\,\mathcal{C}_{\mathrm{u}}^{\mathrm{DVCS}}\left(\mathcal{F}^{\mathrm{eff}},\mathcal{F}^*\right), \tag{3.29}$$

$$s_{1,\mathrm{u}}^{\mathcal{I}} = 8\lambda\mathcal{K}y(2-y)\,\Im m\,\mathcal{C}_{\mathrm{u}}^{\mathcal{I}}(\mathcal{F}), \tag{3.30}$$

$$s_{2,\mathrm{u}}^{\mathcal{I}} = -\frac{16\lambda\mathcal{K}^2 y}{2-x_{\mathrm{B}}}\,\Im m\,\mathcal{C}_{\mathrm{u}}^{\mathcal{I}}\left(\mathcal{F}^{\mathrm{eff}}\right). \tag{3.31}$$

3.3 Linking Fourier Coefficients to GPDs

The Fourier coefficients arising from $|\tau_{\mathrm{DVCS}}|^2$ and $\mathcal{I}$, and appearing in the numerators of the asymmetries introduced in the previous section, are all expressed in terms of $\mathcal{C}$-functions. These exhibit different dependences on kinematics variables and twist–2 and effective twist–3 CFFs integrated over x.

The $\mathcal{C}^{\mathcal{I}}$ $\left(\mathcal{C}^{\mathrm{DVCS}}\right)$ functions are linear (bilinear) with respect to CFFs. There are three functions of particular interest: $\mathcal{C}_{\mathrm{LP}}^{\mathrm{DVCS}}$, $\mathcal{C}_{\mathrm{LP}}^{\mathcal{I}}$, and $\mathcal{C}_{\mathrm{u}}^{\mathcal{I}}$. These all relate to CFFs $\mathcal{H}$, $\mathcal{E}$, $\widetilde{\mathcal{H}}$ and $\widetilde{\mathcal{E}}$ at twist–2 and effective twist–3 level as

$$\mathcal{C}_{\mathrm{LP}}^{\mathrm{DVCS}} = \frac{1}{(2-x_{\mathrm{B}})^2}\left[4(1-x_{\mathrm{B}})\left(\mathcal{H}\widetilde{\mathcal{H}}^* + \widetilde{\mathcal{H}}\mathcal{H}^*\right) - x_{\mathrm{B}}^2\left(\mathcal{H}\widetilde{\mathcal{E}}^* + \widetilde{\mathcal{E}}\mathcal{H}^* + \widetilde{\mathcal{H}}\mathcal{E}^* + \mathcal{E}\widetilde{\mathcal{H}}^*\right)\right.$$

$$\left. - x_{\mathrm{B}}\left(\frac{x_{\mathrm{B}}^2}{2} + (2-x_{\mathrm{B}})\frac{t}{4M^2}\right)\left(\mathcal{E}\widetilde{\mathcal{E}}^* + \widetilde{\mathcal{E}}\mathcal{E}^*\right)\right], \tag{3.32}$$

$$\mathcal{C}_{\mathrm{LP}}^{\mathcal{I}} = \frac{x_{\mathrm{B}}(F_1+F_2)}{2-x_{\mathrm{B}}}\left(\mathcal{H} + \frac{x_{\mathrm{B}}}{2}\mathcal{E}\right) + F_1\widetilde{\mathcal{H}} - \frac{x_{\mathrm{B}}}{2-x_{\mathrm{B}}}\left(\frac{x_{\mathrm{B}}}{2}F_1 + \frac{t}{4M^2}F_2\right)\widetilde{\mathcal{E}}, \tag{3.33}$$

$$\mathcal{C}_{\mathrm{u}}^{\mathcal{I}} = F_1\mathcal{H} + \frac{x_{\mathrm{B}}}{2-x_{\mathrm{B}}}(F_1+F_2)\widetilde{\mathcal{H}} - \frac{t}{4M^2}F_2\mathcal{E}, \tag{3.34}$$

where $\mathcal{F}^*$ represents the complex conjugate of CFF $\mathcal{F}$.

This linearity with respect to CFFs, and the dominance of the $\mathcal{I}$ contribution over that of the $|\tau_{\mathrm{DVCS}}|^2$ term at HERMES, allow the possibility to access GPD-related information via the $\mathcal{C}^{\mathcal{I}}$-function.

The other functions, $\mathcal{C}_{\mathrm{T}}^{\mathcal{I}}$ and $\mathcal{C}_{\mathrm{T}}^{\mathrm{DVCS}}$, appear at leading-gluon-twist level and are suppressed by $\frac{\alpha_{\mathrm{s}}}{\pi}$. These are listed in full in Ref. [27]. The $\mathcal{C}$-functions of importance in this analysis will be revisited in Section 5.6 in relation to the ϕ-dependent asymmetry amplitudes extracted from data.

3.4 Overview of HERMES DVCS Results

HERMES has extracted observables relating to GPDs from asymmetries with dependences on combinations of beam charge, beam helicity and target polarisation. Initial HERMES results of the Beam-Spin Asymmetry (BSA) [20] and Beam-Charge Asymmetry (BCA) [21] have been superceded by more precise measurements from data taken using both beam charges [23, 24], allowing for the first time, the separation of contributions from $|\tau_{\mathrm{DVCS}}|^2$ and $\mathcal{I}$.

HERMES has also published measurements of asymmetry amplitudes associated with a transversely polarised hydrogen target [22] and a number of unpolarised nuclear targets [25]. Figure 3.4 summarises the leading-order DVCS-related asymmetry amplitudes extracted from unpolarised or polarised hydrogen and deuterium gas targets. These amplitudes are integrated over all kinematics in the HERMES acceptance *i.e.* extracted in a single bin. An unpublished extraction of the $\mathcal{A}_{\mathrm{UL}}$ has been performed [61]. The results of this thesis supercede this measurement in addition to extracting $\mathcal{A}_{\mathrm{LL}}$ for the first time. These asymmetry amplitudes will be described in the following section with their relations to GPDs and the Fourier coefficients in the expansion of the cross-section.
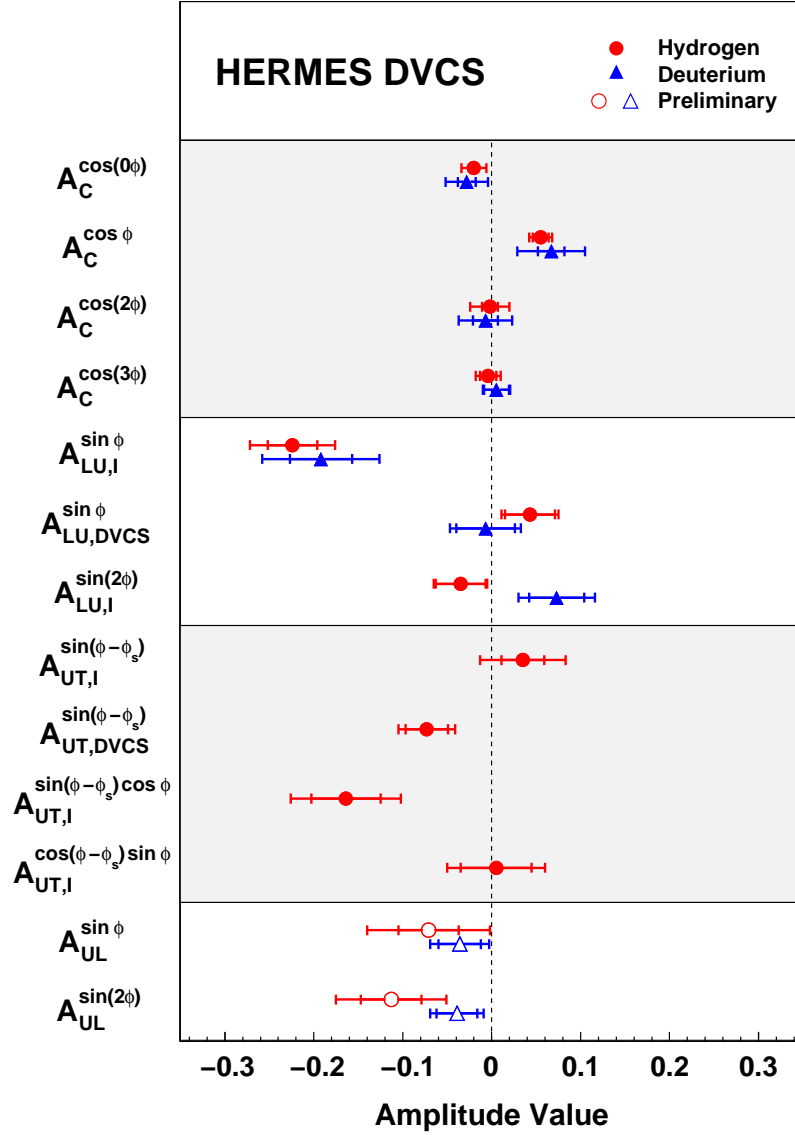
Figure 3.4: Summary of the extracted DVCS-related asymmetry amplitudes from HERMES data. From top to bottom: amplitudes of $\mathcal{A}_{\mathrm{C}}$, $\mathcal{A}_{\mathrm{LU}}$, and $\mathcal{A}_{\mathrm{UT}}$ using both electron and positron data, and an unpublished result of the positron-only $\mathcal{A}_{\mathrm{UL}}$. These are shown integrated over all kinematics in the HERMES acceptance with error bars showing the statistical (inner) and systematic (outer) uncertainties. Open (Filled) points relate to preliminary (published) results from hydrogen (circles) and deuterium (triangles) targets.

3.4.1 Simultaneous Extraction of Beam Helicity and Charge Asymmetries

The beam-helicity asymmetry (formerly labelled BSA) has been extracted at a number of experiments [20, 62]. Equation 3.6 highlights the dependence of $\mathcal{I}$ on the charge of the lepton beam. Using HERMES data taken with both electron and positron beams, it is possible to extract two new beam-helicity asymmetries: the 'charge-difference' $\mathcal{A}_{\mathrm{LU}}^{\mathcal{I}}$ and the 'charge-average' $\mathcal{A}_{\mathrm{LU}}^{\mathrm{DVCS}}$ which are Fourier expanded in ϕ as

$$
\begin{aligned}
\mathcal{A}_{\mathrm{LU}}^{\mathcal{I}}(\phi) &\equiv \frac{[\sigma^{\rightarrow+}(\phi) + \sigma^{\leftarrow-}(\phi)] - [\sigma^{\leftarrow+}(\phi) + \sigma^{\rightarrow-}(\phi)]}{[\sigma^{\rightarrow+}(\phi) + \sigma^{\leftarrow-}(\phi)] + [\sigma^{\leftarrow+}(\phi) + \sigma^{\rightarrow-}(\phi)]} \\
&= \frac{-\dfrac{K_{\mathcal{I}}}{\mathcal{P}(\phi)} \displaystyle\sum_{n=1}^{2} s_{n,\mathrm{u}}^{\mathcal{I}} \sin(n\phi)}{\dfrac{K_{\mathrm{BH}}}{\mathcal{P}(\phi)} \displaystyle\sum_{n=0}^{2} c_{n,\mathrm{u}}^{\mathrm{BH}} \cos(n\phi) + K_{\mathrm{DVCS}} \displaystyle\sum_{n=0}^{2} c_{n,\mathrm{u}}^{\mathrm{DVCS}} \cos(n\phi)} ,
\end{aligned}
\tag{3.35}
$$

$$
\begin{aligned}
\mathcal{A}_{\mathrm{LU}}^{\mathrm{DVCS}}(\phi) &\equiv \frac{[\sigma^{\rightarrow+}(\phi) + \sigma^{\rightarrow-}(\phi)] - [\sigma^{\leftarrow+}(\phi) + \sigma^{\leftarrow-}(\phi)]}{[\sigma^{\rightarrow+}(\phi) + \sigma^{\rightarrow-}(\phi)] + [\sigma^{\leftarrow+}(\phi) + \sigma^{\leftarrow-}(\phi)]} \\
&= \frac{K_{\mathrm{DVCS}} s_{1,\mathrm{u}}^{\mathrm{DVCS}} \sin\phi}{\dfrac{K_{\mathrm{BH}}}{\mathcal{P}(\phi)} \displaystyle\sum_{n=0}^{2} c_{n,\mathrm{u}}^{\mathrm{BH}} \cos(n\phi) + K_{\mathrm{DVCS}} \displaystyle\sum_{n=0}^{2} c_{n,\mathrm{u}}^{\mathrm{DVCS}} \cos(n\phi)} ,
\end{aligned}
\tag{3.36}
$$

where the superscript $+(-)$ denotes a positron (electron) beam. The results from the $1996 - 2005$ HERMES hydrogen and deuterium data sets are shown in Figs. 3.5 and 3.6 as a function of $-t$, x_{B}, and Q^2 for the $\mathcal{I}$ and $|\tau_{\mathrm{DVCS}}|^2$ contributions respectively [23, 24, 63, 64]. A large leading-twist $A_{\mathrm{LU},\mathcal{I}}^{\sin\phi}$ amplitude of $-0.224 \pm 0.028(\mathrm{stat}) \pm 0.020(\mathrm{syst})$ $[-0.192 \pm 0.035 \pm 0.031]$ was observed for the hydrogen [deuterium] target. Results from both targets are shown to agree across the kinematic range. However, calculations from the GPD model in Ref. [49] fail to describe either set of data with predictions of amplitudes twice as large as those observed. As expected, the $A_{\mathrm{LU},\mathcal{I}}^{\sin(2\phi)}$ and $A_{\mathrm{LU},\mathrm{DVCS}}^{\sin\phi}$ amplitudes are suppressed with respect to the $A_{\mathrm{LU},\mathcal{I}}^{\sin\phi}$ amplitude. There is currently no theoretical explanation for the different signs of the $A_{\mathrm{LU},\mathcal{I}}^{\sin(2\phi)}$ extracted from hydrogen and deuterium data.

The analysis simultaneously extracted the BCA which is defined as

$$
\begin{aligned}
\mathcal{A}_{\mathrm{C}}(\phi) &\equiv \frac{[\sigma^{\rightarrow+}(\phi) + \sigma^{\leftarrow+}(\phi)] - [\sigma^{\leftarrow-}(\phi) + \sigma^{\leftarrow-}(\phi)]}{[\sigma^{\rightarrow+}(\phi) + \sigma^{\leftarrow+}(\phi)] + [\sigma^{\leftarrow-}(\phi) + \sigma^{\leftarrow-}(\phi)]} \\
&= \frac{-\dfrac{K_{\mathcal{I}}}{\mathcal{P}(\phi)} \displaystyle\sum_{n=0}^{3} c_{n,\mathrm{u}}^{\mathcal{I}} \cos(n\phi)}{\dfrac{K_{\mathrm{BH}}}{\mathcal{P}(\phi)} \displaystyle\sum_{n=0}^{2} c_{n,\mathrm{u}}^{\mathrm{BH}} \cos(n\phi) + K_{\mathrm{DVCS}} \displaystyle\sum_{n=0}^{2} c_{n,\mathrm{u}}^{\mathrm{DVCS}} \cos(n\phi)} .
\end{aligned}
\tag{3.37}
$$
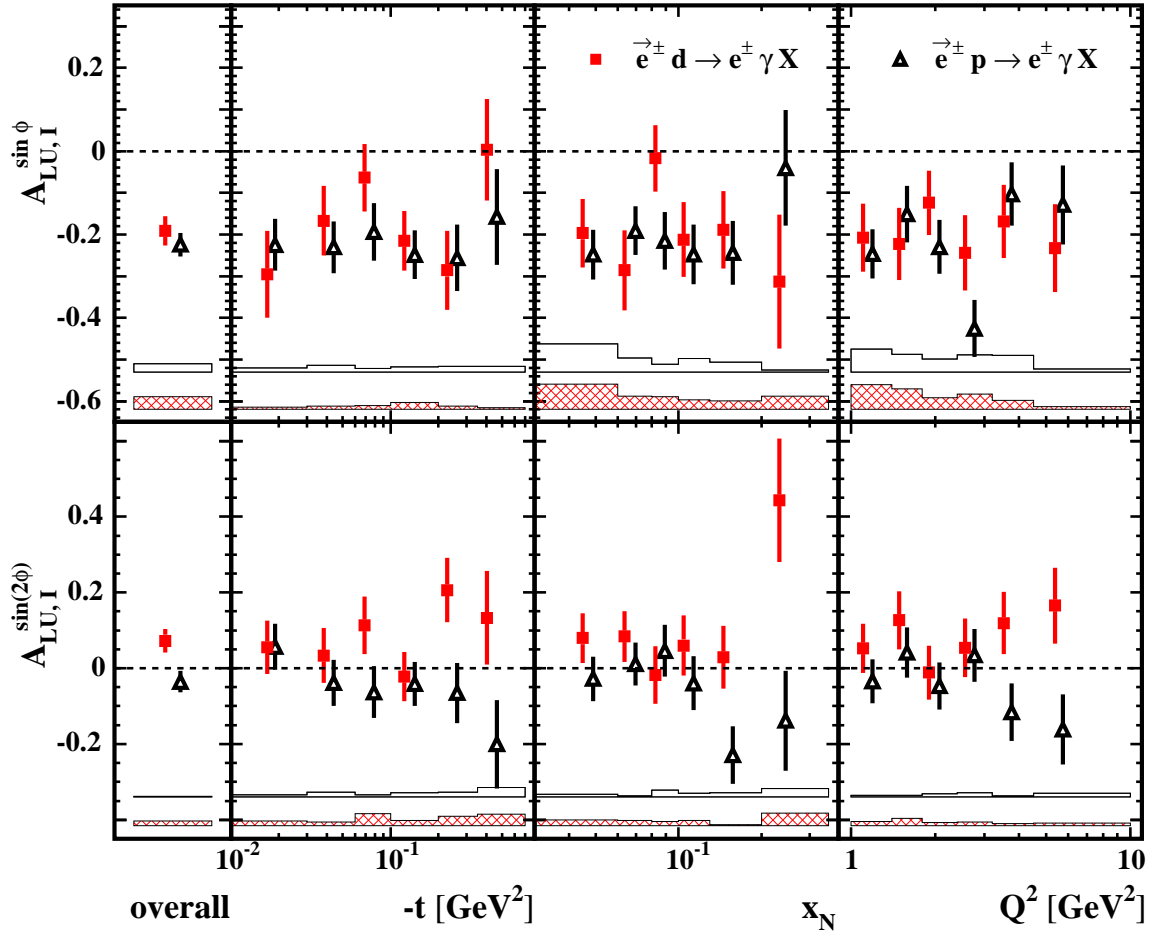
Figure 3.5: The $A_{\text{UL},\mathcal{I}}^{\sin(n\phi)}$ amplitudes of the beam-helicity asymmetry sensitive to $\mathcal{I}$, in bins of $-t$, x_{B}, and Q^2 extracted from hydrogen (triangles) and deuterium target data (squares) [24]. The error bars (bands) represent the statistical (systematic) uncertainties, with an additional $2.4\%\,(2.8\%)$ scale uncertainty arising from the beam polarisation measurement for the deuteron (proton) data. These amplitudes are related to Fourier coefficients appearing in the numerator of Eq. 3.35.

The $A_{\text{C}}^{\cos(n\phi)}$ amplitudes are presented in Fig. 3.7. No significant differences are observed between both sets of amplitudes. However, in the final two $-t$ bins, the leading-twist $A_{\text{C}}^{\cos\phi}$ amplitude from the deuterium data are smaller in amplitude than those from hydrogen. This may be due to contributions from scattering off a constituent neutron in the deuteron [24].

The key amplitudes of interest in Figs. $3.5 - 3.7$ are the $A_{\text{LU},\mathcal{I}}^{\sin\phi}$ and $A_{\text{C}}^{\cos\phi}$ which relate to the imaginary and real parts, respectively, of $\mathcal{C}_{\text{LP}}^{\mathcal{I}}$. This is shown in the respective $s_{1,\text{u}}^{\mathcal{I}}$ (Eq. 3.30) and $c_{1,\text{u}}^{\mathcal{I}}$ Fourier coefficients where

$$c_{1,\text{u}}^{\mathcal{I}} = 8\mathcal{K}\left(2 - 2y + y^2\right)\Re e\,\mathcal{C}_{\text{LP}}^{\mathcal{I}}\,. \tag{3.38}$$
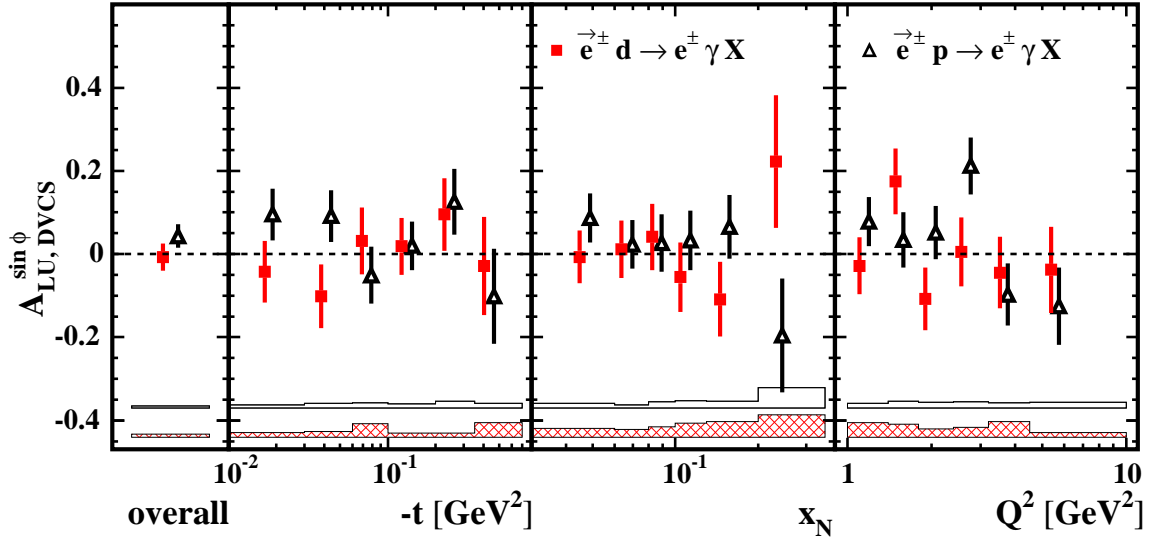
Figure 3.6: The $A_{UL,DVCS}^{\sin\phi}$ amplitude of the beam-helicity asymmetry sensitive to $|\tau_{DVCS}|^2$, in bins of $-t$, x_B, and Q^2 extracted from hydrogen (triangles) and deuterium target data (squares) [24]. The error bars (bands) represent the statistical (systematic) uncertainties, with an additional 2.4% (2.8%) scale uncertainty arising from the beam polarisation measurement for the deuteron (proton) data. These amplitudes are related to the Fourier coefficient appearing in the numerator of Eq. 3.36.

From Eq. 3.34 it is shown that at HERMES kinematics, these asymmetry amplitudes provide access to the imaginary and real parts of dominant CFF $\mathcal{H}$.
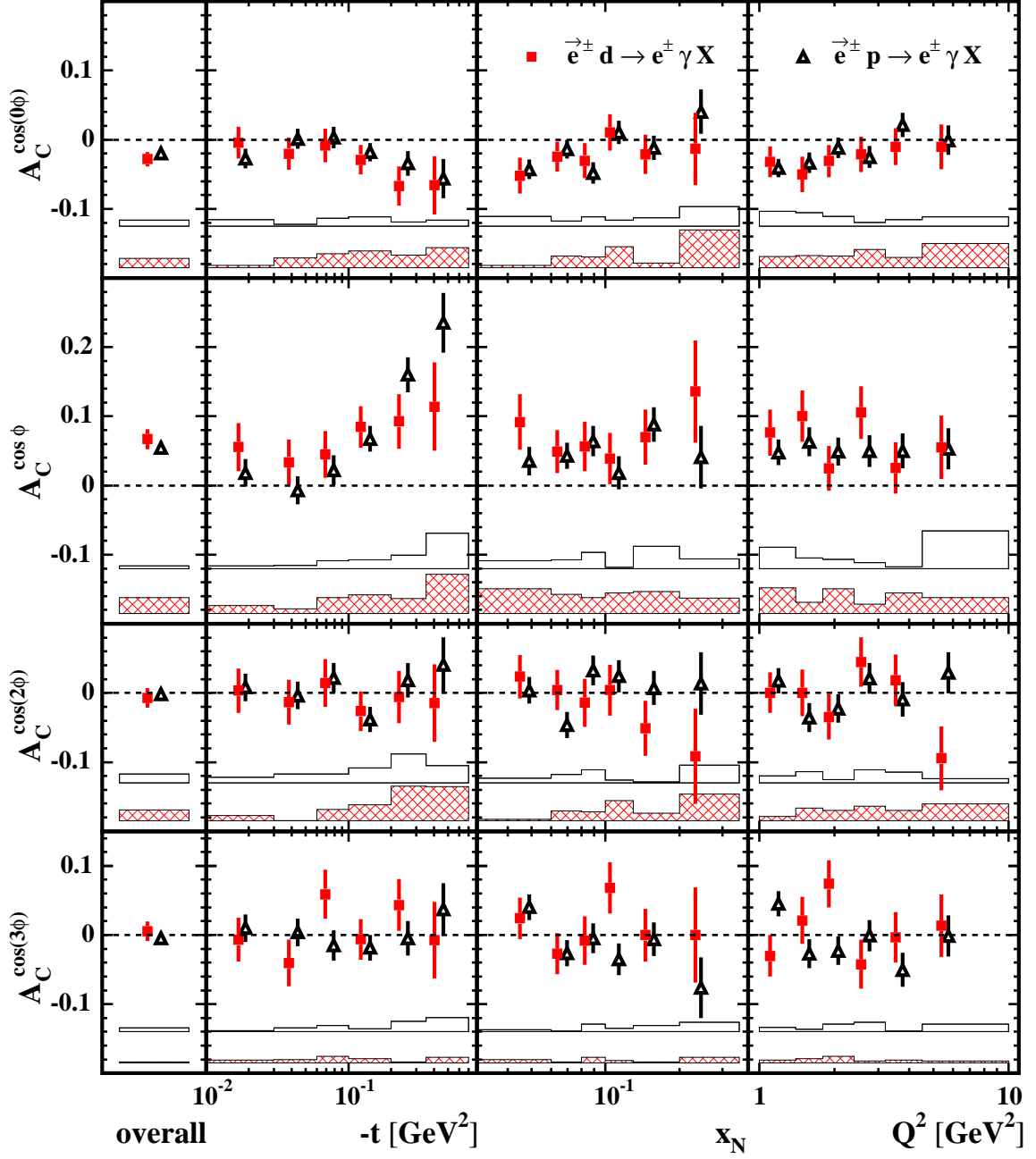
Figure 3.7: The $A_C^{\cos(n\phi)}$ amplitudes of the beam-charge asymmetry, sensitive to $\mathcal{I}$, in bins of $-t$, x_B, and Q^2, extracted from hydrogen (triangles) and deuterium target data (squares) [24]. The error bars (bands) represent the statistical (systematic) uncertainties. All amplitudes relate to Fourier coefficients appearing in Eq. 3.37.

3.4.2 Simultaneous Extraction of Transverse Target Spin Asymmetries

HERMES has published results of the combined extraction of the BCA and transversely polarised target asymmetries $A_{\mathrm{UT}}^{\mathcal{I}}$ and $A_{\mathrm{UT}}^{\mathrm{DVCS}}$ arising from $\mathcal{I}$ and $|\tau_{\mathrm{DVCS}}|^2$ respectively [22, 65, 66]. These azimuthal asymmetries are related to Fourier coefficients as

$$
\begin{aligned}
\mathcal{A}_{\mathrm{UT}}^{\mathcal{I}}(\phi, \phi_s) &\equiv \frac{[\sigma^+(\phi, \phi_s) + \sigma^-(\phi, \phi_s + \pi)] - [\sigma^-(\phi, \phi_s) + \sigma^+(\phi, \phi_s + \pi)]}{[\sigma^+(\phi, \phi_s) + \sigma^-(\phi, \phi_s + \pi)] - [\sigma^-(\phi, \phi_s) + \sigma^+(\phi, \phi_s + \pi)]} \quad (3.39) \\
&= \frac{-\dfrac{e_\ell K_{\mathcal{I}}}{\mathcal{P}(\phi)} \left[\displaystyle\sum_{n=0}^{3} c_{n,\mathrm{UT}}^{\mathcal{I}} \sin\varphi \cos(n\phi) + \sum_{n=1}^{3} s_{n,\mathrm{UT}}^{\mathcal{I}} \cos\varphi \sin(n\phi) \right]}{\dfrac{K_{\mathrm{BH}}}{\mathcal{P}(\phi)} \displaystyle\sum_{n=0}^{2} c_{n,\mathrm{u}}^{\mathrm{BH}} \cos(n\phi) + K_{\mathrm{DVCS}} \sum_{n=0}^{2} c_{n,\mathrm{u}}^{\mathrm{DVCS}} \cos(n\phi)}, \\[2ex]
\mathcal{A}_{\mathrm{UT}}^{\mathrm{DVCS}}(\phi, \phi_s) &\equiv \frac{[\sigma^+(\phi, \phi_s) + \sigma^-(\phi, \phi_s)] - [\sigma^+(\phi, \phi_s + \pi) + \sigma^-(\phi, \phi_s + \pi)]}{[\sigma^+(\phi, \phi_s) + \sigma^-(\phi, \phi_s)] + [\sigma^+(\phi, \phi_s + \pi) + \sigma^-(\phi, \phi_s + \pi)]} \quad (3.40) \\
&= \frac{K_{\mathrm{DVCS}} \left[\displaystyle\sum_{n=0}^{2} c_{n,\mathrm{UT}}^{\mathrm{DVCS}} \sin\varphi \cos(n\phi) + \sum_{n=1}^{2} s_{n,\mathrm{UT}}^{\mathrm{DVCS}} \cos\varphi \sin(n\phi) \right]}{\dfrac{K_{\mathrm{BH}}}{\mathcal{P}(\phi)} \displaystyle\sum_{n=0}^{2} c_{n,\mathrm{u}}^{\mathrm{BH}} \cos(n\phi) + K_{\mathrm{DVCS}} \sum_{n=0}^{2} c_{n,\mathrm{u}}^{\mathrm{DVCS}} \cos(n\phi)},
\end{aligned}
$$

where ϕ_s is the azimuthal angle between the lepton-scattering plane and the transverse target polarisation vector, and $\varphi = \phi - \phi_s$. The amplitudes of particular interest are $A_{\mathrm{UT},\mathcal{I}}^{\sin\varphi\cos\phi}$ and $A_{\mathrm{UT},\mathcal{I}}^{\cos\varphi\sin\phi}$ which relate respectively to the Fourier coefficients:

$$
c_{1,\mathrm{UT}}^{\mathcal{I}} \propto \Im m \left\{ (2 - x_{\mathrm{B}}) F_1 \mathcal{E} - 4 \left(\frac{1 - x_{\mathrm{B}}}{2 - x_{\mathrm{B}}} \right) F_2 \mathcal{H} \right\}, \quad (3.41)
$$

$$
s_{1,\mathrm{UT}}^{\mathcal{I}} \propto \Im m \left\{ \frac{4(1 - x_{\mathrm{B}})}{2 - x_{\mathrm{B}}} F_2 \widetilde{\mathcal{H}} - x_{\mathrm{B}} (F_1 + \xi F_2) \widetilde{\mathcal{E}} \right\}. \quad (3.42)
$$

Equation 3.41 highlights the unique opportunity that arises to access information on CFFs $\mathcal{E}$ and $\widetilde{\mathcal{E}}$ which are kinematically suppressed at HERMES via all other coefficients. Extracted amplitudes relating to these Fourier coefficients are presented in Fig. 3.8 with predictions from the discussed GPD model. It is shown that the $A_{\mathrm{UT},\mathcal{I}}^{\sin\varphi\cos\phi}$ amplitude is sensitive to J_u from the double-distribution parametrisation of GPD E via $c_{1,\mathrm{UT}}^{\mathcal{I}}$. This can help provide a model-dependent constraint on the quark orbital angular momenta contribution to the nucleon spin [3].
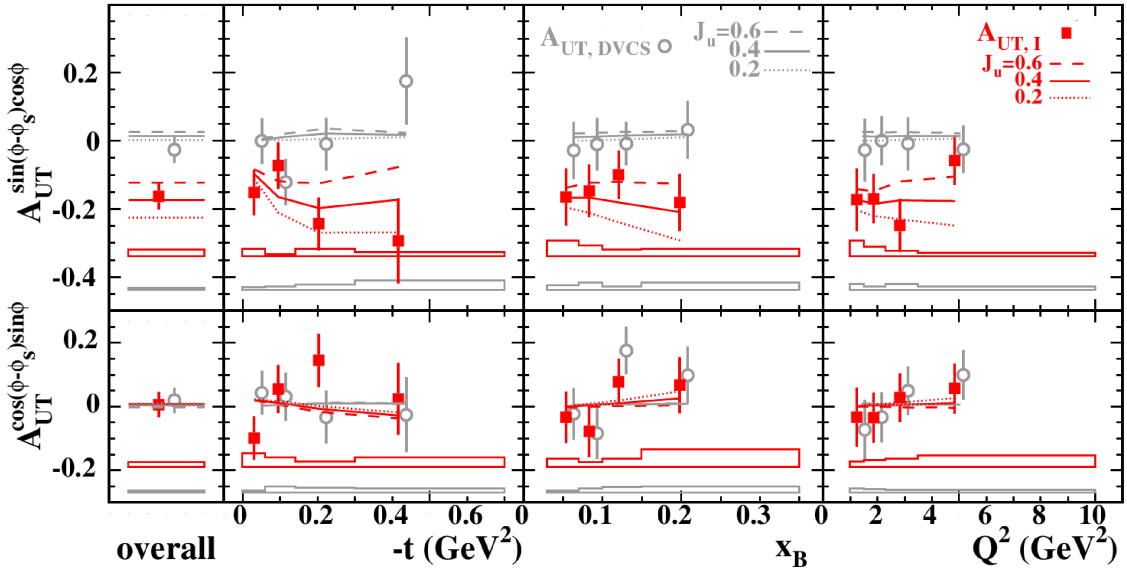
Figure 3.8: The $A_{\mathrm{UT}}^{\sin(\phi-\phi_s)\cos\phi}$ and $A_{\mathrm{UT}}^{\cos(\phi-\phi_s)\sin\phi}$ amplitudes of the transversely polarised target asymmetry sensitive to $\mathcal{I}$ (filled squares) and $|\tau_{\mathrm{DVCS}}|^2$ (open circles) from hydrogen data, in bins of $-t$, x_{B}, and Q^2. The error bars (bands) represent the statistical (systematic) uncertainties, with an additional 8.1% scale uncertainty arising from the target polarisation measurement. Predictions from a GPD-model [49] for certain J_u values (with $J_d = 0$) are presented in comparison with the data [22].

Chapter 4

The HERMES Experiment

The HERMES (HERa MEasurement of Spin) experiment, situated on the Hadron Elektron Ring Anlage (HERA) storage ring at the Deutches Elektronen Synchrotron (DESY) facility in Hamburg, Germany, took data for the first time in 1995 [67]. It continued to run until the final HERA shutdown at the end of July 2007. During this time, the detector setup was improved to expand the original physics programme which was aimed at investigating the questions which arose in the wake of the EMC findings [7,8].

HERMES was one of four active experiments on the HERA ring, shown in Fig. 4.1. Both HERMES and HERA-B were fixed target experiments using the electron/positron and proton beams, respectively. The other two experiments, H1 and ZEUS, were collider experiments using both HERA beams orbiting in opposite directions and brought into collision at the detector halls. The HERMES, H1 and ZEUS experiments continued to run until the end of HERA while HERA-B was decommissioned in 2003.

In this chapter the main features and operation of the HERA storage ring will be outlined along with the HERMES experimental setup, focussing on the longitudinally polarised gas target and key subdetectors, vital to the DVCS analysis presented in this thesis.

The HERMES Coordinate System

Throughout this thesis, important kinematic variables will be defined and further references will be made that rely on a knowledge of the HERMES coordinate system. This right-handed coordinate system is defined with positive z direction originating from the target cell and passing 'downstream' along the beam-line in the direction of the forward spectrometer. Azimuthal angles ($0 \leq \phi \leq 2\pi \, \text{rad}$) are defined in the x-y plane, with x increasing to the left looking downstream, and polar angles ($0 \leq \theta \leq \pi \, \text{rad}$) are conven-
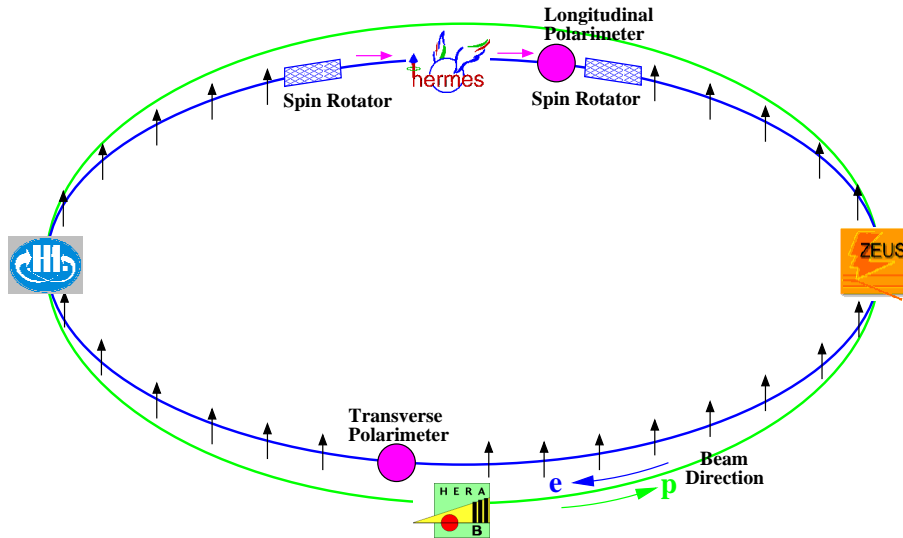
Figure 4.1: Schematic of the HERA storage ring showing the orbit and polarisation directions of the electron/positron and proton beams. The location of the HERMES experiment is shown in relation to the beam polarimeters and spin-rotators.

tionally defined in the y-z plane.

4.1 The HERA Storage Ring

The HERA storage ring (see Fig. 4.1) at DESY, with a circumference of 6.3 km, provided the four experiments introduced previously with a 27.57 GeV longitudinally polarised electron/positron beam and/or a 920 GeV proton beam. The HERMES experiment started taking data in 1995 using a positron beam until 2000, with the exception of a short period in 1998 when electron data were taken. Despite the initial intention to use an electron beam, the positron beam was preferred as electrons had a tendency to attract positively-charged dust which accumulated during acceleration around the ring. This caused the lifetime of the electron beam to diminish significantly. Throughout 2001, the vacuum system at HERA was upgraded and for the following period of $2002 - 2004$, positrons were accelerated. An electron beam was then used until mid-2006, when HERA returned to positrons for the final year of data-taking.

The Polarised Electron/Positron Beam

The HERA storage ring was filled with either electrons or positrons which were accelerated to energies of 27.57 GeV by a multi-stage process. The beam was initially accelerated through the LinAc-II linear accelerator at DESY to an energy of 450 MeV before being

injected into the DESY-II storage ring. Here, the beam underwent further acceleration to 7.5 GeV. For the penultimate stage of this process, the leptons were transferred to the PETRA storage ring and accelerated to 12 GeV. Before injection into HERA they were finally accelerated to the operating energy of 27.57 GeV.

The leptons were unpolarised when injected into HERA by the PETRA pre-accelerator. The polarisation is defined as an asymmetry in the spin orientation of the beam leptons, *i.e.*

$$P = \frac{N^\uparrow - N^\downarrow}{N^\uparrow + N^\downarrow}. \tag{4.1}$$

It is a measure of the number of leptons N with a particular spin state. This increased exponentially with time τ as

$$P = P_{\text{ST}} \left(1 - e^{-\tau/\tau_{\text{ST}}}\right). \tag{4.2}$$

At HERA, a transverse polarisation of the lepton beam built up naturally via the Sokolov-Ternov effect [68], an asymmetry in the small-flip probability in the emission of synchrotron radiation, as the leptons orbited the storage ring. This effect accumulated over successive orbits providing a large overall polarisation. From Eq. 4.2, $P_{\text{ST}} = \frac{8\sqrt{3}}{15}$ is the maximum polarisation possible from this effect and is equal to ~92.4% for an ideal machine. The characteristic polarisation rise-time is given by

$$\tau_{\text{ST}} = P_{\text{ST}} \left(\frac{m_e \, \rho^3}{\hbar \, c^2 \, r_e \, \gamma^5}\right), \tag{4.3}$$

where ρ is the bending radius of the magnetic field, r_e is the classical electron radius and $\gamma = \frac{E_\ell}{m_e}$ is the Lorentz factor with beam energy E_ℓ and electron mass m_e. Applying Eq. 4.3 to the HERA storage ring gives an optimum rise-time of approximately 37 minutes.

Several depolarising effects limited the maximum polarisation achieved by HERA. These included, but were not limited to:

- Emission of synchrotron radiation which caused oscillations of beam particles. These affected the optimal alignment of the beam particles with the magnetic field. This effect is referred to as 'spin-diffusion' [70].

- Interactions between the electron/positron and proton beams at the H1 and ZEUS experiments.

- Non-perfect alignment of the magnetic field components with respect to the beam orbit. This was due to a number of factors including small inhomogeneities in the magnetic fields and/or small magnet misalignments.
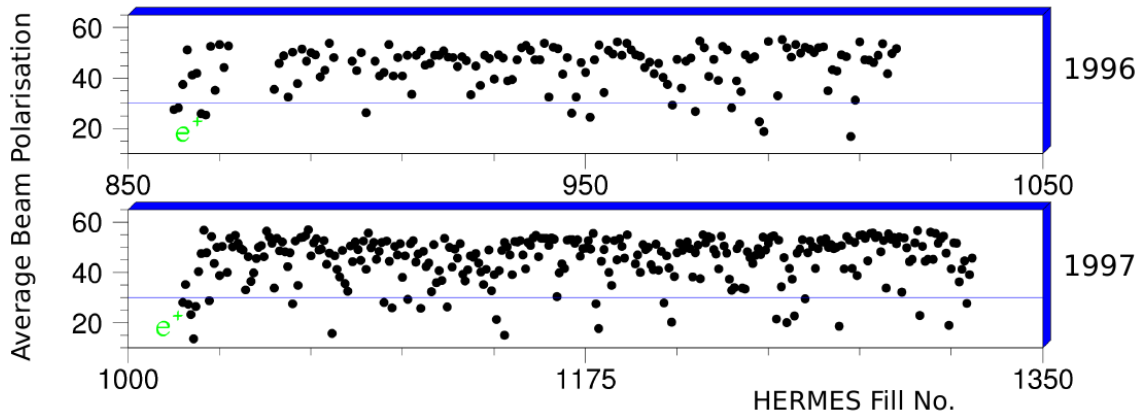
Figure 4.2: Average absolute beam polarisations for each target 'fill' for both the 1996 and 1997 data years used in the analysis presented in this thesis. Figure amended from Ref. [69]

.

These factors conspired to produce a significantly decreased transverse beam polarisation with typical maximum values of around 60%. This is shown in Fig. 4.2 for the data years used in the analysis presented later in this thesis. As these depolarisation effects could not be controlled, it was necessary to continuously monitor the polarisation of the beam. While the Sokolov-Ternov effect produced a transverse polarisation of the lepton beam, the cross-section for this is highly suppressed by a factor of $\frac{1}{\gamma}$ compared to that of a longitudinally polarised lepton beam. For this reason the latter polarisation state was preferred. In order to achieve this, magnets called 'spin-rotators' [71] were installed upstream and downstream of the HERMES experiment on the HERA ring. These spin-rotators (see Fig. 4.1) 'rotated' the spin of the beam through a series of small, angular deflections using horizontal and vertical dipole magnets. This process was performed before entering the HERMES experimental hall, and on leaving the experiment the opposite task of rotating the beam polarisation back to the original transverse direction was performed. The spin-rotators had no adverse effect on the absolute polarisation values measured as they acted only to alter the direction of polarisation. This is shown in Fig. 4.3 which compares measurements from two independent polarimeters at HERA, the Transverse (TPOL) and Longitudinal (LPOL) Polarimeters. This allowed a cross-check of the beam polarisation measurements to be performed. Figure 4.3 also shows the typical achievable $\tau_{\mathrm{ST}} \simeq 40\,\mathrm{minutes}$ and $P_{\mathrm{ST}} \simeq 60\%$ values at HERA.

For the 1996 running period, a single beam polarisation direction was selected. This was reversed every few months for the following data-taking years by realigning the magnets
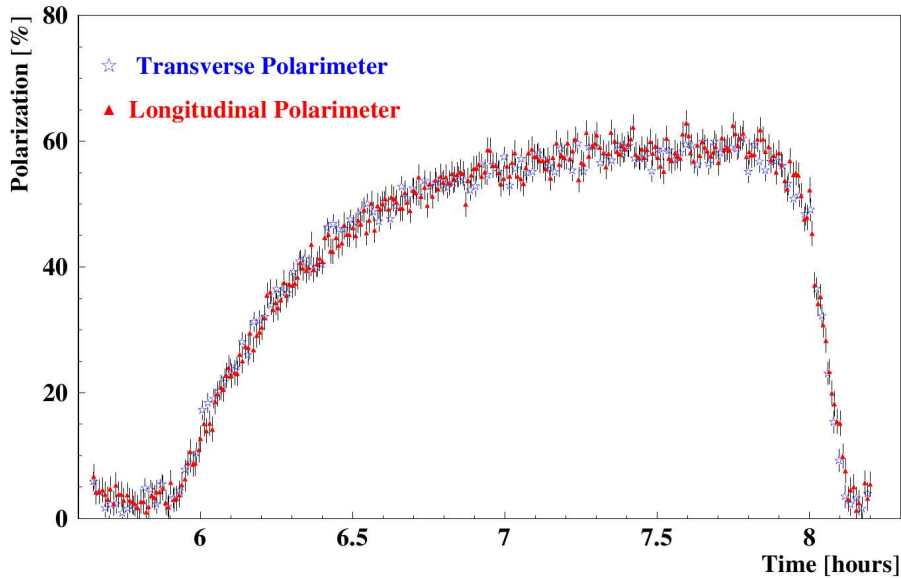
Figure 4.3: Comparison of the independent beam polarisation measurements from the TPOL and LPOL [72]. A transverse polarisation built up via the Sokolov-Ternov effect and typically reached a maximum polarisation of 60% within a rise-time close to 40 minutes. As described in the text, there was no effect observed from the rotation of the spin.

of the spin-rotators. The analysis presented in this thesis (see Chapter 5) involves the simultaneous extraction of three asymmetries which arise from the $e\,p \rightarrow e\,p\,\gamma$ interaction on a longitudinally polarised proton target using a longitudinally polarised positron beam. As these asymmetries depend on the polarisation of the beam, accurate measurements of this property are required. For such measurements the TPOL and LPOL were used to continuously monitor the polarisation at two different regions on the storage ring.

The Transverse Polarimeter (TPOL)

The TPOL [70] was situated close to the site of the HERA-B experiment and relied on the interaction of circularly-polarised laser light with the transverse polarisation direction of the beam. In the HERMES coordinate system this was in the y plane. Asymmetries were measured in the Compton back-scattering distribution of polarised photons incident on the beam. These back-scattered photons from the laser light were detected by calorimeters. The asymmetrical distribution of photons is given by

$$\Delta y\,(E_\gamma) = \Delta S_3\,\Pi_y\,(E_\gamma)\,P_{\ell y}\,, \tag{4.4}$$

and is directly proportional to the circular polarisation ΔS_3 and the analysing power of the polarimeter Π_y, which is itself dependent on the energy of the photon E_γ. The trans-

verse polarisation of the beam $P_{\ell y}$ could be calculated to within 1% statistical accuracy from one minute of data taking. A systematic uncertainty of 3.4% is inherent in this measurement [73].

The Longitudinal Polarimeter (LPOL)

Similarly, the operation of the LPOL, which is described in detail in Ref. [73], used circularly-polarised photons. However, whereas the TPOL observed a spatial asymmetry from these photons, the LPOL measured an energy asymmetry arising from photons incident on the longitudinally polarised lepton beam. This is given by

$$A(\Delta S_3,\, P_{\ell z}) = \Delta S_3\, \Pi_z\, P_{\ell z}\,, \tag{4.5}$$

where Π_z is the analysing power of the LPOL. The polarisation of the beam $P_{\ell z}$ is subject to year-dependent systematic uncertainties of around 2%. However, the LPOL was not operational for the longitudinally polarised proton target data-taking period, so the analysed data do not benefit from this improved accuracy.

The Luminosity Monitor (LUMI)

The luminosity monitor (LUMI) [74] was situated along the beam-line in the calorimeter region of the HERMES spectrometer (shown later in Fig. 4.9) and consisted of two radiation-hard $NaBi(WO_4)_2$ Čerenkov crystal calorimeters, each coupled to photomultipliers. The integrated luminosity of the positron beam was determined from LUMI measurements of two quantities: the luminosity constant C_{LUMI} and the integrated coincidence rate R_{LUMI} of the Bhabha scattering ($e^+e^- \rightarrow e^+e^-$) and Møller annihilation ($e^+e^- \rightarrow 2\gamma$) processes. Here e^- are atomic target electrons.

4.2   The Internal Gas Target

The HERMES polarised target was unlike any in operation at similar deep-inelastic scattering experiments in that it was internal to the storage ring. This allowed a high degree of target purity with minimal contamination from unpolarised nucleons. As HERMES was one of three experiments using the HERA polarised electron/positron beam, the target design was restricted, and as such, a low density gaseous target was chosen to limit losses in beam current. The gaseous nature allowed the target material and density to be changed easily during experimental running and benefited from a lower degree of target

HERMES Target Gas: Integrated Luminosities (pb^{-1})										
Year	$e^\pm$	H	**H$_\parallel$**	H$_\perp$	D	D$_\parallel$	He	N	Ne	Kr	Xe
1996	e^+	24.7	**12.6**	-	46.4	-	14.4	-	-	-	-
1997	e^+	31.9	**37.3**	-	58.1	-	-	51.4	-	-	-
1998	e^-	11.0	-	-	24.0	24.8	-	-	-	0.4	-
1999	e^+	0.3	-	-	7.8	29.2	-	2.0	-	29.5	-
2000	e^+	132.5	-	-	39.3	138.7	32.4	-	85.9	0.8	-
2002	e^+	12.7	-	14.1	11.4	-	-	-	-	12.7	-
2003	e^+	1.5	-	6.1	-	-	-	-	-	1.1	-
2004	e^+	2.9	-	44.2	76.3	-	-	-	-	43.0	30.7
2005	e^-	9.1	-	85.8	70.4	-	-	-	-	19.3	19.6
2006	e^-	245.0	-	-	57.8	-	-	-	-	-	-
2006	e^+	696.2	-	-	193.8	-	-	-	-	-	-
2007	e^+	753.3	-	-	112.4	-	-	-	-	-	-
SUM		1921.1	**49.9**	150.2	697.7	192.7	46.8	53.4	85.9	106.8	50.3

Table 4.1: Overview of the integrated luminosity values in pb^{-1} of each data set, with each target gas and lepton beam charge used. The longitudinally polarised hydrogen (H$_\parallel$) data set analysed in this thesis is highlighted in boldface.

impurity. However, it resulted in a decreased luminosity and reaction rate, and had a significantly detrimental effect on the lifetime τ_ℓ of the beam

$$\frac{1}{\tau_\ell} = \frac{1}{\tau_{\mathrm{HERMES}}} + \frac{1}{\tau_{\mathrm{HERA}}}\,, \tag{4.6}$$

where the contribution from the HERMES target, $\tau_{\mathrm{HERMES}} > 45\,\mathrm{hrs}$ [75].

The wide physics scope of the HERMES experiment was aided by the ability to measure lepton-hadron interactions using various target gases with either beam charge. Over the experimental data-taking period of $1996 - 2007$, HERMES operated using unpolarised and polarised (either longitudinal $\parallel$ or transverse $\perp$) gas targets ranging from hydrogen and deuterium to heavy nuclear gases such as krypton and xenon. The gas targets are summarised in chronological order in Table 4.1 which also shows the integrated luminosities of the experimental data.

The Longitudinally Polarised Gas Target

For this thesis, the analysis was performed using positron data taken in 1996 and 1997 on a longitudinally polarised hydrogen $\left(\mathrm{H}_\parallel\right)$ gas target. The HERMES polarised gas
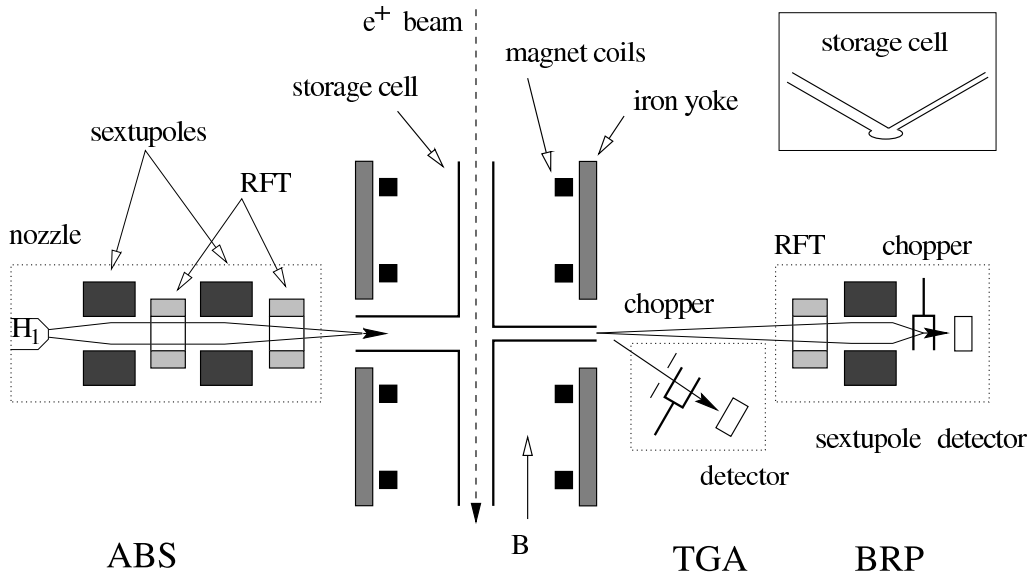
Figure 4.4: Schematic view of the HERMES longitudinally polarised gas target [76]. From left to right: the Atomic Beam Source (ABS), target chamber consisting of the storage cell and magnet, and diagnostic system composed of the Target Gas Analyser (TGA) and the Breit-Rabi Polarimeter (BRP). The locations of the radio-frequency transition (RFT) units are also indicated.

target is detailed in Ref. [77] and schematically shown in Fig. 4.4. It consisted of a Stern-Gerlach Atomic Beam Source (ABS) [78] which supplied a storage cell, internal to the HERA lepton ring, with gaseous atoms of polarised hydrogen. These could diffuse into one of two component systems: the Target Gas Analyser (TGA) [79], used to measure the atomic content of the target gas, or the Breit-Rabi Polarimeter (BRP) [80] which provided measurements of the atomic target polarisation. The target chamber was subject to a $350\,\mathrm{mT}$ magnetic holding field supplied by a superconducting magnet. This is pictured in Fig. 4.5. This magnet defined the axis of polarisation and prevented spin relaxations by decoupling the spins of the target protons and beam positrons. The key features and operation of each of these subcomponents will now be described.

Storage Cell

The target gas storage cell [81] installed in the HERMES experimental setup for the longitudinally polarised proton data-taking period is shown schematically in Fig. 4.6. Several target cells were installed over the course of the HERMES data-taking programme, each optimised for the specific target requirements. This particular storage cell was designed to maintain high target polarisation and target thickness with a density of
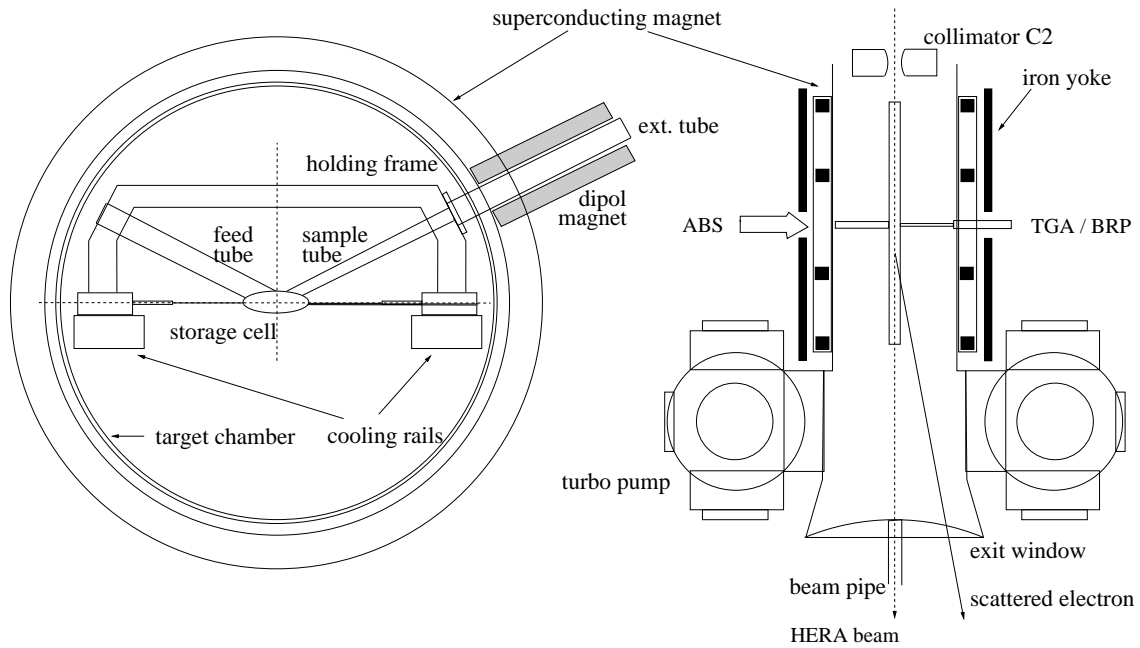
Figure 4.5: Longitudinal target chamber and superconducting magnet viewed from downstream with respect to the HERA beam direction (left), and from above (right) [76].

7×10^{13} nucleons cm^{-2}.

The storage cell was constructed from two $75\,\mu$m-thick and 400 mm long aluminium sheets with an elliptical cross-section of 9.8 mm $\times$ 29 mm. To minimise depolarisation and recombination of the gas molecules arising from collisions with the cell walls, the cell was coated with Drifilm [81] and the hydrogen gas was cryogenically cooled by cooling rails to a temperature of 100 K. These rails were mounted on a target support flange, and their temperature was measured and constantly monitored by three thermistors.

The storage cell was connected to the beam pipe by $100\,\mu$m-thick titanium wakefield suppressors which confined the radio frequency of the HERA beam to form a gradual electrical transition at the discontinuities between the cell and beam pipe. This prevented overheating and damage to the storage cell. Two tubes were connected to the cell: the feed tube, used to inject the polarised hydrogen atoms into the cell, and the sample tube through which approximately 5% of the target gas was sampled and analysed by the TGA and BRP. These tubes were offset by $120°$ to maintain thermal equilibrium between the sampled gas and the storage cell casing.
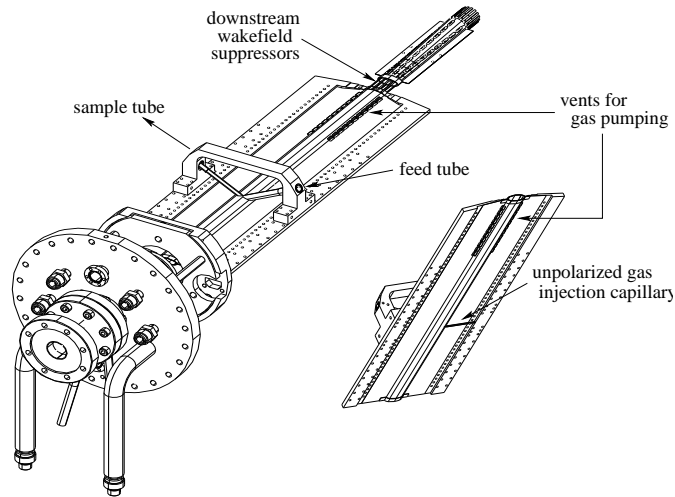
Figure 4.6: Schematic of the target storage cell and its support flange [76]. Also shown are the wakefield suppressors, and the feed and sample tubes described in the text.

Atomic Beam Source (ABS)

The storage cell was populated with polarised, gaseous atoms of hydrogen by the Atomic Beam Source [78]. This was a multi-component system consisting of an atom dissociator, beam forming and pumping systems, and sextupole magnets which were used to focus the atoms into the cell.

As hydrogen gas molecules passed through the dissociator they experienced a 13.56 MHz RF-discharge producing a degree of dissociation of up to 80% [77]. During this process, trace amounts of oxygen were introduced to ensure stability. The dissociated atoms of gas flowed through a collimator, cooled to 100 K, into the pumping system. At this temperature, water produced in the dissociator chamber froze on the collimator nozzle. This helped prevent recombination of the monatomic hydrogen atoms. At 5-day intervals the chamber was heated to remove the layer of ice which had built up, to maintain a constant flow of gas.

These atoms were then pumped into the HERA vacuum region where an array of 1.5 T sextupole magnets separated the hyperfine states of hydrogen with spin projection $m_s = \pm\frac{1}{2}$. These were focussed into the storage cell providing a polarised hydrogen gas sample for data-taking.
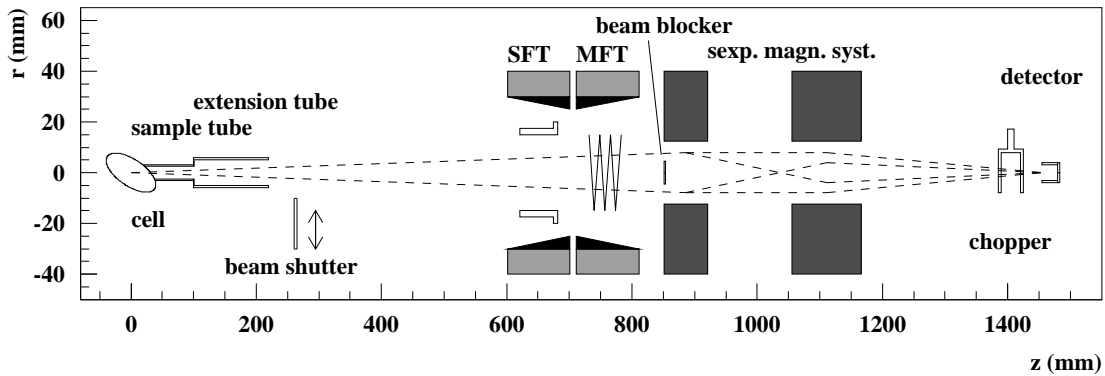
Figure 4.7: Schematic layout of the BRP with respect to the sample tube [76]. The beam blocker at the entrance to the first set of magnets ensured 100% rejection of atoms with hyperfine state $m_{\mathrm{s}} = -\frac{1}{2}$.

Breit-Rabi Polarimeter (BRP)

The Breit-Rabi Polarimeter [80], shown in Fig. 4.7, provided measurements of the relative populations of each hyperfine state from a sample of approximately 5% of the target gas which diffused from the storage cell. These measurements were used to determine the absolute atomic target polarisation which is essential for the analysis presented in this thesis. The BRP was tilted by 30° with respect to the ABS to ensure the atoms had undergone at least one collision with the wall and had not come directly from the injected beam. Two sextupole magnets separated the sampled atoms with hyperfine states $m_{\mathrm{s}} = +\frac{1}{2}$ and $m_{\mathrm{s}} = -\frac{1}{2}$. The former states were focussed towards the BRP and the latter were blocked by a 9 mm diameter beam blocker with a rejection efficiency of 100%. The absolute atomic target polarisation was calculated from the relative population of the $m_{\mathrm{s}} = +\frac{1}{2}$ atoms and accurate measurements of the magnetic field strength of the target magnet. This calculation is detailed in Ref. [77].

The Target Gas Analyser (TGA)

The target gas in the storage cell could also diffuse into the Target Gas Analyser [79] which provided measurements of both the atomic and molecular content of the sample. The TGA arrangement, shown in Fig. 4.8, was offset by 7° with respect to the BRP, allowing gas flow to both analysers. A pair of baffles ensured that only gas from the sample tube was analysed and prevented recombination. The degree of dissociation of the sampled target gas α_{TGA}, defined as the fraction of nucleons in atoms relative to all nucleons entering the
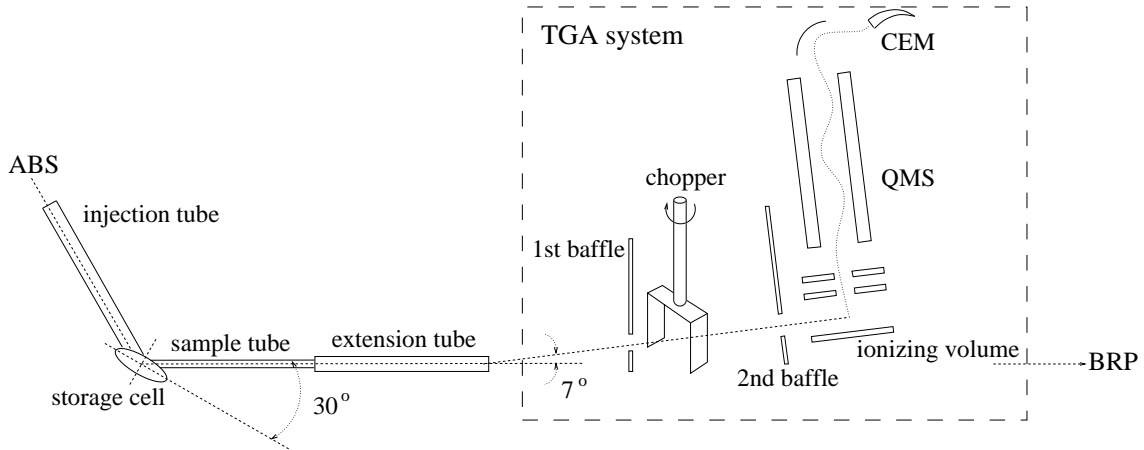
Figure 4.8: A schematic diagram of the Target Gas Analyser [76]. Approximately 5% of the target gas diffused through the extension tube and was collimated by two baffles before entering the ionising volume. The chopper was used for background subtraction.

TGA, is given as

$$\alpha_{\mathrm{TGA}} = \frac{\Phi_{\mathrm{A}}}{\Phi_{\mathrm{A}} + \Phi_{\mathrm{M}}}, \tag{4.7}$$

where Φ_{A} and Φ_{M} are the normalised fluxes of atoms and molecules respectively. Typical α_{TGA} values of up to 80% were observed.

Beam and Target Properties of the 1996 − 1997 Data Set

For the longitudinally polarised proton data set used in this analysis, measurements of the year-averaged beam and target polarisations were taken for each polarisation state. These values are presented in Table 4.2 alongside systematic uncertainties determined by the beam [82] and target [83] groups at HERMES. These values will be used in Chapter 5 in the extraction of the polarisation-dependent asymmetries.

Year	Luminosity	Beam Polarisation		Target Polarisation	
	$\left[\mathrm{pb}^{-1}\right]$	$P_\ell < 0$	$P_\ell > 0$	$P_{\mathrm{L}} < 0$	$P_{\mathrm{L}} > 0$
1996	12.6 ± 1.0	−	0.514 ± 0.017	-0.759 ± 0.042	0.759 ± 0.042
1997	37.3 ± 3.2	-0.531 ± 0.018	0.497 ± 0.017	-0.850 ± 0.032	0.850 ± 0.032

Table 4.2: The integrated luminosities in pb^{-1} of the analysed data sets with average beam and target polarisations for each state.

4.3 The HERMES Spectrometer

The HERMES detector [84] was a forward spectrometer, symmetrical above and below the beam-line, and consisted of several subdetectors for both particle tracking and identification. This is schematically shown in Fig. 4.9. A septum magnet plate, installed in the region of the $1.3\,\mathrm{T}$ magnets shielded the lepton beam from the magnetic field. The acceptance of the HERMES spectrometer was limited at small angles as a consequence of this plate, and at large angles due to the presence of the magnets used to bend charged particle tracks. As a result, only charged particles with scattering angles

$$40\,\mathrm{mrad} < \quad |\theta_{\mathrm{vertical}}| \quad < 140\,\mathrm{mrad}\,,$$
$$|\theta_{\mathrm{horizontal}}| \quad < 170\,\mathrm{mrad}\,,$$

were detected, resulting in a total angular acceptance of

$$40\,\mathrm{mrad} < |\theta| \quad < \quad 220\,\mathrm{mrad}\,.$$

The network of subdetectors used in this analysis were, in increasing position along the beam-line: Drift Chambers (DVCs, FCs and BCs), Magnet Chambers (MCs), a Threshold Čerenkov Detector, trigger hodoscopes, a Transition Radiation Detector (TRD), a preshower and an electromagnetic calorimeter. The purpose of each of these detectors will be described in this section. After the longitudinally polarised hydrogen data-taking period, the Threshold Čerenkov Detector was upgraded to the Ring-Imaging Čerenkov Detector (RICH). For detailed descriptions of the two detectors not covered in this thesis, the Lambda Wheels and the RICH, see Refs. [85] and [86] respectively.

4.4 Particle Identification at HERMES

One of the most important aspects of the analysis presented in this thesis is the identification of the scattered beam positron and produced real photon from an $e\,p \to e\,p\,\gamma$ event. The particle identification (PID) system [88] at HERMES was capable of discriminating between leptons and hadrons with a hadron contamination of less than 1% remaining in the lepton sample. The method utilised information from four subdetector systems: the Threshold Čerenkov Detector, the Transition Radiation Detector (TRD), the electromagnetic calorimeter and the preshower detector.
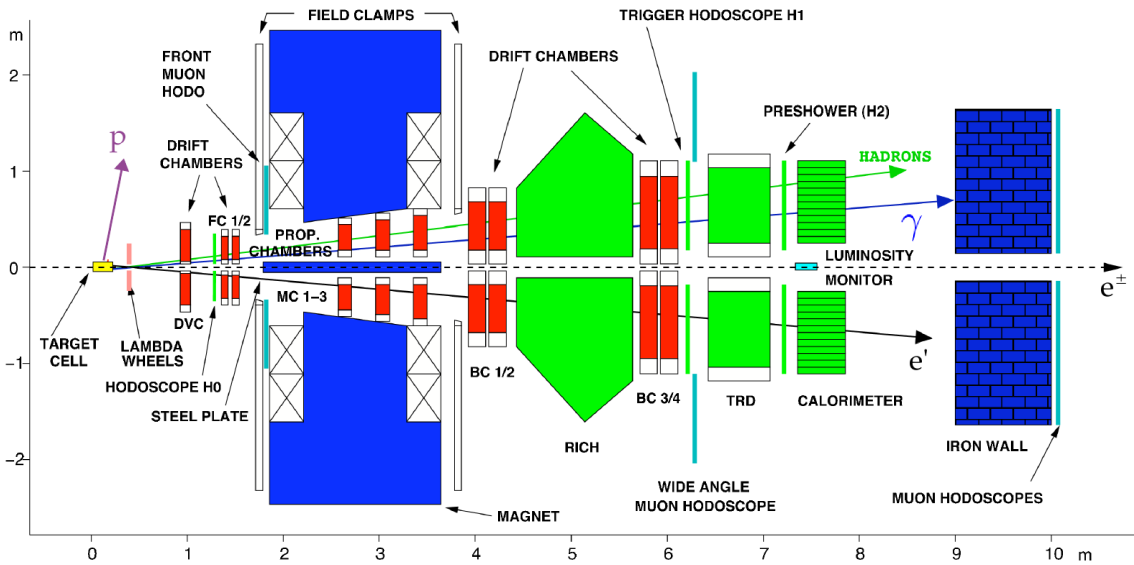
Figure 4.9: Schematic side view of the HERMES forward angle spectrometer after RICH upgrade. The particle identification (PID) detectors are shown in the green (light shaded) regions and the particle tracking detectors are highlighted in red (intermediate shading). The magnets are shown in blue (dark shading). Shown also is a typical BH/DVCS event with the energy deposition of the scattered lepton (e') and produced real photon (γ) measured in the calorimeter. Figure amended from Ref. [87].

The Threshold Čerenkov Detector

The Threshold Čerenkov Detector [89] was installed in the HERMES setup until 1998 when it was upgraded to the RICH. Like the other PID detectors, it was constructed in two halves, one either side of the beam-line. Each half consisted of an aluminium box filled with a nitrogen-freon gas mixture. When a charged hadron or lepton passed through the mixture with a phase velocity v greater than the speed of light in the medium $\frac{c}{n}$, a cone of Čerenkov light was radiated with opening angle $\psi = \cos^{-1}\left(\frac{c/n}{v}\right)$ along the direction of momentum of the incident particle. Here, n is the refractive index of the medium. It is clear that for a cone to be radiated, the criterion $v > \frac{c}{n}$ must be fulfilled. A consequence of this is that only charged particles with small mass will radiate. The produced cone of light was reflected by focussing mirrors, 26 cm wide and mounted at 23° to the vertical, into an array of photomultiplier tubes which measured the corresponding photoelectron yield N_{pe}. This is written as

$$N_{\mathrm{pe}} = C_0 \left(1 - \frac{1}{(n\beta)^2}\right), \tag{4.8}$$
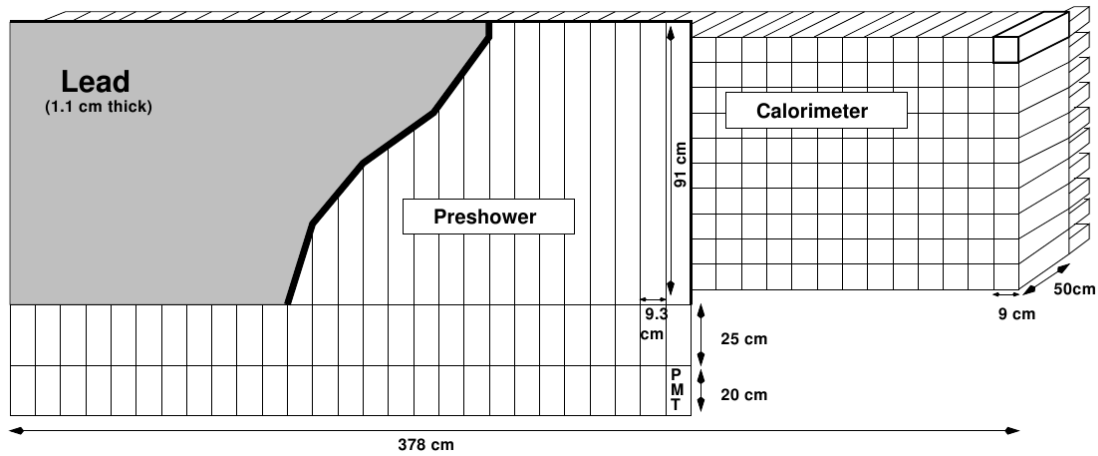
Figure 4.10: Schematic representation, looking downstream, of the preshower and electromagnetic calorimeter [91] on one side of the beam-line. Shown from front to back are the 1.1ċm thick lead plate from which electromagnetic showers originate, some of the 42 scintillator bars comprising the preshower and a 42×10 array of lead glass calorimeter blocks.

where $\beta = \frac{v}{c}$ and C_0 is a constant extracted from data. This allowed the separation of low mass particles from their different momenta.

Transition Radiation Detector (TRD)

The TRD consisted of six modules, above and below the beam-line. Each module contained a 6.35 cm thick radiator and a Multi-Wire Proportional Chamber [90] (MWPC) with 256 wires separated by 1.27 cm. This was filled with a Xe/CH_4 gas mixture optimised for the absorption of transition radiation.

The emission of transition radiation occurs when a charged particle crosses the boundary between two materials with different dielectric constants. At HERMES energies this production of radiation arose solely from leptons [84]. This radiation was emitted with mean energy proportional to γ at an angle $\frac{1}{\gamma}$. Hence at HERMES energies ($\gamma_{\mathrm{lepton}} > 10^4$) there was colinearity between the lepton and transition radiation X-rays. While hadrons do not produce transition radiation, they deposit energy via ionisation. Thus leptons could be discriminated from hadrons from the additional energy deposition arising from transition radiation.

The Electromagnetic Calorimeter and Preshower

The electromagnetic calorimeter [92] shown in Fig. 4.10 discerned between leptons and hadrons by comparing the ratio between their energy deposition and momenta *i.e.* E/p

where p was predetermined from the HERMES tracking procedure (see Section 4.5). The thickness of the calorimeter was sufficient to fully contain an electromagnetic shower produced by a charged lepton. For such an interaction, $E/p \simeq 1$ *i.e.* almost all the lepton energy was deposited. For a hadronic shower, the mean free path between collisions was typically an order of magnitude larger than for leptons, such that they could not be contained within the calorimeter. Hence only a fraction of the hadron energy was deposited, *i.e.* $E/p < 1$. Figure 4.11 shows a comparison between the normalised calorimeter response for hadrons and leptons. This shows the high degree of separation between both sets of particles.

The calorimeter itself was situated $729\,\mathrm{cm}$ along the beam-line from the centre of the target cell. It was comprised of 840 lead-glass blocks with cross-sectional dimensions $9\,\mathrm{cm} \times 9\,\mathrm{cm}$ and each $50\,\mathrm{cm}$ long. These were arranged in two 42×10 arrays, one either side of the beam-line. Studies detailed in Ref. [92] showed that the calorimeter was able to resolve the spatial position of the lepton to within $1\,\mathrm{cm}$. The calorimeter is also used in DVCS analyses to provide rough spatial and energy information for the produced real photon. However this energy measurement suffers from poor resolution, of approximately 5%, determined by

$$\frac{\sigma(E_\gamma)}{E_\gamma}\,\% = \frac{5.1 \pm 1.1}{\sqrt{E_\gamma}} + (2.0 \pm 0.5) + \frac{10.0 \pm 2.0}{E_\gamma}\,, \tag{4.9}$$

where E_γ is the measured photon energy in GeV.

The electromagnetic calorimeter was complemented by a preshower hodoscope which consisted of a $1.1\,\mathrm{cm}$ thick lead plate from which the electromagnetic showers originate. In addition, a series of 84 scintillator bars, sometimes referred to as the H2 hodoscope, were divided evenly above and below the beam-line. From its energy deposition spectrum, the preshower was able to provide further information to help to distinguish between hadrons and leptons.

4.5 Particle Tracking at HERMES

It was important to not only identify, but to track the scattered beam lepton through the entire region of the spectrometer with detection in both the 'front' and 'back' regions. This was vital in identifying the process that had taken place and also for determining the four-momenta and positional information necessary to calculate the kinematics of the interaction. The front region of the spectrometer contained a series of horizontal drift
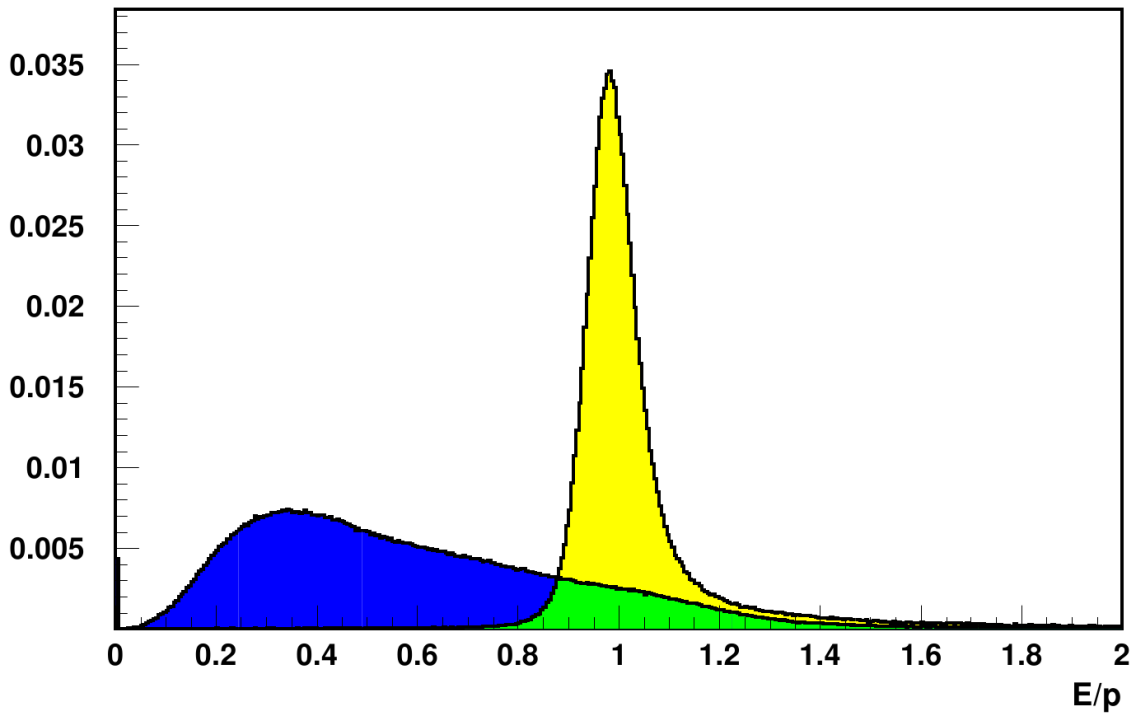
Figure 4.11: The normalised response of the electromagnetic calorimeter, showing the difference in E/p ratios between hadrons (dark blue) and leptons (light yellow). Figure taken from Ref. [91].

chambers, the Drift-Vertex Chamber (DVC) and two Front Chambers (FC 1/2). The back region contained four Back Chambers (BC 1/2 and 3/4). In the region of the bending magnet there was also a series of Magnet Chambers (MC 1-3). These are all shown in Fig. 4.9 and the operating principles are outlined here. For a detailed description of the construction and individual readout systems, see Ref. [84].

Magnet Chambers

The Magnet Chambers (MCs) in the HERMES spectrometer were examples of MWPCs. These consisted of three submodules, each with a plane of alternating anode and cathode wires between a pair of cathode foils. This arrangement was surrounded by a gas mixture comprising of Ar (65%), CO_2 (30%), and CF_4 (5%). Two of these submodules were orientated at angles of $\pm 30°$ with respect to the x-plane allowing spatial determination in the x, u ($-30°$) and v ($+30°$) planes. As a charged particle passed through the MWPC, the gas mixture ionised and the produced electrons experienced acceleration in the internal electric field. This induced further ionisation by a phenomenon known as the Townsend Avalanche in which the measured current is proportional to the energy of the incident charged particle. The primary function of the MCs was the momentum determination of

low-momenta tracks and was also used to resolve multiple particle tracks [93].

Drift Chambers

The operation of the drift chambers was similar to that of the MCs but with a smaller internal electric field below the ionisation threshold. A different gas mixture of $Ar\,(90\%)$, $CO_2\,(5\%)$, and $CF_4\,(5\%)$ was used. They consisted of six layers of drift cells, each with a plane of cathode and anode wires similar to the MCs. The drift time across the cell was used to determine the intersection of the charged lepton with the chamber.

The DVC, with a drift cell size of $6\,mm$, was installed in 1997 to provide a larger acceptance of $\pm[35,270]\,mrad$ in the vertical plane and $\pm200\,mrad$ in the horizontal plane with spatial resolution of $220\,\mu m$. The FCs and BCs were similar in construction and operation to the DVC but with drift cell sizes of $7\,mm$ and $15\,mm$ respectively. The FCs, situated upstream of the spectrometer magnet, consisted of one module with six planes, providing good spatial resolution, typically $225\,\mu m$, and an efficiency greater than 96%. The performance of the BC pairs (BC1/2 and BC3/4) were monitored throughout the 1996 running and were shown to provide an optimum spatial resolution of $275\,\mu m$ with a tracking efficiency in excess of 99% [94].

4.6   Trigger and Reconstruction Software

In the analysis detailed in this thesis, a BH/DVCS event candidate is selected only if exactly one charged track identified as a DIS lepton was tracked through the spectrometer and a single real photon was detected in the calorimeter. In addition, a host of data quality, kinematic and geometric criteria must be satisfied. The DIS-event trigger system and the separate track and photon reconstruction methods will now be outlined.

DIS Event Trigger

When a candidate physics event was identified, the trigger system activated the readout of all detectors. At HERMES there were many triggers relating to specific analyses. For the purposes of this analysis the DIS-event trigger (trigger-21) was used. This required coincidences in the front (H0) and back region (H1) hodoscopes, a signal in the preshower (H2) larger than the minimum ionisation energy of the lepton, and signals greater than $1.4\,GeV$ must have registered in two neighbouring calorimeter blocks to ensure good separation

between hadrons and leptons (see Fig. 4.11). All these must be detected in coincidence with the bunch timing signal provided by the HERA clock.

Track Reconstruction Software

The HERMES Reconstruction Code (HRC), described in detail in Ref. [95], reconstructs front and back partial tracks using information provided by the various tracking detectors of the spectrometer. The momentum of the scattered lepton can be extracted from a look-up table and used along with information from the PID detectors to provide not only particle type, but also positional information which are crucial to the analysis outlined in Chapter 5.

Photon Reconstruction Software

Photons are detected in the calorimeter as a neutral signal 'cluster' with no corresponding track in the spectrometer. As DVCS was not included in the initial physics programme of the HERMES experiment, the design specifications of the spectrometer and calorimeter did not allow for accurate measurements of energy deposition from photons. The energy resolution of the detected photons are therefore poorer that those for charged leptons. In Chapter 5, steps to alleviate this problem are outlined with the introduction of a constraint on the calculation of the Mandelstam t variable used throughout this analysis.

Chapter 5

Exclusive Leptoproduction of Real Photons on a Longitudinally Polarised Hydrogen Target

Recently, HERMES has published results associated with DVCS on a variety of gaseous targets [22–25]. These analyses, collectively using the $1996 - 2005$ HERMES data set prior to the installation of the Recoil Detector [96], follow the analytical procedure devised for the DVCS analysis of the transversely polarised hydrogen data set [22], *i.e.* the simultaneous extraction of a number of azimuthal asymmetries using the maximum likelihood fitting formalism [97, 98].

This chapter will outline this analytical procedure tuned for the simultaneous extraction of three azimuthal asymmetries $\mathcal{A}_{\mathrm{UL}}$, $\mathcal{A}_{\mathrm{LL}}$ and $\mathcal{A}_{\mathrm{LU}}$ in the distribution of real photons from BH and DVCS off a longitudinally polarised hydrogen gas target using a longitudinally polarised positron beam. These asymmetries, introduced previously in Eqs. 3.16, 3.22 and 3.28 respectively, are dependent on the longitudinal polarisations of the beam and/or target. The assignment of systematic uncertainties will be described in Chapter 6. The final results are discussed and presented in Chapter 7 alongside theoretical predictions from the GPD model in Ref. [49].

The results from this extraction of $\mathcal{A}_{\mathrm{UL}}$ and $\mathcal{A}_{\mathrm{LL}}$ are presented in the recent HERMES publication of Ref. [99].
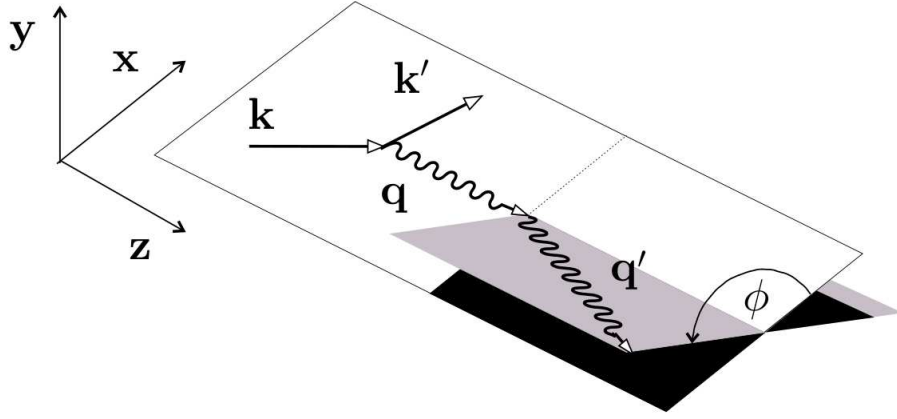
Figure 5.1: Definition of the azimuthal angle ϕ between the lepton-scattering and photoproduction planes. Also highlighted are the four-momenta of the incoming lepton $\mathbf{k}$, scattered lepton $\mathbf{k}'$, virtual photon $\mathbf{q}$ and real photon $\mathbf{q}'$. Not shown are the four-momenta $\mathbf{p}$ and $\mathbf{p}'$ of the target and recoiling nucleon respectively. Figure taken from Ref. [100].

5.1 Kinematic Definitions

For the purposes of this thesis, the analysed process involves the quasi-elastic scattering of a positron from the HERA beam on a longitudinally polarised hydrogen target with a produced real photon and scattered positron detected in the final state. The interaction with a quark in the target proton is mediated by virtual photon exchange. The scattered positron was tracked through the HERMES spectrometer and identified as a single charged track. The produced real photon was detected as a trackless cluster in the calorimeter and the recoiling proton was not detected. This process is illustrated in Fig. 5.1 where the related four-momenta are given as

$$ e(\mathbf{k})\,p(\mathbf{p}) \overset{\gamma^*(\mathbf{q})}{\to} e(\mathbf{k}')\,p(\mathbf{p}')\,\gamma(\mathbf{q}')\,. \tag{5.1} $$

These are defined using the standard four-momentum $\mathbf{v} = (E,\,\vec{v})$ and corresponding positional three-vector $\vec{v} = (v_x,\,v_y,\,v_z)$ notation as

- $\mathbf{p} = (M_p,\,0,\,0,\,0)$, the four-momentum of the target proton at rest. Fermi momentum is neglected here in the quasi-elastic scattering case. The rest energy is therefore taken as the proton rest mass, M_p.

- $\mathbf{k} = (E_\ell,\,0,\,0,\,P_\ell)$ is the four-momentum of the beam positron. The direction of momentum is assumed to be purely in the z-direction.

- $\mathbf{q}$ is the four-momentum of the virtual photon which is calculable from the measured

$\mathbf{k}'$ and $\mathbf{q}'$. It is calculated as

$$\mathbf{q} = \left(\nu, \ -|P_{\text{track}}| \sin \theta_\ell \cos \phi_\ell, \ -|P_{\text{track}}| \sin \theta_\ell \sin \phi_\ell, \ (P_\ell - |P_{\text{track}}| \cos \theta_\ell) \right),$$

where P_{track} is the momentum of the detected positron track, θ_ℓ is the polar angle between the incoming and scattered positrons in the scattering plane, and ϕ_ℓ is the azimuthal scattering angle of the positron.

- $\mathbf{p}'$ is the four-momentum of the recoiling proton. This cannot be measured in this analysis.

- $\mathbf{k}'$ is the four-momenta of the scattered positron which is detected in the calorimeter and calculated as

$$\mathbf{k}' = \left(E_{\text{track}}, \ |P_{\text{track}}| \sin \theta_\ell \cos \phi_\ell, \ |P_{\text{track}}| \sin \theta_\ell \sin \phi_\ell, \ |P_{\text{track}}| \cos \theta_\ell \right).$$

- $\mathbf{q}'$ is the four-momentum of the produced real photon, also detected by the calorimeter at corresponding positional three-vector $\vec{q'}$, and is given as

$$\mathbf{q}' = \left(E_\gamma, \ \frac{E_\gamma \vec{q'}}{\left| \vec{q'} \right|} \right).$$

In Chapter 2, kinematic variables pertaining to DIS were introduced. Here they are summarised with the corresponding data selection criteria discussed in Section 5.2.

The angle ϕ, shown in Fig. 5.1, is defined as the azimuthal angle between the lepton-scattering plane and the plane containing the vectors of the virtual and real photons. This is calculated from the three-vectors of the incoming positron and the real and virtual photons as

$$\phi = \frac{\vec{q} \times \vec{k} \cdot \vec{q'}}{\left| \vec{q} \times \vec{k} \cdot \vec{q'} \right|} \cos^{-1} \left(\frac{\vec{q} \times \vec{k}}{\left| \vec{q} \times \vec{k} \right|} \cdot \frac{\vec{q} \times \vec{q'}}{\left| \vec{q} \times \vec{q'} \right|} \right). \tag{5.2}$$

At HERMES, results from the extraction of azimuthal asymmetries relating to the BH and DVCS processes are presented in bins of three kinematic variables: Q^2, x_{B}, and t. The negative squared four-momentum Q^2 of the virtual photon is calculated from the four-momenta of the initial and scattered leptons as

$$Q^2 \equiv -\mathbf{q}^2 \equiv -(\mathbf{k} - \mathbf{k}')^2 \overset{\text{lab}}{=} 4 \, E \, E' \sin^2 \left(\frac{\theta_\ell}{2} \right). \tag{5.3}$$

The Bjorken scaling variable x_{B} is defined as

$$x_{\text{B}} \equiv \frac{Q^2}{2 \, (\mathbf{p} \cdot \mathbf{q})} \overset{\text{lab}}{=} \frac{Q^2}{2 \, M_p \, \nu}. \tag{5.4}$$

The third binning variable is the squared four-momentum transfer to the nucleon. In a change to the notation from Ref. [27], this is represented by the Mandelstam t variable instead of Δ^2 and can be determined via the difference in four-momenta of the initial and final state nucleons or photons as

$$t \equiv (\mathbf{p} - \mathbf{p}')^2 \equiv (\mathbf{q} - \mathbf{q}')^2 \,. \tag{5.5}$$

In the lab frame frame this can be calculated as

$$t \stackrel{\text{lab}}{=} -Q^2 - 2E_\gamma \left(\nu - \sqrt{\nu^2 + Q^2} \cos \theta_{\gamma^* \gamma} \right) \,, \tag{5.6}$$

where E_γ is the energy deposited in the electromagnetic calorimeter by the real photon, a measurement which is subject to a comparatively large uncertainty, and $\theta_{\gamma^* \gamma}$ is the polar angle between the three-vectors of the virtual and real photons, calculated as

$$\theta_{\gamma^* \gamma} = \cos^{-1} \left(\frac{\vec{q} \cdot \vec{q'}}{|\vec{q}||\vec{q'}|} \right) \,. \tag{5.7}$$

As the recoiling proton was not detected, the 'exclusive' event sample is selected using the squared 'missing-mass' M_X^2 of the $e \, p \to e \, \gamma \, X$ interaction which is calculated using E_γ as

$$M_\text{X}^2 \equiv \left(\mathbf{k} - \mathbf{k}' + \mathbf{p} - \mathbf{q}' \right)^2 \stackrel{\text{lab}}{=} M_p^2 + 2M_p(\nu - E_\gamma) + t \,. \tag{5.8}$$

The low resolution ($\sim 5\%$) in the energy measurement of the produced photon in the calorimeter results in the calculated value of M_X^2 for high-energy photons extending to negative values. As the measurement of E_γ is subject to large uncertainty, the resolution in t is consequently affected. However, assuming an exclusive sample where $M_\text{X} = M_p$ for elastic events which leave the proton intact, Eq. 5.8 can be rearranged as

$$E_\gamma = \frac{t}{2M_p} + \nu \,. \tag{5.9}$$

This can be substituted into Eq. 5.6, providing a calculation of t which is 'constrained' for exclusive events. This quantity t_c no longer depends on the measured photon energy and instead relies on its interaction position in the calorimeter which can be measured with greater precision. This is calculated as

$$t_c \stackrel{\text{lab}}{=} \frac{-Q^2 - 2\nu \left(\nu - \sqrt{\nu^2 + Q^2} \cos \theta_{\gamma^* \gamma} \right)}{1 + \dfrac{1}{M_p} \left(\nu - \sqrt{\nu^2 + Q^2} \cos \theta_{\gamma^* \gamma} \right)} \,. \tag{5.10}$$

For the remainder of this thesis, this calculation of t will be used, *i.e.* $t = t_c$.

Other experiments such as CLAS [101] prefer to present the dependence of their asymmetry amplitudes on the skewness parameter ξ. This is interpreted as the average longitudinal momentum fraction transferred to the nucleon during the scattering process and is expressed as

$$\xi \simeq \frac{x_{\mathrm{B}} \left(1 + \frac{t}{2Q^2} \right)}{2 - x_{\mathrm{B}} + x_{\mathrm{B}} \frac{t}{Q^2}} \overset{Q^2 \gg t}{\simeq} \frac{x_{\mathrm{B}}}{2 - x_{\mathrm{B}}} \,, \tag{5.11}$$

using the convention from Ref. [27]. The use of this non-standard kinematic variable at HERMES is disfavoured over the well-defined Bjorken scaling variable.

The final kinematic definition required is the invariant mass W of the $\gamma^* p$ system which is widely used as one of the key selection criteria of a DIS-candidate event. The squared invariant mass W^2 is given by

$$W^2 \equiv (\mathbf{p} + \mathbf{q})^2 \overset{\mathrm{lab}}{=} M_p^2 + 2M_p \nu - Q^2 \,. \tag{5.12}$$

5.2 Selection of the Exclusive Event Sample

The HERMES data structure is illustrated in Fig. 5.2. For each year of data-taking, several data productions were iteratively created based on improvements in detector calibration, particle tracking and/or data quality software. Each production is divided into data runs lasting approximately 30 minutes, containing 10 second 'bursts' of data during which the performance and quality of the beam, target and detectors are continuously monitored. These bursts contain individual physics events.

Burst-Level Data Quality Criteria

Several burst-level data quality requirements are applied to the experimental data to ensure analysed bursts are not subject to detrimental factors. These are presented as a hexadecimal 32-bit 'pattern' which can be tuned to a specific physics analysis to ensure the quality of the analysed data sample. For the data productions used in this analysis, 96d0 and 97d1, the required bits and their purposes are:

- **Bit 2**: Rejects bursts with an unphysical and/or unreasonably high dead time.

- **Bit 3**: Ensures the length of the burst $L_{\mathrm{burst}} < 11 \, \mathrm{ns}$.

- **Bit 4**: Only allows bursts with a beam current I_ℓ in the range $5 \, \mathrm{mA}$ to $50 \, \mathrm{mA}$.
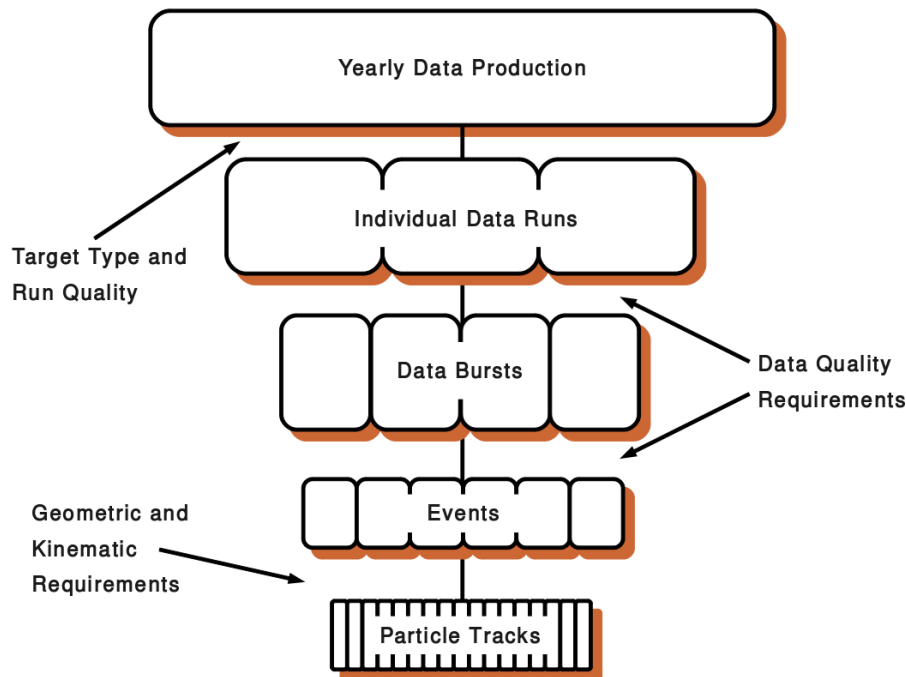
Figure 5.2: Illustration of the HERMES data structure, highlighting the different levels at which different criteria are applied to select the analysed data sample.

- **Bit 5**: This bit discards data with very small count rates and/or very large fluctuations in target density.

- **Bit 6**: Checks that the burst was not the first in an experimental run.

- **Bit 7**: All bursts with 'bad' data records or last bursts in a target fill period are discarded.

- **Bit 8**: Any burst with no PID information available are rejected.

- **Bit 9**: The burst must be part of a run manually marked 'analysable' in the HERMES electronic logbook.

- **Bit 16**: This bit is used to reject bad target data.

- **Bit 17**: Discards any burst in which at least one calorimeter block was 'dead'.

- **Bit 18**: The burst is discarded if at least one block in the H2 hodoscope and/or the luminosity monitor was dead.

- **Bit 19**: Ensures the TRD was fully operational.

- **Bit 20**: Checks there were no high voltage trips in the FCs or BCs.

- **Bit 22**: Checks the performance of the calorimeter to ensure the threshold voltage was stable.

- **Bit 28**: Rejects the burst if the most recent beam polarisation measurement was taken more than 5 minutes ago.

- **Bit 30**: Polarised target data not undergoing a dead-time correction are discarded.

This corresponds to a bit pattern of 0x505F03DC. In addition to using this bit pattern, the following data quality criteria are applied to the data. These are expressed using the appropriate HERMES ADAMO [102] data table variables in the format **table.variable**.

- $0.0 < |$**g1Beam.rPolFit**$| < 1.0$ restricts the beam polarisation to realistic values which can be measured by the polarimeters.

- **g1Quality.iTrdDQ** $= 3$ allows only those bursts for which the TRD was fully operational in both spectrometer halves. This is a complementary requirement to Bit 19.

- $5 <$ **g1Beam.rLumiRate** < 10000 ensures that the measured luminosity rate was reasonable.

- $0.8 <$ **g1DAQ.rDeadCorr21** ≤ 1.0 requires the data acquisition (DAQ) software to have been active for more than 80% of the burst.

- **g1DAQ.bProdMethods** $\& \, 0x00800 \, ! = 0x00800$ rejects the burst if neither beam polarimeter was operational.

Integrated Luminosity

The results presented in this thesis are normalised to the time-integrated luminosity L of each beam helicity and target polarisation state. This is expressed as

$$L = \int \mathcal{L}(\tau)\, \mathrm{d}\tau = \int \frac{I_\ell(\tau)\rho}{e}\, \mathrm{d}\tau\,, \tag{5.13}$$

where $\mathcal{L}$ represents the time-dependent luminosity, ρ denotes the target density and e is the elementary charge of the lepton. Throughout this data-taking period the target density was monitored and found to be stable [77].

The luminosity monitor, introduced in Section 4.1, calculated the integrated luminosity from measurements of the coincidence rate $R_{\mathrm{LUMI}} = \sigma_{\mathrm{BM}} \mathcal{L}$ and cross-section, σ_{BM} of the

Bhabha and Møller scattering processes. The resultant time-integrated luminosity of each burst is given as

$$L = \epsilon_{\text{eff}} \, C_{\text{LUMI}} \, \frac{A}{Z} \int R_{\text{LUMI}}(\tau) \, \mathrm{d}\tau \,, \tag{5.14}$$

for a given target nucleus with A nucleons and Z protons. Here, ϵ_{eff} is the efficiency of the detector which accounts for dead-time effects.

The stability of the target density over the longitudinally polarised proton data-taking period allows the use of a target-state averaged fit to the values of R_{LUMI} such that a target-polarisation independent luminosity can be calculated as

$$L = \epsilon_{\text{eff}} \, C_{\text{LUMI}} \, R_{\text{LUMI}}^{\text{fit}} \, \tau_{\text{burst}} \,, \tag{5.15}$$

for a burst of length τ_{burst}. This is determined from the HERMES data tables as

$$L = \mathbf{g1DAQ.rDeadCorr21} * \mathbf{g1Beam.rLumiFitBstGai} * \mathbf{g1DAQ.rLength} \,.$$

Previous HERMES measurements on unpolarised target data introduced in Section 3.4 used the DIS yield N_{DIS} for data normalisation which is proportional to the luminosity. However, for a longitudinally polarised target the relation between N_{DIS} and L is no longer constant due to contributions from the target polarisation dependent DIS asymmetry $\mathcal{A}_{\parallel}$. As a result a normalisation must be performed using integrated luminosity.

Event-Level Geometric Requirements

In addition to the burst-level selection criteria applied to the experimental data, several geometrical requirements are imposed on the particle track to neglect those that experience internal deflections from subdetectors or shielding plates, and those that are detected in, or originate from, non-feasible regions. Each event must contain a track satisfying the following criteria in order to minimise these effects:

- $|\mathbf{g1Track.rVertZ}| < 18 \, \text{cm}$ ensures that the tracked particle originated from within the region of the target storage cell.

- $\mathbf{g1Track.rVertD} < 0.75 \, \text{cm}$ places a limit on the closest radial distance from the track to the vertex. This has the effect of limiting the background from potential interactions with material occurring outside of the target cell.

- $|x_{\text{lepton}}| < 175 \, \text{cm}$ and $30 \, \text{cm} < |y_{\text{lepton}}| < 108 \, \text{cm}$ constrain the region in the x-y plane where the track energy deposition was measured. This corresponds to the fiducial volume of the calorimeter.

- $5\,\mathrm{mrad} < \theta_{\gamma^*\gamma} < 45\,\mathrm{mrad}$ constrains the polar angle between the virtual and produced photons. The lower limit is imposed to ensure the azimuthal angle ϕ remains well defined within the finite resolution of the spectrometer. Monte Carlo (MC) studies outlined in Ref. [59] show that above this upper limit the data sample is dominated by background processes. See Section 6.2 for a discussion of the most significant sources of background.

The last set of geometric requirements use information from the measured slopes and spatial offsets of the track to ensure that it was not deflected by the septum magnet plates which were situated in possible track trajectories in the spectrometer. These are

- $|x_{\mathrm{offset}} + 172.0^*\tan(\theta_x)| < 31$,

  $|y_{\mathrm{offset}} + 181.0^*\tan(\theta_y)| > 7$,

  $|y_{\mathrm{offset}} + 383.0^*\tan(\theta_y)| < 54$,

  $|\mathbf{smTrack.rXpos} + 108.0^*\mathbf{smTrack.rXslope}| \leq 100.0$,

  $|\mathbf{smTrack.rYpos} + 108.0^*\mathbf{smTrack.rYslope}| \leq 54.0$.

DIS Event and Kinematic Requirements

The HERMES experiment was initially commissioned to investigate many properties relating to DIS. Hence the selection criteria of such an event has been thoroughly investigated. A DIS event ($e\,p \rightarrow e\,X$) is selected by requiring exactly one charged lepton which was fully tracked through the forward spectrometer, and identified as a positron. This is fulfilled using the PID requirement

$$2 < (\mathbf{g1Track.rPID2} + \mathbf{g1Track.rPID5}) < 100,$$

which combines information from the PID detectors introduced in Section 4.4.

This track must also meet the following criteria:

- $\mathbf{smTrack.bTrigMask} \,\&\, (1{<}{<}20)$ checks that trigger-21 fired.

- $27.0\,\mathrm{GeV} < \mathbf{g1Beam.rHeraElEnergy} \leq E_\ell$ ensures that only events with reasonable beam energies are analysed.

- $Q^2 > 1.0\,\mathrm{GeV}^2$ selects events in the DIS region and ensures the factorisation of the DVCS process.

- $W^2 > 9.0 \, \text{GeV}^2$ restricts the kinematic regime to one in which the fragmentation model in the MC is believed to work. This provides a reliable estimation of the fractional contributions from background processes.

- $\nu < 22.0 \, \text{GeV}$ cuts away events with an unreliable efficiency of the photon energy measurement in the calorimeter.

In addition to the detection of one positively-charged lepton track, the detection of exactly one photon is required in the calorimeter. This is achieved by measuring a single signal cluster subject to the following criteria:

- $E_\gamma > 5 \, \text{GeV}$ reduces contamination from background processes.

- $E_{\text{preshower}} > 1 \, \text{MeV}$ ensures that the energy of the produced real photon is sufficiently higher than the threshold energy required to produce an electromagnetic shower in the calorimeter. This requirement rejects approximately 20% of events from the analysed sample and improves the resolution of the E_γ measurement.

- $|x_\gamma| < 125 \text{cm}$ and $33 \, \text{cm} < |y_\gamma| < 105 \text{cm}$. These spatial requirements ensure the photon was detected within the fiducial volume of the calorimeter and hence the energy deposition was correctly reconstructed.

BH/DVCS-Candidate Event Requirements

For each $e \, p \rightarrow e \, \gamma \, X$ event the following criteria are applied to obtain the final analysed data sample:

- $Q^2 < 10.0 \, \text{GeV}^2$ and $0.03 < x_{\text{B}} < 0.35$ are used to define a kinematic region for the two binning variables. These reject a negligible amount of candidate events.

- $-t < 0.7 \, \text{GeV}^2$ is required to reject background events. Monte Carlo studies in Ref. [59] have shown these contributions to increase with $-t$. This will be explained in Section 6.2.

Throughout this chapter, the phrase 'Single Photon Event' (SPE) will refer to events which have passed all the previously outlined requirements.

As the recoiling proton could not be detected, the exclusive sample is selected by constraining the values of M_{X}^2. This 'exclusive region' is consistent with the proton mass as determined from MC simulations in Ref. [65]. The lower limit of this region, defined for the

$2002 - 2005$ data set as $-2.25\,\mathrm{GeV}^2 \leq M_X^2 \leq 2.89\,\mathrm{GeV}^2$, corresponds to a displacement of three times the M_X^2 resolution from the mean of the distribution. The upper limit is chosen such that the contributions from the desired BH/DVCS and background processes are equal.

The RICH detector was installed upstream, in front of the calorimeter in the HERMES spectrometer configuration after the longitudinally polarised proton data-taking period. This additional material reduced the momentum resolution of the detected photon which is subsequently propagated to the calculation of M_X^2. Thus the exclusive region for the pre-RICH data set used in this analysis is expected to be narrower than the post-RICH region determined from MC studies. In Ref. [63], the resultant M_X^2 region for the $1996 - 1997$ positron beam data set was determined to be $-2.08\,\mathrm{GeV}^2 \leq M_X^2 \leq 2.81\,\mathrm{GeV}^2$. However, a year-dependent shift in the mean of the M_X^2 distributions between the constituent data years has since been discovered. This issue will be addressed in Section 6.1.

Visualising the Data

Of the three asymmetries which are simultaneously extracted in this analysis, $\mathcal{A}_{\mathrm{UL}}$ ($\mathcal{A}_{\mathrm{LU}}$) is dependent of the target (beam) polarisation averaged over all beam helicity (target polarisation) states, and the double-spin asymmetry $\mathcal{A}_{\mathrm{LL}}$ is dependent on the product of the polarisations of the beam and target. As such, it is important that the net polarisations of the beam and target are approximately zero over the analysed data set in order to reduce uncertainties in the extraction of the $\mathcal{A}_{\mathrm{UL}}$ and $\mathcal{A}_{\mathrm{LU}}$ respectively.

To ensure this, designated run periods were taken for each beam-helicity state and the direction of polarisation of the target was flipped every $60\,\mathrm{seconds}$. The net target polarisation averaged over the data set is consistent with zero. This is shown in Fig. 5.3 for all data passing the aforementioned burst-level data quality requirements. The yields of exclusive events from the experimental data and a MC simulation [103] are compared in Figs. 5.4 and 5.5 for various kinematic variables. This MC simulation provides estimations of the fractional contributions from the BH/DVCS process and the main sources of background i.e. resonance production and semi-inclusive DIS. The contribution from the exclusive π^0 background is neglected here (see Section 6.2).

It is observed that the data and MC simulation agree well at the exclusive event level. In the exclusive region of the M_X^2 distribution, the MC overshoots the data by about 7%. This can be explained by the lack of radiative corrections in the simulation which results
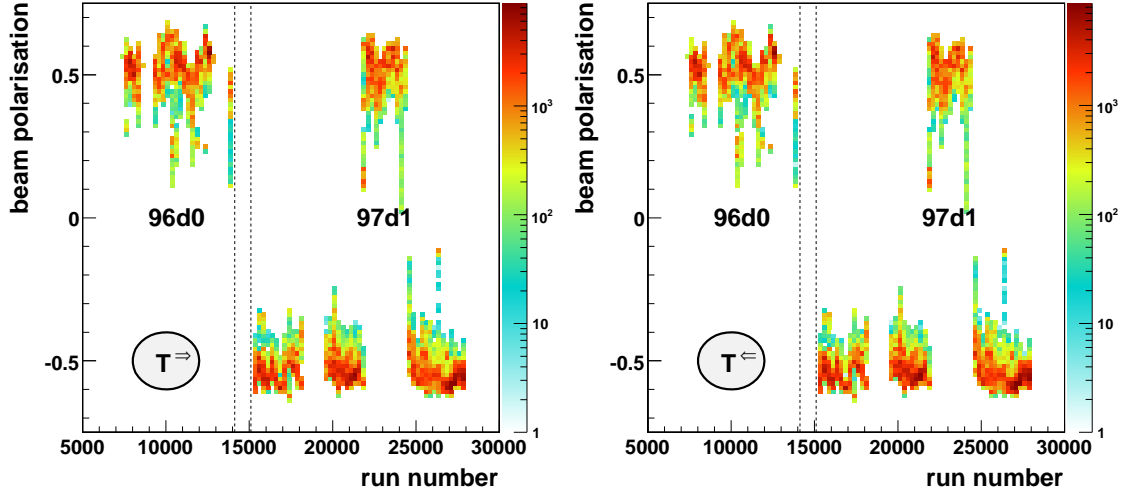
Figure 5.3: The average positron beam polarisation of each analysed burst as a function of run number. Shown here is a comparison for each target polarisation, polarised parallel (left figure) and anti-parallel (right figure) to the beam direction. There are negligible differences between the two target states as a result of the rapid flipping of the polarisation direction.

in the measurement of larger photon energies that shift into the semi-inclusive region [63]. Figure 5.5 also shows the x-y plane spatial distribution of the energy deposition in the calorimeter from the scattered positrons and real photons at SPE-level. For the majority of events, either one of the two particles was detected close to the septum plate surrounding the beam-line.

From the definitions of x_B (Eq. 5.4), t (Eq. 5.10) and ξ (Eq. 5.11) it is shown that they are highly correlated with Q^2, $\theta_{\gamma^*\gamma}$, and x_B respectively. These correlations are presented in Fig. 5.6 at SPE-level.
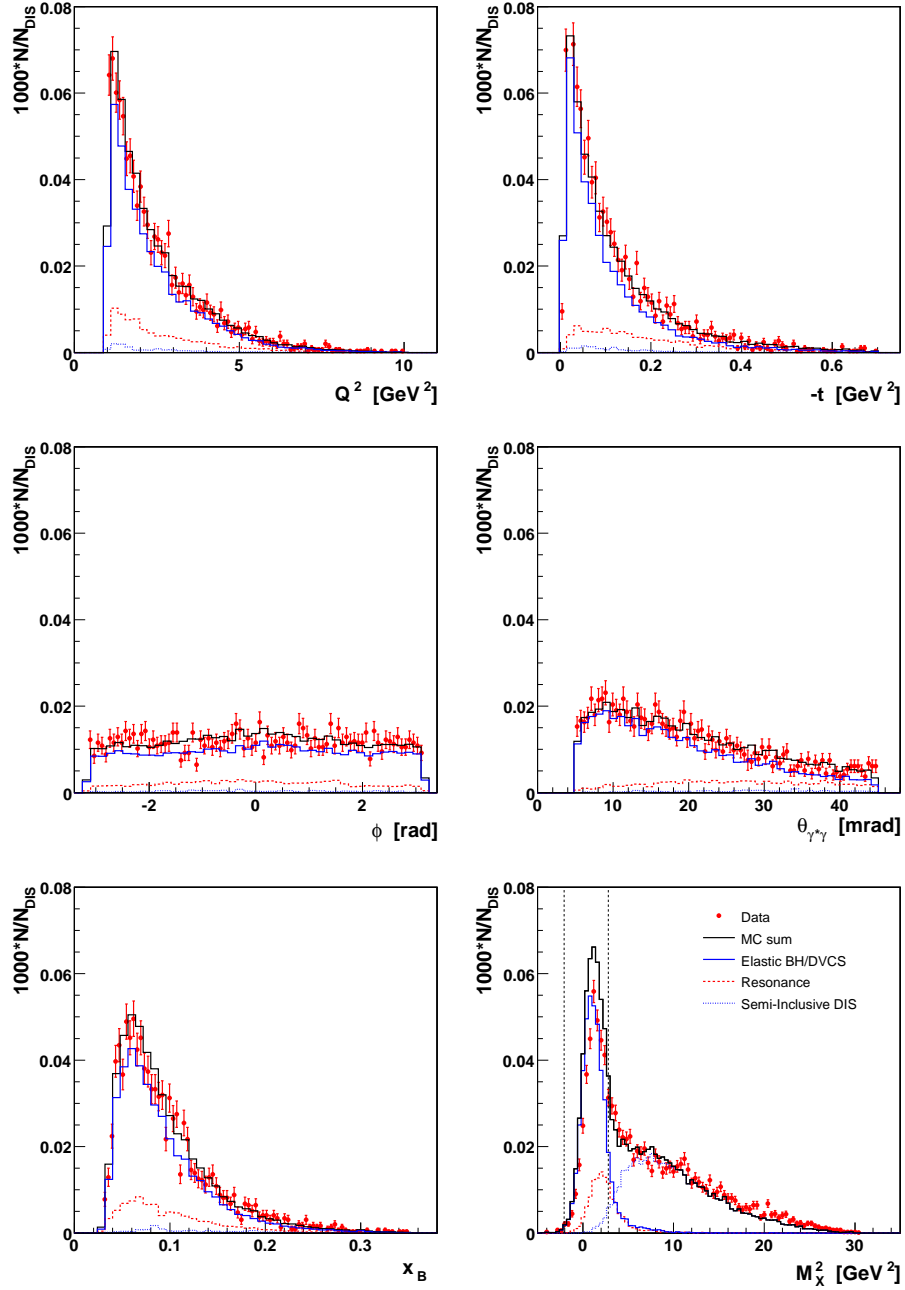
Figure 5.4: Kinematic distributions showing the comparison between the DIS-normalised experimental yield with an MC simulation, showing the contribution from each process at exclusive event level for Q^2, $-t$, ϕ, $\theta_{\gamma^*\gamma}$, x_B and at SPE-level for M_X^2. The errors shown are purely statistical.
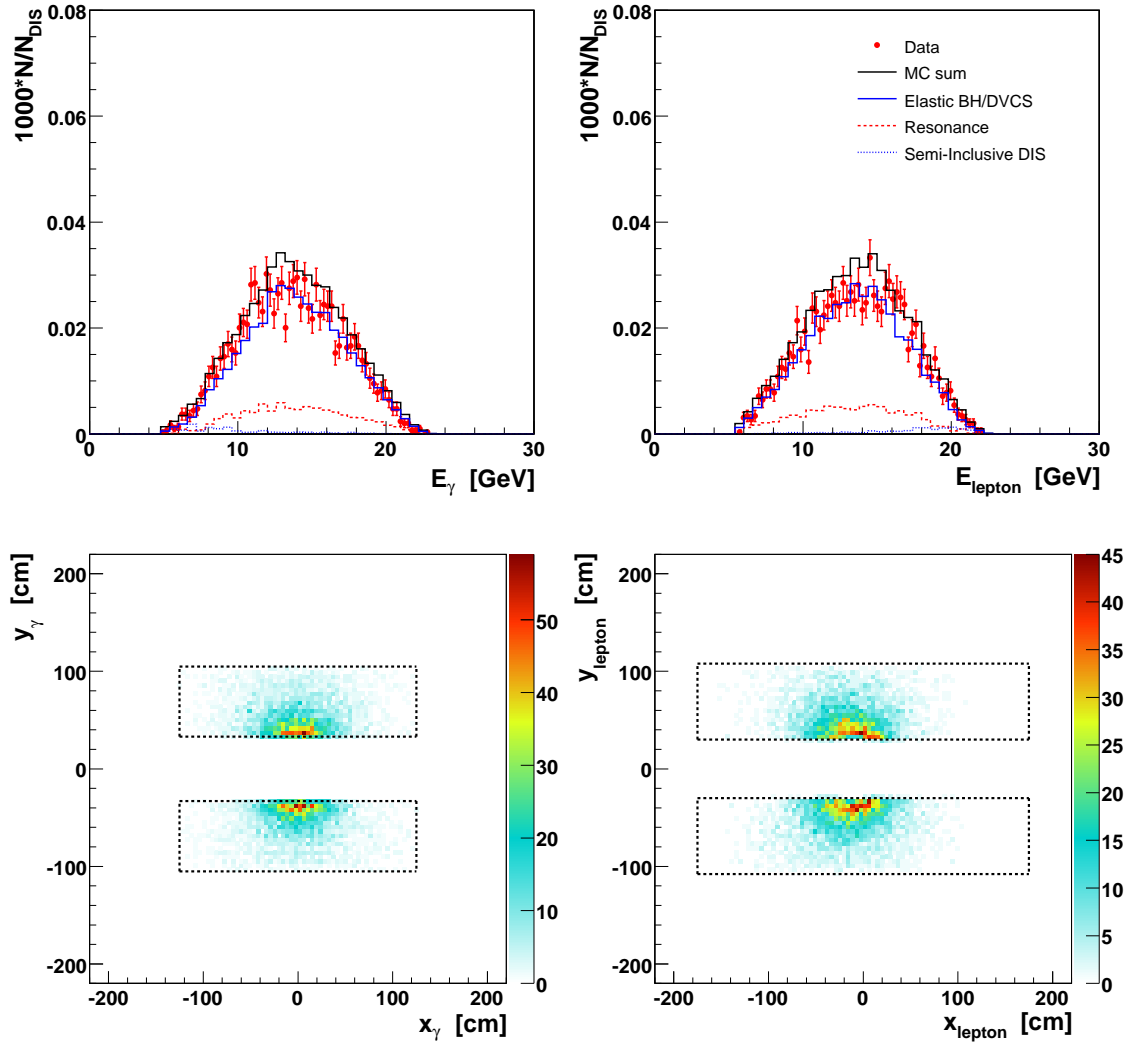
Figure 5.5: (top): Kinematic distributions showing the comparison between the DIS-normalised experimental yield with an MC simulation, showing the contribution from each process at exclusive event level for E_γ (left) and E_{lepton} (right). The errors shown are purely statistical. (bottom): Spatial distributions in the x-y plane of the energy deposition of the photon (left) and the lepton track (right) in the calorimeter at SPE-level. The dotted lines highlight the fiducial volume of the calorimeter.
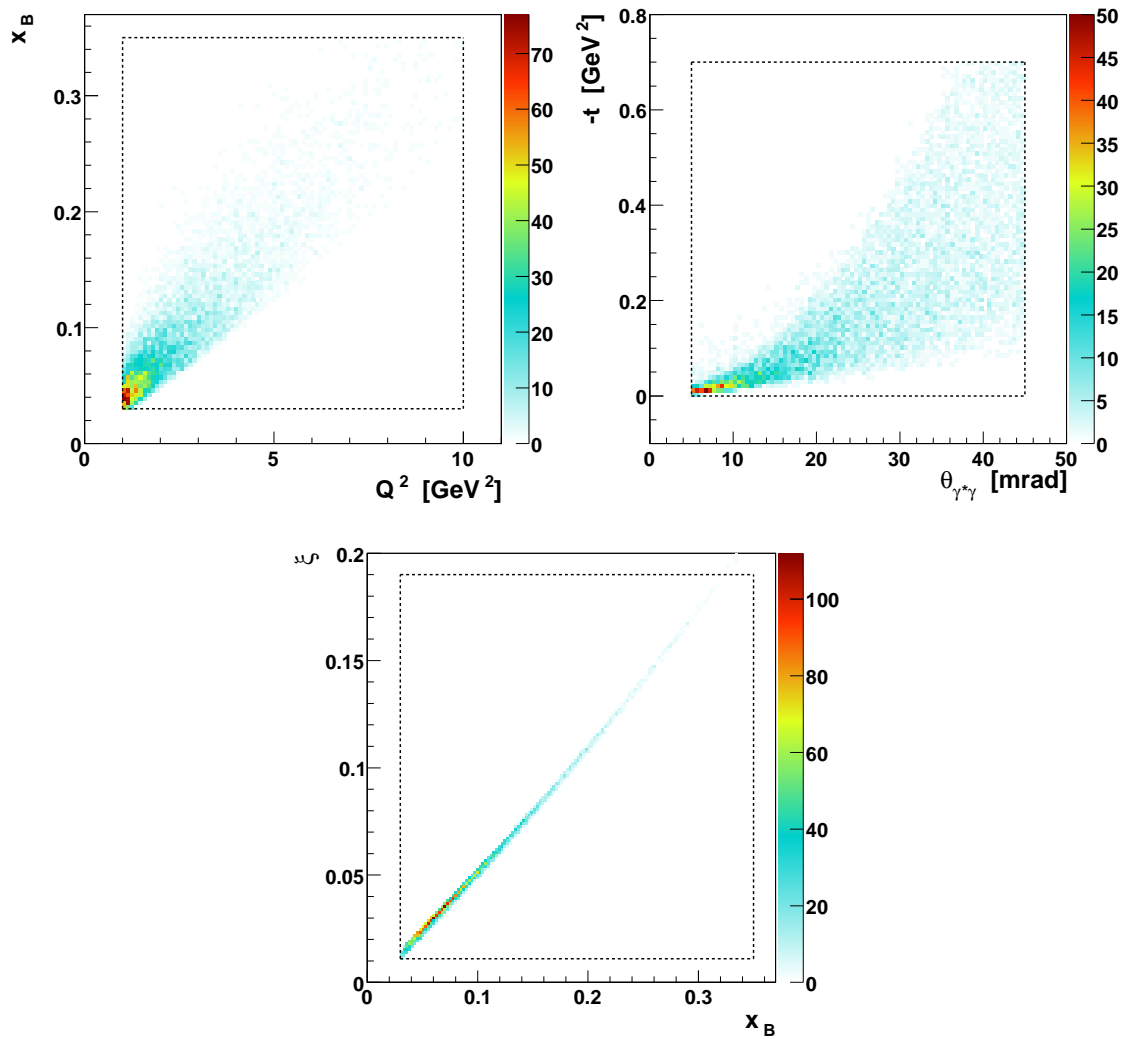
Figure 5.6: Two-dimensional distributions at SPE-level showing the correlation between x_{B} and Q^2 (top left), between $-t$ and $\theta_{\gamma^*\gamma}$ (top right), and between ξ and x_{B} (bottom). The dotted lines highlight the regions allowed by the kinematic data constraints.

5.3 Cross-Check of the Data Selection

An independent cross-check of the data selection and extraction procedures was necessary to ensure the accuracy of the analysis results. For this particular analysis a two-step procedure was performed with Caroline Riedl of DESY (data selection) and Aram Movsisyan of the Yerevan Physics Institute, Armenia (extraction method). Table 5.1 compares the exclusive "DVCS" event yields of the cross-check for each beam and target polarisation state. No differences in the exclusive event yield or integrated luminosity were observed and the discrepancies in the determination of the average beam polarisations were found to be, at worst, 0.1%.

Section 5.7 shows the results of the cross-check of the independent fitting routines.

			$B^\rightarrow T^\Leftarrow$	$B^\rightarrow T^\Rightarrow$	$B^\leftarrow T^\Leftarrow$	$B^\leftarrow T^\Rightarrow$
96d0	DVCS Events	Mahon	402	431	-	-
		Riedl	402	431	-	-
	L	Mahon	17361290.17	17353273.64	-	-
		Riedl	17361290.17	17353273.64	-	-
	$\langle P_\ell \rangle$ [%]	Mahon	51.38	51.39	-	-
		Riedl	51.38	51.40	-	-
97d1	DVCS Events	Mahon	168	210	845	769
		Riedl	168	210	845	769
	L	Mahon	10116931.17	10121351.18	38797412.22	38731751.31
		Riedl	10116931.17	10121351.18	38797412.22	38731751.31
	$\langle P_\ell \rangle$ [%]	Mahon	49.69	49.75	-53.10	-53.05
		Riedl	49.70	49.74	-53.05	-53.05

Table 5.1: Table showing the data selection cross-check with Caroline Riedl. The number of exclusive "DVCS" events are presented separately for each data year and beam and target polarisation state, alongside values of the average beam polarisation P_ℓ and integrated luminosities L.
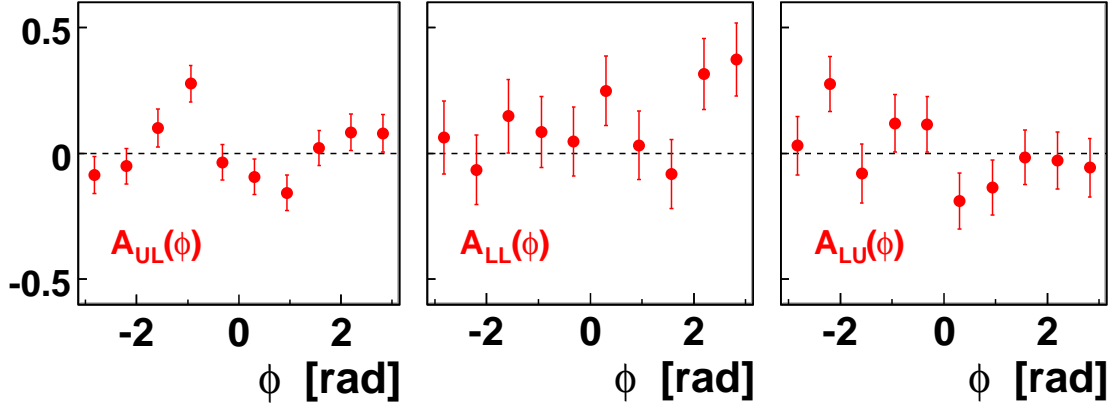
Figure 5.7: The ϕ-dependence of the longitudinal target-spin asymmetry $\mathcal{A}_{\mathrm{UL}}$, the double-spin asymmetry $\mathcal{A}_{\mathrm{LL}}$ and the beam-helicity asymmetry $\mathcal{A}_{\mathrm{LU}}$. The data points are calculated from Eqs. $5.16 - 5.18$.

5.4   Azimuthal Dependences

The azimuthal dependences of the three extracted asymmetries are given by

$$\mathcal{A}_{\mathrm{UL}}\left(\phi\right) = \frac{1}{|\langle P_{\mathrm{L}}\rangle|} \frac{\left(\frac{N^{\leftarrow\Rightarrow}(\phi)}{L^{\leftarrow\Rightarrow}} + \frac{N^{\rightarrow\Rightarrow}(\phi)}{L^{\rightarrow\Rightarrow}}\right) - \left(\frac{N^{\leftarrow\Leftarrow}(\phi)}{L^{\leftarrow\Leftarrow}} + \frac{N^{\rightarrow\Leftarrow}(\phi)}{L^{\rightarrow\Leftarrow}}\right)}{\left(\frac{N^{\leftarrow\Rightarrow}(\phi)}{L^{\leftarrow\Rightarrow}} + \frac{N^{\rightarrow\Rightarrow}(\phi)}{L^{\rightarrow\Rightarrow}}\right) + \left(\frac{N^{\leftarrow\Leftarrow}(\phi)}{L^{\leftarrow\Leftarrow}} + \frac{N^{\rightarrow\Leftarrow}(\phi)}{L^{\rightarrow\Leftarrow}}\right)}, \qquad (5.16)$$

$$\mathcal{A}_{\mathrm{LL}}\left(\phi\right) = \frac{1}{|\langle P_{\ell}P_{\mathrm{L}}\rangle|} \frac{\left(\frac{N^{\rightarrow\Rightarrow}(\phi)}{L^{\rightarrow\Rightarrow}} + \frac{N^{\leftarrow\Leftarrow}(\phi)}{L^{\leftarrow\Leftarrow}}\right) - \left(\frac{N^{\leftarrow\Rightarrow}(\phi)}{L^{\leftarrow\Rightarrow}} + \frac{N^{\rightarrow\Leftarrow}(\phi)}{L^{\rightarrow\Leftarrow}}\right)}{\left(\frac{N^{\rightarrow\Rightarrow}(\phi)}{L^{\rightarrow\Rightarrow}} + \frac{N^{\leftarrow\Leftarrow}(\phi)}{L^{\leftarrow\Leftarrow}}\right) + \left(\frac{N^{\leftarrow\Rightarrow}(\phi)}{L^{\leftarrow\Rightarrow}} + \frac{N^{\rightarrow\Leftarrow}(\phi)}{L^{\rightarrow\Leftarrow}}\right)}, \qquad (5.17)$$

$$\mathcal{A}_{\mathrm{LU}}\left(\phi\right) = \frac{1}{|\langle P_{\ell}\rangle|} \frac{\left(\frac{N^{\rightarrow\Leftarrow}(\phi)}{L^{\rightarrow\Leftarrow}} + \frac{N^{\rightarrow\Rightarrow}(\phi)}{L^{\rightarrow\Rightarrow}}\right) - \left(\frac{N^{\leftarrow\Leftarrow}(\phi)}{L^{\leftarrow\Leftarrow}} + \frac{N^{\leftarrow\Rightarrow}(\phi)}{L^{\leftarrow\Rightarrow}}\right)}{\left(\frac{N^{\rightarrow\Leftarrow}(\phi)}{L^{\rightarrow\Leftarrow}} + \frac{N^{\rightarrow\Rightarrow}(\phi)}{L^{\rightarrow\Rightarrow}}\right) + \left(\frac{N^{\leftarrow\Leftarrow}(\phi)}{L^{\leftarrow\Leftarrow}} + \frac{N^{\leftarrow\Rightarrow}(\phi)}{L^{\leftarrow\Rightarrow}}\right)}, \qquad (5.18)$$

where $N^{\leftrightarrow\Leftrightarrow}$ denotes the photon yield for a specific beam and target polarisation state. In Eq. 5.16 (5.18) the average beam (target) polarisation is assumed to be zero. The azimuthal dependences of these asymmetries are shown in Fig. 5.7, in ten equal bins of ϕ in the range $[-\pi,\pi]$ rad, and integrated over all kinematics in the HERMES acceptance.

5.5   Maximum Likelihood Extraction Method

These asymmetries are simultaneously extracted from the exclusive event sample using the maximum likelihood fitting formalism which is summarised in Ref. [104]. This has an advantage over the standard least-squares method as it provides a fit which is unbinned in ϕ and does not suffer from problems evaluating the constant $\cos(0\phi)$ terms in an extraction. This technique has been used for all recent HERMES DVCS publications and will

be outlined here with a detailed description of the luminosity-normalised fitting routine unique to this analysis.

5.5.1 The Maximum Likelihood Fitting Technique

The maximum likelihood method estimates the mean values of a parameter set θ describing a probability density function (p.d.f), denoted $p(\mathbf{x}; \theta)$, with N sets of independently measured quantities $\mathbf{x} \in \{-t, x_{\mathrm{B}}, Q^2, \phi\}$. This is achieved by maximising the standard likelihood function $\mathcal{L}_{\mathrm{ML}}(\theta)$ defined as the product of the probabilities of each individual event i, such that

$$\mathcal{L}_{\mathrm{ML}}(\theta) = \prod_i^N p(\mathbf{x}; \theta)\,. \tag{5.19}$$

Here, potential computational problems may arise from evaluating the product of many small numbers. Alternatively, by minimising the negative, natural-logarithm of the standard likelihood function, *i.e.*

$$-\ln \mathcal{L}_{\mathrm{ML}}(\theta) = -\sum_i^N \ln p(\mathbf{x}_i; \theta)\,, \tag{5.20}$$

the most likely set of parameters θ can be determined.

Generally, the normalisation of a p.d.f is unity, *i.e.* $\int p(\mathbf{x}; \theta)\, d\mathbf{x} = 1$. However, in the case of maximum likelihood the normalisation may depend on the fitted parameters and therefore must be fixed. Assuming the observed distribution of events has a Poisson fluctuation around its expectation value θ, the above function can be 'extended' to include the Poisson p.d.f $\frac{\mathcal{N}^N e^{-\mathcal{N}}}{N!}$. This Extended Maximum Likelihood (EML) function is expressed as

$$\mathcal{L}_{\mathrm{EML}}(\theta) = \frac{\mathcal{N}(\theta)^N e^{-\mathcal{N}(\theta)}}{N!} \prod_i^N p(\mathbf{x}_i; \theta)\,, \tag{5.21}$$

where N is the expected number of events and $\mathcal{N}(\theta)$ can be interpreted as the normalisation of the extended p.d.f, defined as $\mathcal{P}(\mathbf{x}; \theta) \equiv \mathcal{N}(\theta) \cdot p(\mathbf{x}; \theta)$, *i.e.*

$$\mathcal{N}(\theta) = \int \mathcal{P}(\mathbf{x}; \theta)\, d\mathbf{x}\,. \tag{5.22}$$

Equation 5.21 can then be expressed as

$$\begin{aligned} -\ln \mathcal{L}_{\mathrm{EML}}(\theta) &= -N \ln \mathcal{N}(\theta) + \mathcal{N}(\theta) + \ln N! - \sum_i^N \ln p(\mathbf{x}_i; \theta) \\ &= -N \ln \mathcal{N}(\theta) + \mathcal{N}(\theta) + \ln N! - \sum_i^N \ln \mathcal{P}(\mathbf{x}_i; \theta) + \sum_i^N \ln \mathcal{N}(\theta)\,, \end{aligned} \tag{5.23}$$

where the first and last terms of the lower equation cancel, and the constant term $\ln N!$ can be neglected as it does not affect the position of the minimum. The resultant function is therefore given as

$$-\ln \mathcal{L}_{\mathrm{EML}}(\theta) = -\sum_{i}^{N} \ln \mathcal{P}(\mathbf{x}_i; \theta) + \mathcal{N}(\theta) \,. \tag{5.24}$$

In addition, the Standard (SML) and Unnormalised (UML) Maximum Likelihood methods will also be studied. These are expressed as

$$-\ln \mathcal{L}_{\mathrm{SML}}(\theta) = -\sum_{i}^{N} \ln \mathcal{P}(\mathbf{x}_i; \theta) + N \ln \mathcal{N}(\theta) \,, \tag{5.25}$$

$$-\ln \mathcal{L}_{\mathrm{UML}}(\theta) = -\sum_{i}^{N} \ln \mathcal{P}(\mathbf{x}_i; \theta) \,. \tag{5.26}$$

All results in this thesis will be extracted using the EML method which has been shown in experiments with a non-fixed number of events, such as HERMES, to provide a better estimation of parameters and uncertainties compared to the SML method which relies on the expected number of events N [100]. The UML method has the same disadvantage as the standard least-squares method in that the extraction of $\cos(0\phi)$ amplitudes, sensitive to the normalisation, are not properly evaluated.

Results of the asymmetry amplitudes extracted using these three methods are presented in Section 5.7 in comparison with those extracted as a cross-check by Aram Movsisyan.

5.5.2   Fit Function for the Longitudinally Polarised Proton Analysis

For the purposes of this extraction of asymmetry amplitudes using an EML fit, it is necessary to define a suitable normalised 'fit-function'. Section 5.2 detailed the selection of an event yield $\mathcal{N}$. Its expectation value is expressed as

$$\langle \mathcal{N}(P_\ell, P_{\mathrm{L}}, \phi) \rangle = L(P_\ell)\, \eta(\phi)\, \sigma_{\mathrm{UU}}(\phi)$$
$$\times \left[1 + P_{\mathrm{L}}\, \mathcal{A}_{\mathrm{UL}}(\phi) + P_\ell P_{\mathrm{L}}\, \mathcal{A}_{\mathrm{LL}}(\phi) + P_\ell\, \mathcal{A}_{\mathrm{LU}}(\phi) \right], \tag{5.27}$$

where L is the beam polarisation dependent integrated luminosity, σ_{UU} denotes the unpolarised cross-section and η represents the detection efficiency. For the case when $\eta = 1$, the total number of events in a small time $d\tau$ and phase space interval $d\mathbf{x}$ is given as

$$d\mathcal{N}(\mathbf{x}) = \mathcal{L}(\tau)\, d\tau\, d\mathbf{x}\, \sigma_{\mathrm{UU}}(\mathbf{x}) \left[1 + P_{\mathrm{L}}\mathcal{A}_{\mathrm{UL}}(\mathbf{x}) + P_\ell P_{\mathrm{L}}\mathcal{A}_{\mathrm{LL}}(\mathbf{x}) + P_\ell \mathcal{A}_{\mathrm{LU}}(\mathbf{x}) \right]. \tag{5.28}$$

Integrating over all phase space and beam and target polarisation states obtains

$$\mathcal{N}(\theta) = \int N^{\rightarrow\Leftarrow}(\mathbf{x};\theta) + N^{\rightarrow\Rightarrow}(\mathbf{x};\theta) + N^{\leftarrow\Leftarrow}(\mathbf{x};\theta) + N^{\leftarrow\Rightarrow}(\mathbf{x};\theta)\,d\mathbf{x}\,, \quad (5.29)$$

$$\approx \sum_{i=1}^{N} K^{\leftrightarrow\Leftrightarrow}\big[m_{\mathrm{UU}} + m_{\mathrm{UL}}\mathcal{A}_{\mathrm{UL}}(\mathbf{x}_i;\theta) + m_{\mathrm{LL}}\mathcal{A}_{\mathrm{LL}}(\mathbf{x}_i;\theta)$$
$$+ m_{\mathrm{LU}}\mathcal{A}_{\mathrm{LU}}(\mathbf{x}_i;\theta)\big]\,, \quad (5.30)$$

with factors,

$$K^{\rightarrow\Leftarrow} = \frac{1}{2L^{\rightarrow\Leftarrow}(1 - P^{\rightarrow\Leftarrow}/P^{\leftarrow\Leftarrow})}\,, \quad (5.31)$$

$$K^{\rightarrow\Rightarrow} = \frac{1}{2L^{\rightarrow\Rightarrow}(1 - P^{\rightarrow\Rightarrow}/P^{\leftarrow\Rightarrow})}\,, \quad (5.32)$$

$$K^{\leftarrow\Leftarrow} = \frac{1}{2L^{\leftarrow\Leftarrow}(1 - P^{\leftarrow\Leftarrow}/P^{\rightarrow\Leftarrow})}\,, \quad (5.33)$$

$$K^{\leftarrow\Rightarrow} = \frac{1}{2L^{\leftarrow\Rightarrow}(1 - P^{\leftarrow\Rightarrow}/P^{\rightarrow\Rightarrow})}\,, \quad (5.34)$$

and

$$m_{\mathrm{UU}} = L^{\rightarrow\Leftarrow} + L^{\rightarrow\Rightarrow} + L^{\leftarrow\Leftarrow} + L^{\leftarrow\Rightarrow}\,, \quad (5.35)$$

$$m_{\mathrm{UL}} = P_{\mathrm{L}}\,m_{\mathrm{UU}}\,, \quad (5.36)$$

$$m_{\mathrm{LL}} = P_{\mathrm{L}}\,m_{\mathrm{LU}}\,, \quad (5.37)$$

$$m_{\mathrm{LU}} = L^{\rightarrow\Leftarrow}P^{\rightarrow\Leftarrow} + L^{\rightarrow\Rightarrow}P^{\rightarrow\Rightarrow} + L^{\leftarrow\Leftarrow}P^{\leftarrow\Leftarrow} + L^{\leftarrow\Rightarrow}P^{\leftarrow\Rightarrow}\,. \quad (5.38)$$

The EML fit can therefore be performed by minimising the following fit-function summed over each beam and target state:

$$-\ln\mathcal{L}_{\mathrm{EML}}(\theta) = -\sum_{i}^{N}\ln\big[1 + P_{\mathrm{L}}\mathcal{A}_{\mathrm{UL}}(\mathbf{x}_i;\theta) + P_{\ell}P_{\mathrm{L}}\mathcal{A}_{\mathrm{LL}}(\mathbf{x}_i;\theta)$$
$$+ P_{\ell}\mathcal{A}_{\mathrm{LU}}(\mathbf{x}_i;\theta)\big] + \mathcal{N}(\theta)\,, \quad (5.39)$$

where θ here are the set of extracted asymmetry amplitudes of $\mathcal{A}_{\mathrm{UL}}$, $\mathcal{A}_{\mathrm{LL}}$ and $\mathcal{A}_{\mathrm{LU}}$. The extraction is weighted on the event level by the beam polarisation to account for any luminosity imbalances which may arise. The rapid flipping of the target polarisation direction allows the year-averaged values from Table 4.2 to be used in the extraction.

5.6 Linking Extracted Amplitudes and Fourier Coefficients

The extracted asymmetry amplitudes are Fourier-expanded in ϕ as

$$\mathcal{A}_{\mathrm{UL}}(\phi) \;\simeq\; \sum_{n=0}^{2} A_{\mathrm{UL}}^{\cos(n\phi)} \cos(n\phi) + \sum_{n=1}^{3} A_{\mathrm{UL}}^{\sin(n\phi)} \sin(n\phi)\,, \tag{5.40}$$

$$\mathcal{A}_{\mathrm{LL}}(\phi) \;\simeq\; \sum_{n=0}^{2} A_{\mathrm{LL}}^{\cos(n\phi)} \cos(n\phi) + \sum_{n=1}^{2} A_{\mathrm{LL}}^{\sin(n\phi)} \sin(n\phi)\,. \tag{5.41}$$

$$\mathcal{A}_{\mathrm{LU}}(\phi) \;\simeq\; \sum_{n=0}^{2} A_{\mathrm{LU}}^{\cos(n\phi)} \cos(n\phi) + \sum_{n=1}^{2} A_{\mathrm{LU}}^{\sin(n\phi)} \sin(n\phi)\,. \tag{5.42}$$

The $A_{\mathrm{UL}}^{\sin(n\phi)}$, $A_{\mathrm{LL}}^{\cos(n\phi)}$ and $A_{\mathrm{LU}}^{\sin(n\phi)}$ amplitudes are related to the Fourier coefficients appearing in the numerators of the asymmetries in Eqs. 3.16, 3.22 and 3.28 respectively. These relationships are outlined in Table 5.2 which also shows the contributing $\mathcal{C}$-functions and the twist level at which they enter. All other amplitudes have been included as a test of the extraction method and normalisation, and are all expected to be zero across the kinematic range.

For each of the asymmetries, the links between the physics-motivated extracted amplitudes and the Fourier coefficients from the squared-BH $|\tau_{\mathrm{BH}}|^2$, squared-DVCS $|\tau_{\mathrm{DVCS}}|^2$ and interference $\mathcal{I}$ terms of the squared scattering amplitude $|\tau|^2$ are summarised as follows:

- $\mathcal{A}_{\mathrm{UL}}$ — The $A_{\mathrm{UL}}^{\sin\phi}$ amplitude is related to the leading-twist $s_{1,\mathrm{LP}}^{\mathcal{I}}$ coefficient from $\mathcal{I}$ and also receives a $\frac{1}{Q}$ suppressed contribution arising from $|\tau_{\mathrm{DVCS}}|^2$ entering at twist–3 level. The dominant contribution from $\mathcal{I}$ allows information relating to the imaginary part of CFF $\widetilde{\mathcal{H}}$ from $\mathcal{C}_{\mathrm{LP}}^{\mathcal{I}}$ to be accessed. The $A_{\mathrm{UL}}^{\sin(2\phi)}$ amplitude relates to the same $\mathcal{C}_{\mathrm{LP}}^{\mathcal{I}}$-function at twist–3 level with a further $\frac{\alpha_{\mathrm{s}}}{\pi}$ suppressed contribution from leading-order gluon-helicity-flip CFFs from $|\tau_{\mathrm{DVCS}}|^2$. The $A_{\mathrm{UL}}^{\sin(3\phi)}$ amplitude relates solely to leading-order gluon-helicity-flip CFFs and as such is beyond the scope of this analysis, other than to verify the theoretical prediction of a small amplitude.

- $\mathcal{A}_{\mathrm{LL}}$ — The $A_{\mathrm{LL}}^{\cos(0\phi)}$ and $A_{\mathrm{LL}}^{\cos\phi}$ amplitudes relate to Fourier coefficients, appearing in the numerator of Eq. 3.22, arising from all three terms of the squared scattering amplitude. They both receive a leading-twist contribution from the CFFs appearing in $\mathcal{C}_{\mathrm{LP}}^{\mathcal{I}}$ with $A_{\mathrm{LL}}^{\cos(0\phi)}$ $\left(A_{\mathrm{LL}}^{\cos\phi}\right)$ also relating to the twist–2 (twist–3) coefficient $c_{0,\mathrm{LP}}^{\mathrm{DVCS}}$ $(c_{1,\mathrm{LP}}^{\mathrm{DVCS}})$ from $|\tau_{\mathrm{DVCS}}|^2$. Both receive dominating contributions from the corresponding Fourier coefficient from $|\tau_{\mathrm{BH}}|^2$. The pure twist–3 coefficient $c_{2,\mathrm{LP}}^{\mathcal{I}}$ is related to

Asymmetry Amplitude	Contributing Fourier-Coefficient	Twist Level	CFF Dependence
$A_{\mathrm{UL}}^{\sin\phi}$	$s_{1,\mathrm{LP}}^{\mathcal{I}}$	2	$\Im\mathfrak{m}\,\mathcal{C}_{\mathrm{LP}}^{\mathcal{I}}$
	$s_{1,\mathrm{LP}}^{\mathrm{DVCS}}$	3	$\Im\mathfrak{m}\,\mathcal{C}_{\mathrm{LP}}^{\mathrm{DVCS}}$
$A_{\mathrm{UL}}^{\sin(2\phi)}$	$s_{2,\mathrm{LP}}^{\mathcal{I}}$	3	$\Im\mathfrak{m}\,\mathcal{C}_{\mathrm{LP}}^{\mathcal{I}}$
	$s_{2,\mathrm{LP}}^{\mathrm{DVCS}}$	2	$\Im\mathfrak{m}\,\mathcal{C}_{\mathrm{T,LP}}^{\mathrm{DVCS}}$
$A_{\mathrm{UL}}^{\sin(3\phi)}$	$s_{3,\mathrm{LP}}^{\mathcal{I}}$	2	$\Im\mathfrak{m}\,\mathcal{C}_{\mathrm{T,LP}}^{\mathcal{I}}$
$A_{\mathrm{LL}}^{\cos(0\phi)}$	$c_{0,\mathrm{LP}}^{\mathcal{I}}$	2	$\Re\mathfrak{e}\,\mathcal{C}_{\mathrm{LP}}^{\mathcal{I}}$
	$c_{0,\mathrm{LP}}^{\mathrm{DVCS}}$	2	$\Re\mathfrak{e}\,\mathcal{C}_{\mathrm{LP}}^{\mathrm{DVCS}}$
	$c_{0,\mathrm{LP}}^{\mathrm{BH}}$	-	-
$A_{\mathrm{LL}}^{\cos\phi}$	$c_{1,\mathrm{LP}}^{\mathcal{I}}$	2	$\Re\mathfrak{e}\,\mathcal{C}_{\mathrm{LP}}^{\mathcal{I}}$
	$c_{1,\mathrm{LP}}^{\mathrm{DVCS}}$	3	$\Re\mathfrak{e}\,\mathcal{C}_{\mathrm{LP}}^{\mathrm{DVCS}}$
	$c_{1,\mathrm{LP}}^{\mathrm{BH}}$	-	-
$A_{\mathrm{LL}}^{\cos(2\phi)}$	$c_{2,\mathrm{LP}}^{\mathcal{I}}$	3	$\Re\mathfrak{e}\,\mathcal{C}_{\mathrm{LP}}^{\mathcal{I}}$
$A_{\mathrm{LU}}^{\sin\phi}$	$s_{1,\mathrm{u}}^{\mathcal{I}}$	2	$\Im\mathfrak{m}\,\mathcal{C}_{\mathrm{u}}^{\mathcal{I}}$
	$s_{1,\mathrm{u}}^{\mathrm{DVCS}}$	3	$\Im\mathfrak{m}\,\mathcal{C}_{\mathrm{u}}^{\mathrm{DVCS}}$
$A_{\mathrm{LU}}^{\sin(2\phi)}$	$s_{2,\mathrm{u}}^{\mathcal{I}}$	3	$\Im\mathfrak{m}\,\mathcal{C}_{\mathrm{u}}^{\mathcal{I}}$

Table 5.2: Summary of the links between the asymmetry amplitudes extracted from the data set and the coefficients from the Fourier expansion of $|\tau|^2$. Amplitudes with a dependence on twist–2 gluon-helicity-flip CFFs through the $\mathcal{C}_{\mathrm{T}}$-functions are suppressed by a further factor of $\frac{\alpha_{\mathrm{s}}}{\pi}$.

the $A_{\mathrm{LL}}^{\cos(2\phi)}$ amplitude. All these amplitudes offer some possibility to access information on the real part of CFF $\widetilde{\mathcal{H}}$. Despite the $A_{\mathrm{LL}}^{\cos(0\phi)}$ appearing purely at twist–2 level, the separate contributions cannot be disentangled with only one beam charge available for this analysis. As a result, the easiest access to $\widetilde{\mathcal{H}}$ arises via the $A_{\mathrm{LL}}^{\cos\phi}$ amplitude.

- $\mathcal{A}_{\mathrm{LU}}$ − The $A_{\mathrm{LU}}^{\sin\phi}$ amplitude is related at twist–2 and twist–3 level to the imaginary part of a combination of CFFs via the $\mathcal{C}_{\mathrm{u}}^{\mathcal{I}}$ and $\mathcal{C}_{\mathrm{u}}^{\mathrm{DVCS}}$ functions respectively. In this case, the dominant CFF in question is $\mathcal{H}$ from $\mathcal{C}_{\mathrm{u}}^{\mathcal{I}}$. The $A_{\mathrm{LU}}^{\sin(2\phi)}$ amplitude relates to the $\frac{1}{Q}$ suppressed twist–3 coefficient $s_{2,\mathrm{u}}^{\mathcal{I}}$.

This discussion has not considered the possible influence on the extracted amplitudes from the ϕ-dependent lepton propagators and correlations between the extracted amplitudes in

Variable	Bin 1	Bin 2	Bin 3	Bin 4	Units
$-t$	0.00 - 0.06	0.06 - 0.14	0.14 - 0.30	0.30 - 0.70	GeV^2
x_B	0.03 - 0.07	0.07 - 0.10	0.10 - 0.15	0.15 - 0.35	-
Q^2	1.0 - 1.5	1.5 - 2.3	2.3 - 3.5	3.5 - 10.0	GeV^2

Table 5.3: The kinematic binning in $-t$, x_B, and Q^2 used in this analysis.

Eqs. $5.40 - 5.42$. However, the correlations were determined from the fitting procedure and were found to be small. This is shown in Appendix A.

5.7 Asymmetry Amplitude Extraction and Cross-Check

The asymmetry amplitudes from Eqs. $5.40 - 5.42$ were extracted and the results are shown in Figs. $5.8 - 5.10$ for the amplitudes related to Fourier coefficients in Table 5.2. They are presented in kinematic bins of $-t$, x_B, and Q^2 and integrated over all kinematics, *i.e.* the extraction is performed in a single bin. The standard HERMES binning from Ref. [22] and given in Table 5.3 was used.

These amplitudes are shown in comparison with those independently determined by the cross-check process. Both sets show near-perfect agreement between the independent analyses across all plotted kinematics.

Of these eight amplitudes, the leading-twist $A_{\mathrm{UL}}^{\sin\phi}$, $A_{\mathrm{LL}}^{\cos(0\phi)}$ and $A_{\mathrm{LU}}^{\sin\phi}$ amplitudes, and the twist–3 $A_{\mathrm{UL}}^{\sin(2\phi)}$ amplitude are found to be non-zero. All other amplitudes are consistent with zero across the plotted ranges in $-t$, x_B, and Q^2.

The terms added as a consistency-test of the extraction method are shown in Appendix B. These are all shown to be compatible with zero as expected.

Maximum Likelihood Method Comparison

Figure 5.11 shows the $A_{\mathrm{UL}}^{\sin(n\phi)}$ and $A_{\mathrm{LL}}^{\cos(n\phi)}$ amplitudes extracted using the three methods introduced in Section 5.5.1. It is observed that these routines, which differ only in their approaches to normalisation, are consistent.
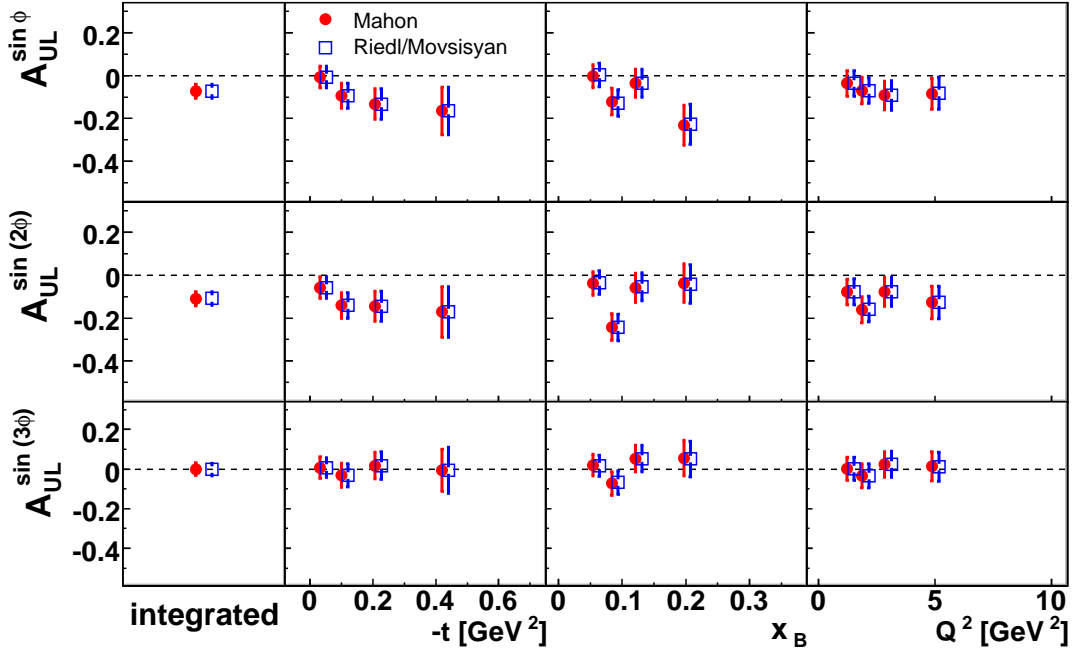
Figure 5.8: Cross check of the extracted $A_{\mathrm{UL}}^{\sin(n\phi)}$ amplitudes integrated over all kinematics in the HER-MES acceptance and as a function of $-t$, x_{B}, and Q^2. The two sets of amplitudes are observed to be in near-perfect agreement across the entire kinematic range.
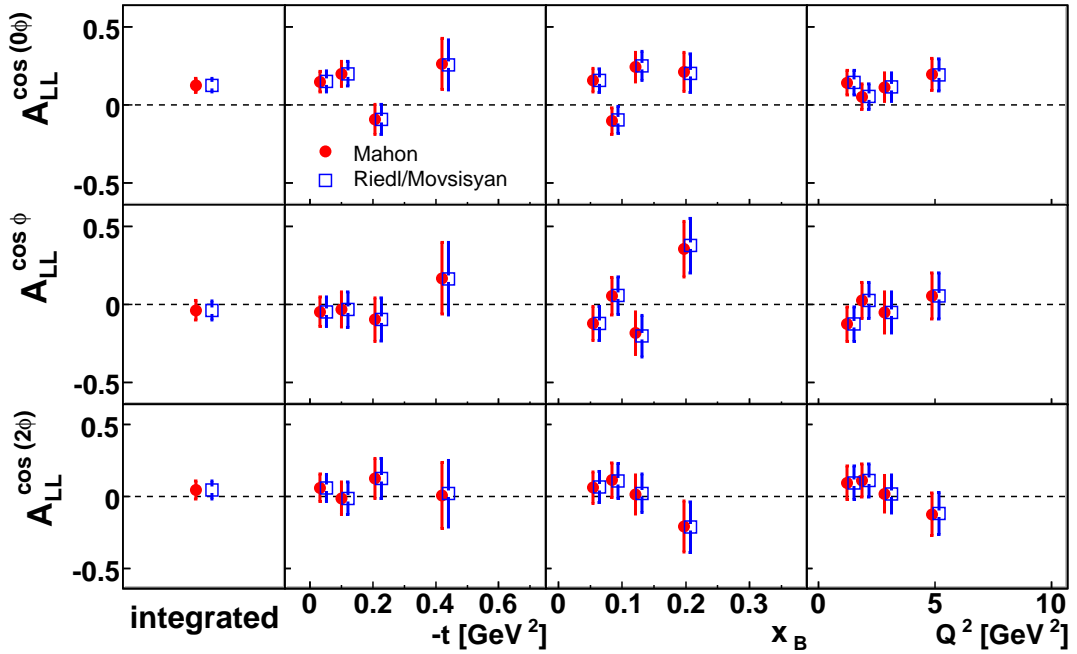
Figure 5.9: Cross check of the extracted $A_{\mathrm{LL}}^{\cos(n\phi)}$ amplitudes integrated over all kinematics in the HER-MES acceptance and as a function of $-t$, x_{B}, and Q^2. The two sets of amplitudes are observed to be in near-perfect agreement across the entire kinematic range.
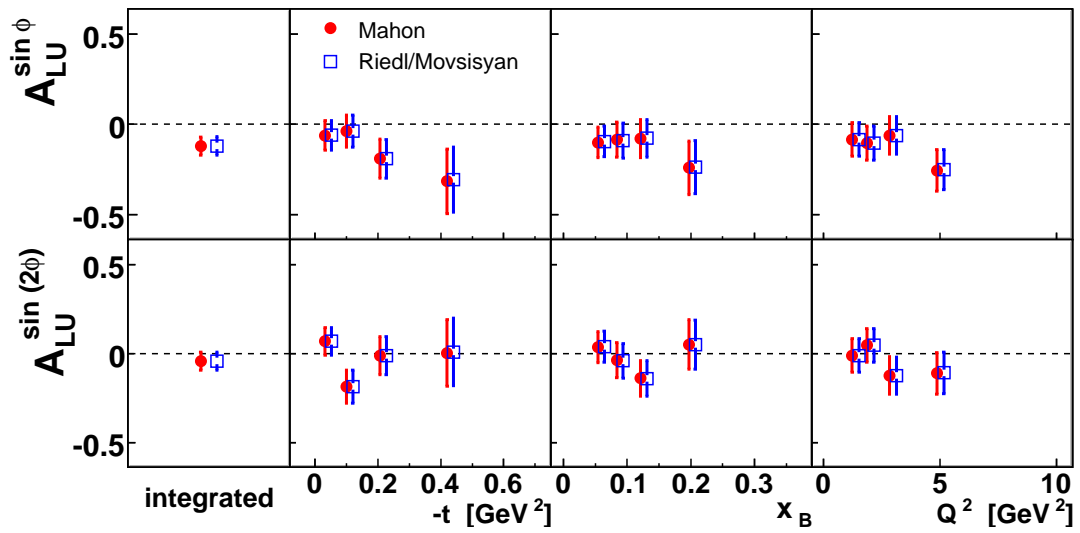
Figure 5.10: Cross check of the extracted $A_{\mathrm{LU}}^{\sin(n\phi)}$ amplitudes integrated over all kinematics in the HER-MES acceptance and as a function of $-t$, x_{B}, and Q^2. The two sets of amplitudes are observed to be in near-perfect agreement across the entire kinematic range.
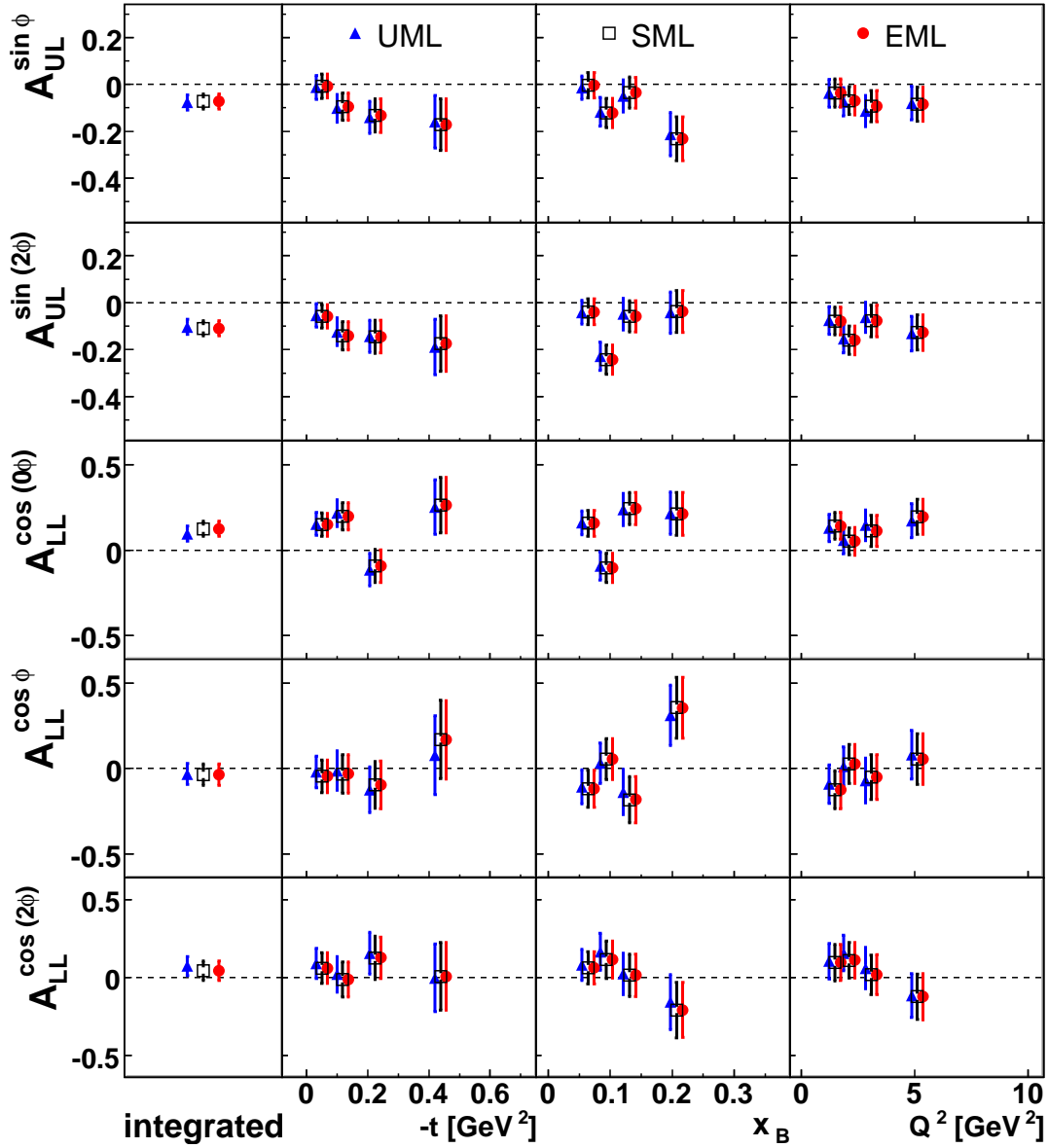
Figure 5.11: Comparison of the extracted $A_{\mathrm{UL}}^{\sin(n\phi)}$ and $A_{\mathrm{LL}}^{\cos(n\phi)}$ amplitudes using the UML (triangles), SML (squares) and EML (circles) methods for each $-t$, x_{B}, and Q^2 bin. Across the kinematic range there are no significant differences between the three extraction methods studied.

5.8 Final Amplitude Extraction

HERMES has published results of the $\mathcal{A}_{\mathrm{LU}}$ from the $1996 - 2005$ hydrogen data set. This significantly larger data set has both electron and positron beam data allowing the separation of the contributions from $|\tau_{\mathrm{DVCS}}|^2$ and $\mathcal{I}$ [23]. The analysis presented in this thesis uses a subset of approximately 10% of this larger data set. Therefore, only the $\mathcal{A}_{\mathrm{UL}}$ and $\mathcal{A}_{\mathrm{LL}}$ asymmetries will be extracted in the following. The final extraction will determine only the physics-motivated amplitudes from Table 5.2 and will now neglect the terms introduced as consistency tests (with the exception of $A_{\mathrm{UL}}^{\cos(0\phi)}$ which will provide a check of the normalisation) and higher harmonics up to $n = 4$ which are compatible with zero. The terms extracted are

$$\mathcal{A}_{\mathrm{UL}}(\phi) \simeq A_{\mathrm{UL}}^{\cos(0\phi)} + \sum_{n=1}^{3} A_{\mathrm{UL}}^{\sin(n\phi)} \sin(n\phi), \qquad (5.43)$$

$$\mathcal{A}_{\mathrm{LL}}(\phi) \simeq \sum_{n=0}^{2} A_{\mathrm{LL}}^{\cos(n\phi)} \cos(n\phi). \qquad (5.44)$$

The comparisons between these extracted amplitudes and those in Eqs. 5.40 and 5.41 are presented in Fig. 5.12 for $\mathcal{A}_{\mathrm{UL}}$ and $\mathcal{A}_{\mathrm{LL}}$. Minor differences are observed across the kinematic projections with some larger differences observed in the lower statistics bins. The extraction of the consistency test $A_{\mathrm{UL}}^{\cos(0\phi)}$ and gluon twist–2 $A_{\mathrm{UL}}^{\sin(3\phi)}$ amplitudes presented in Fig. 5.13 are shown to be consistent with zero across the kinematic range as expected. In Chapter 7 the results of the $A_{\mathrm{LU}}^{\sin(n\phi)}$ amplitudes from the cross-check extraction will be presented in comparison with the results from the $1996 - 2005$ hydrogen data set from Ref. [23]. These amplitudes are shown to be consistent within experimental uncertainty. The correlation matrix for this fit is shown in Appendix A.
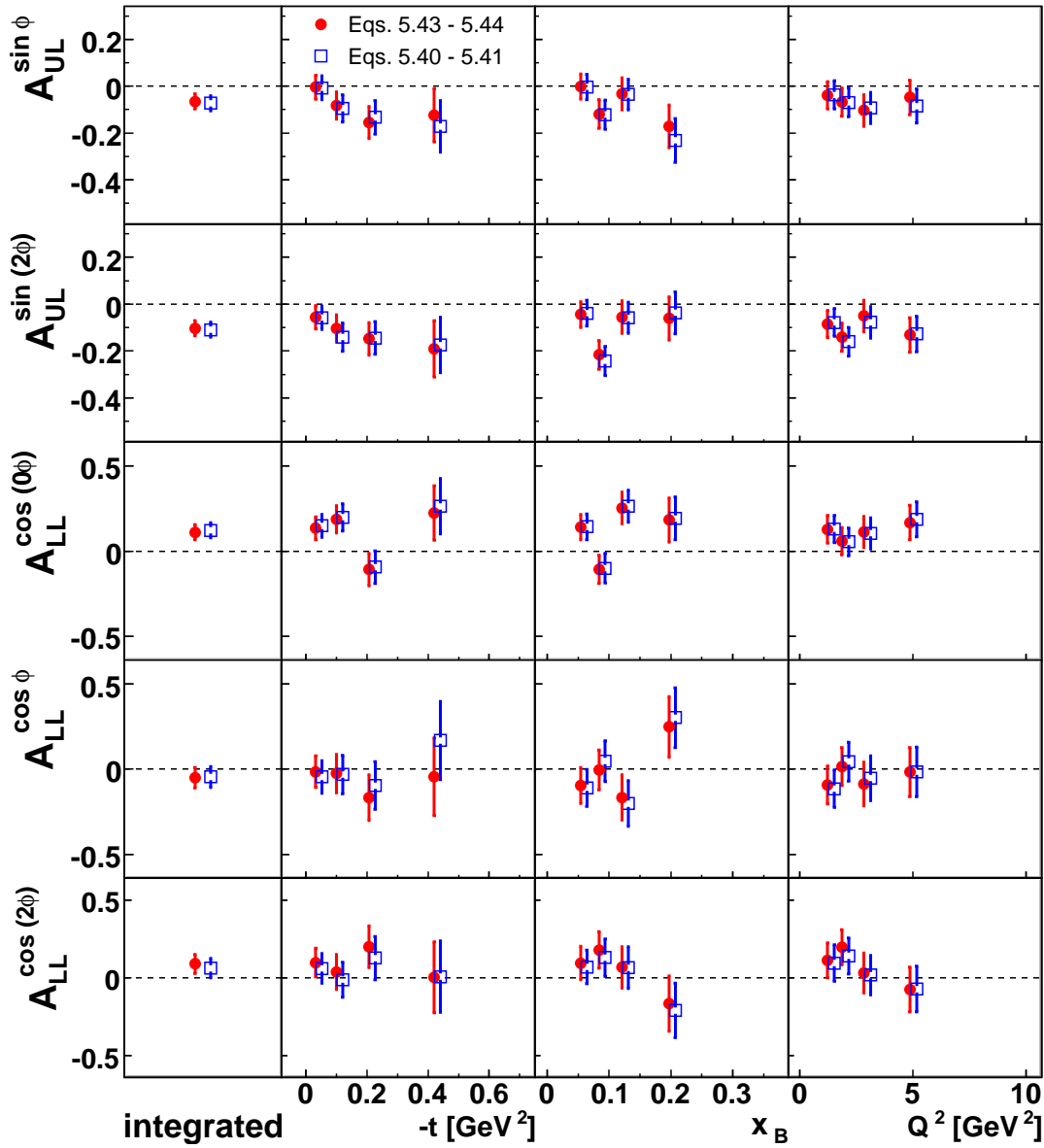
Figure 5.12: Comparison of the $A_{\mathrm{UL}}^{\sin(n\phi)}$ and $A_{\mathrm{LL}}^{\cos(n\phi)}$ amplitudes extracted using Eqs. $5.40 - 5.41$ and $5.43 - 5.44$ shown integrated over all kinematics in the HERMES acceptance and as a function of $-t$, x_{B}, and Q^2. Minor differences in the extracted amplitudes are observed with the largest in the lower statistics bins.
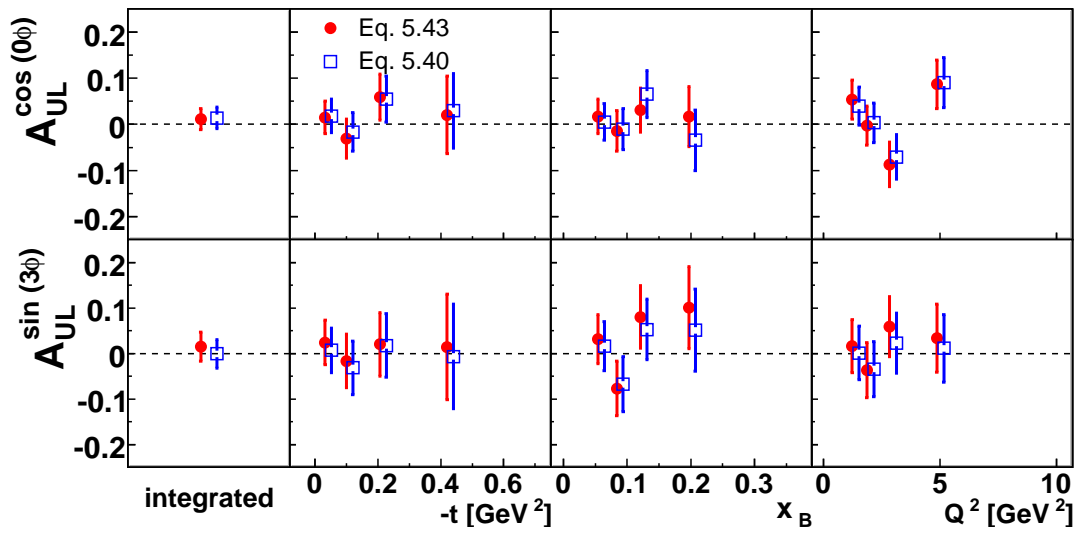
Figure 5.13: Comparison of the consistency test, $A_{\mathrm{UL}}^{\cos(0\phi)}$ and suppressed $A_{\mathrm{UL}}^{\sin(3\phi)}$ amplitudes extracted using Eqs. 5.40 and 5.43 shown integrated over all kinematics in the HERMES acceptance and as a function of $-t$, x_{B}, and Q^2.

Chapter 6

Determination of Systematic Uncertainties

Several sources of systematic uncertainty pertain to the results presented in this thesis. This chapter will outline the nature of each of the contributions and detail the methods undertaken to determine their extent. The following effects are considered:

1. $\delta_{M_\mathrm{X}^2}$ – Uncertainty introduced by accounting for shifts in the mean values of the M_X^2 distributions between data-taking years.

2. δ_Bg – Effect of the corrections applied to remove asymmetry contributions from background processes.

3. δ_4in1 – '4-in-1' method accounting for the correlated effects of detector misalignment, smearing, acceptance and finite bin-width introduced by binning the data in kinematic bins of $-t$, x_B, and Q^2.

In addition, the following contributions have been studied:

- Systematic uncertainty inherent in the measurement of the integrated luminosity. No systematic uncertainty was assigned for this as the luminosity does not depend on the target polarisation and the asymmetry extraction was weighted at event level by the beam polarisation to account for luminosity imbalances.

- Scale uncertainty of 3.4% (4.2%) arising from the systematic uncertainty in the measurements of P_ℓ (P_L) which is propagated to the asymmetry. These are shown in Table 4.2 and in the captions of the final results figures.

- Possible contributions from tracking and trigger inefficiencies have been studied in Ref. [63] and were found to be negligible. Therefore, no corresponding systematic uncertainty will be assigned.

- Uncertainties arising from possible extra QED vertices, *i.e.* radiative corrections, have been estimated to be less than 0.1% and are therefore neglected [105].

6.1 Missing-Mass Shift

For the analysis of transversely polarised hydrogen data (see Section 3.4.2) taken after the installation of the RICH, an exclusive region of $-2.25\,\mathrm{GeV}^2 \leq M_X^2 \leq 2.89\,\mathrm{GeV}^2$ was determined from MC simulation [22]. After the longitudinally polarised data-taking, the RICH was installed upstream of the electromagnetic calorimeter. The presence of this additional material has a detrimental effect on the resolution of the calorimeter measurement of the photon momentum. This $\sim 6\%$ decrease in momentum resolution, observed from studies shown in Ref. [63], was propagated to the calculation of M_X^2. Thus, with an improved pre-RICH M_X^2 resolution, a refined exclusive region was determined and found to be approximately $250\,\mathrm{MeV}^2$ narrower and shifted giving

$$-2.08\,\mathrm{GeV}^2 \leq M_X^2 \leq 2.81\,\mathrm{GeV}^2\,. \tag{6.1}$$

However, during the analysis detailed in this thesis, a shift was discovered between the mean values of the 96d0 and 97d1 exclusive M_X^2 distributions shown in Fig. 6.1. Separate year-specific exclusive regions were determined to be

$$96\mathrm{d}0: \quad -2.22\,\mathrm{GeV}^2 \leq M_X^2 \leq 2.68\,\mathrm{GeV}^2\,, \tag{6.2}$$

$$97\mathrm{d}1: \quad -2.00\,\mathrm{GeV}^2 \leq M_X^2 \leq 2.89\,\mathrm{GeV}^2\,. \tag{6.3}$$

The effect these 'shifted' regions have on the exclusive yield compared to the 'original' region is shown in Table 6.1 for each beam and target state. An overall increase in statistics of around 1.5% is observed.

Figure 6.2 shows the corresponding effect on the extracted $A_{\mathrm{UL}}^{\sin(n\phi)}$ and $A_{\mathrm{LL}}^{\cos(n\phi)}$ amplitudes. The differences in the extracted amplitudes are shown to be minor for both asymmetries, with the biggest variation of 0.05 observed in low statistics bins which are subject to larger contributions from background processes.
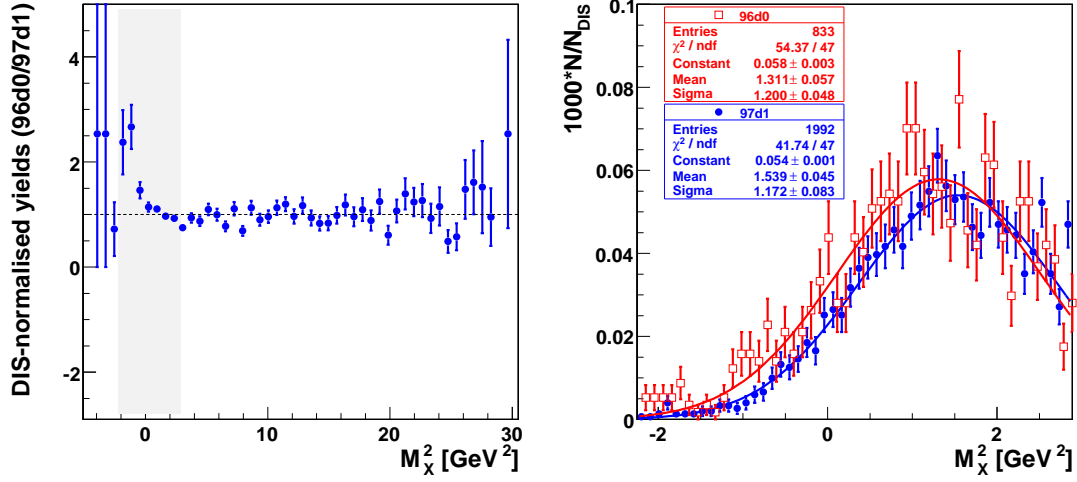
Figure 6.1: Comparisons of the normalised M_X^2 distributions between the two data productions analysed, 96d0 and 97d1. (left): The ratio of the normalised exclusive event yields (96d0/97d1) as a function of M_X^2. A shift in the exclusive peaks is observed. (right): M_X^2 distributions for the 96d0 and 97d1 productions within the exclusive region $-2.08\,\text{GeV}^2 \leq M_X^2 \leq 2.81\,\text{GeV}^2$. The Gaussian fit parameters are shown, from which the new year-specific M_X^2 exclusive regions are calculated.

As the underlying cause of this M_X^2-shift is not fully understood, a systematic uncertainty $\delta_{M_X^2}$ equal to one quarter of the effect this shift has on the extracted amplitudes is assigned to account for any uncertainty introduced by the missing-mass correction.

	DVCS Events	$B^{\rightarrow}T^{\Leftarrow}$	$B^{\rightarrow}T^{\Rightarrow}$	$B^{\leftarrow}T^{\Leftarrow}$	$B^{\leftarrow}T^{\Rightarrow}$
96d0	Original	402	431	-	-
	Shifted	397	422	-	-
97d1	Original	168	210	845	769
	Shifted	172	215	864	791

Table 6.1: Comparison between the exclusive events for each beam and target polarisation state selected using the original (Eq. 6.1) and shifted, year-dependent exclusive regions (Eqs. 6.2 and 6.3).

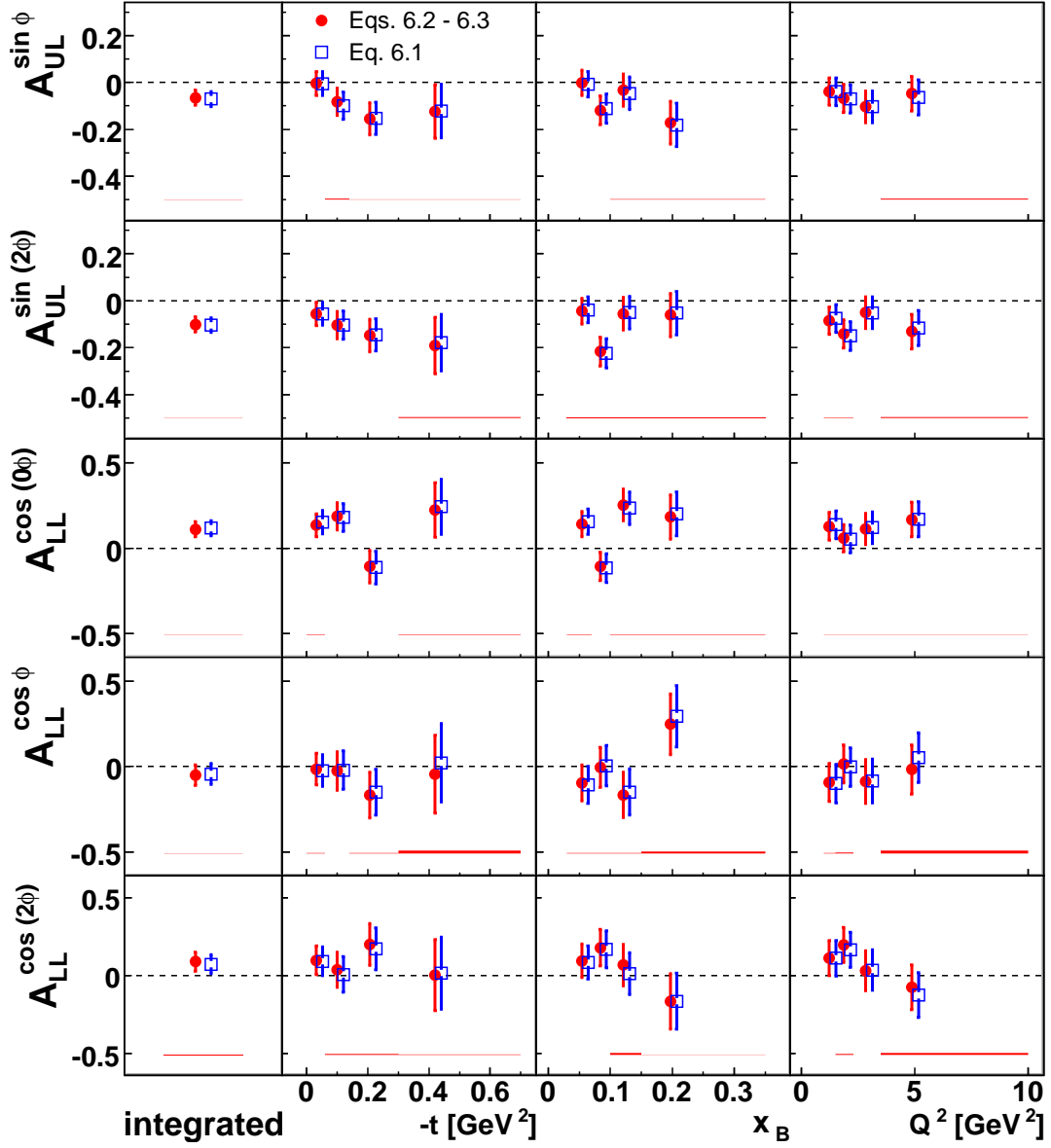**Figure 6.2:** The $A_{\mathrm{UL}}^{\sin(n\phi)}$ and $A_{\mathrm{LL}}^{\cos(n\phi)}$ amplitudes extracted from the exclusive data sample using the original (Eq. 6.1) and shifted M_{X}^2 regions (Eqs. 6.2 and 6.3) determined for this analysis. The bands show the corresponding contribution to the systematic uncertainty which is evaluated as one quarter of the difference in each $-t$, x_{B} and Q^2 bin.

6.2 Correcting for Background Contributions

The extracted asymmetry amplitudes presented here do not arise solely from the elastic BH and DVCS processes. Instead, they also contain contributions from several background processes which contaminate the analysed data sample. These contributions arise from resonance production, semi-inclusive DIS processes and from exclusive π^0 production.

If all N background processes and corresponding asymmetries A_i are known, corrections can be made to the extracted amplitudes to determine the desired BH/DVCS contribution, *i.e.*

$$A_{\mathrm{BH/DVCS}} = \frac{1}{f_{\mathrm{BH/DVCS}}} \left(A_{\mathrm{measured}} - \sum_i^N f_i \, A_i \right), \qquad (6.4)$$

where f_i is the relative fractional contribution from background process i.

Based on a MC simulation using a parametrisation of the form factor for the resonance region from Ref. [106] and the individual cross sections for the single-meson decay channels *e.g.* $\Delta^+ \to p\pi^0$ calculated using the MAID2000 program [107], each background process is identified using the following selection criteria:

- BH/DVCS: **g1MEvent.XTrue** $= 1$,

- Associated BH: **g1MEvent.XTrue** < 1 and **g1MEvent.W2True** < 4,

- Semi-inclusive π^0: **g1MEvent.XTrue** < 1 and **g1MEvent.W2True** > 4,

where **XTrue** and **W2True** represent the generated MC values of x and W^2 respectively. The corresponding fractional contribution f_{process} of a particular process is determined as

$$f_{\mathrm{process}} = \frac{\sum\limits_i^{N_{\mathrm{process}}} w_i}{\sum\limits_i^N w_i}, \qquad (6.5)$$

where w_i is the MC event weight of an exclusive event i, passing all DVCS-candidate requirements and $N_{\mathrm{process}} \subset N$. Values of these fractions are presented in Table 6.2 and Fig. 6.3 for each kinematic bin with statistical uncertainties calculated from error propagation, determined using the findings of Ref. [108] that a MC-weighted quantity $\sigma = \sum_i^N w_i$ has an uncertainty $d\sigma = \sqrt{\sum_i^N w_i^2}$.

The largest of these contributions arises from resonance production (12.9% on average and ranging from 5.6% to 33.6% over the range in t) where an excited state of the proton *i.e.* a

Kinematic Bin	Elastic BH	Resonant	Semi-Inc. DIS	Excl. π^0
Overall	$84.0 \pm 0.0\%$	$12.9 \pm 0.0\%$	$3.1 \pm 0.1\%$	$0.4 \pm 0.2\%$
$-t \leq 0.06$	$92.5 \pm 0.0\%$	$5.6 \pm 0.0\%$	$1.9 \pm 0.3\%$	$0.5 \pm 0.4\%$
$0.06 < -t \leq 0.14$	$83.3 \pm 0.0\%$	$12.6 \pm 0.0\%$	$4.0 \pm 0.3\%$	$0.7 \pm 0.6\%$
$0.14 < -t \leq 0.30$	$74.3 \pm 0.0\%$	$21.6 \pm 0.0\%$	$4.1 \pm 0.3\%$	$0.4 \pm 0.6\%$
$0.30 < -t \leq 0.70$	$62.1 \pm 0.0\%$	$33.6 \pm 0.0\%$	$4.1 \pm 0.3\%$	$0.2 \pm 0.9\%$
$0.03 < x_{\mathrm{B}} \leq 0.07$	$87.4 \pm 0.0\%$	$11.3 \pm 0.0\%$	$1.1 \pm 0.2\%$	$0.2 \pm 0.3\%$
$0.07 < x_{\mathrm{B}} \leq 0.10$	$84.5 \pm 0.0\%$	$12.3 \pm 0.0\%$	$3.4 \pm 0.4\%$	$0.7 \pm 0.5\%$
$0.10 < x_{\mathrm{B}} \leq 0.15$	$82.0 \pm 0.0\%$	$14.1 \pm 0.0\%$	$3.8 \pm 0.4\%$	$0.6 \pm 0.7\%$
$0.15 < x_{\mathrm{B}} \leq 0.35$	$75.3 \pm 0.0\%$	$16.3 \pm 0.0\%$	$8.0 \pm 0.5\%$	$0.4 \pm 1.0\%$
$1.0 < Q^2 \leq 1.5$	$86.3 \pm 0.0\%$	$10.4 \pm 0.0\%$	$3.4 \pm 0.2\%$	$0.6 \pm 0.6\%$
$1.5 < Q^2 \leq 2.3$	$84.2 \pm 0.0\%$	$12.2 \pm 0.0\%$	$2.4 \pm 0.2\%$	$0.7 \pm 0.7\%$
$2.3 < Q^2 \leq 3.5$	$82.2 \pm 0.0\%$	$14.0 \pm 0.0\%$	$3.7 \pm 0.3\%$	$0.3 \pm 0.5\%$
$3.5 < Q^2 \leq 10.0$	$80.1 \pm 0.0\%$	$16.3 \pm 0.0\%$	$3.3 \pm 0.4\%$	$0.1 \pm 0.5\%$

Table 6.2: Fractional contributions of the processes present in the exclusive region for each $-t$, x_{B}, and Q^2 bin. These have been determined from MC simulations and the presented errors are purely statistical and depend on the number of generated MC events available.

resonance, is present in the final state, *e.g.* $\gamma^* p \to \Delta^+ \gamma$, where the Δ^+ resonance decays into $p\pi^0$ $(n\pi^+)$ with a branching ratio of $\frac{2}{3}$ $\left(\frac{1}{3}\right)$. These events cannot be distinguished from BH/DVCS events without the detection of all final state particles due to the limited M_{X}^2 resolution.

The contribution from semi-inclusive DIS processes on the other hand (3.1% on average, ranging from 1.1% to 8.0% over the range in x_{B}), can be corrected by performing a 'two-photon analysis' to extract the corresponding asymmetries from the semi-inclusive π^0 data sample.

Studies based on HERMES MC simulations have shown that π^0 production accounts for approximately 80% of these semi-inclusive DIS events, where a neutral meson is produced and decays into two photons [65]. The remainder of this contribution is mainly from η^0 decay ($\sim$15%). It has also been shown using models in Refs. [49,109] that the contribution from exclusive π^0 production is less than 0.7% in each kinematic bin. This is supported by a data search at HERMES [110]. Due to the limited statistics available in this analysis,
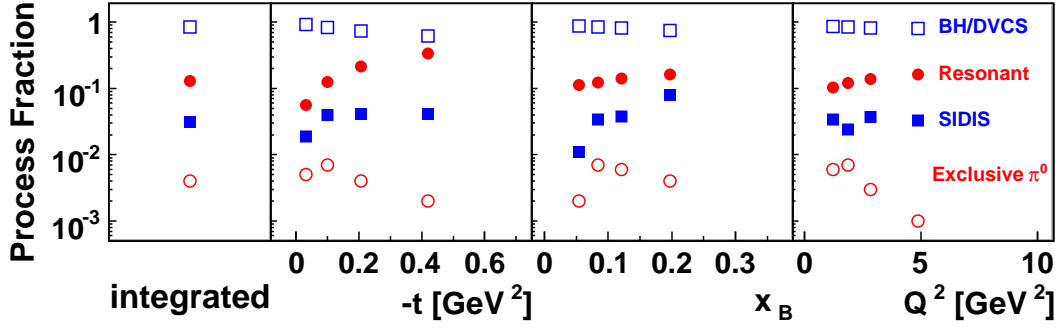
Figure 6.3: Average fractional contributions of each process present in the exclusive data sample, integrated over all kinematics and as a function of $-t$, x_{B}, and Q^2. Shown are contributions from the BH/DVCS, resonance production, semi-inclusive DIS (SIDIS) and exclusive π^0 processes.

this asymmetry cannot be extracted from the experimental data. As such, a value of $0 \pm \frac{2}{\sqrt{12}}$ is chosen corresponding to one standard deviation from a uniform distribution in the range [-1,1].

The background-corrected asymmetry, representing the asymmetry from the combined elastic BH/DVCS and resonant processes, can then be determined in each kinematic bin as

$$A_{\mathrm{corrected}} = \frac{A_{\mathrm{measured}} - f_{\mathrm{sidis}} A_{\mathrm{sidis}} - f_{\mathrm{excl}} A_{\mathrm{excl}}}{1 - f_{\mathrm{sidis}} - f_{\mathrm{excl}}} \,. \tag{6.6}$$

where f_{sidis} (f_{excl}) and A_{sidis} (A_{excl}) represent the fraction and asymmetry amplitude of the semi-inclusive DIS (exclusive) π^0 process respectively.

Correcting for the π^0 Background Contributions

The semi-inclusive DIS process is dominated by events in which the trackless cluster(s) detected in the calorimeter is (are) produced by decay photons from a neutral pion. This process is represented as

$$\gamma^* p \to p \, \pi^0 \to p \, \gamma(\mathbf{q_1'}) \, \gamma(\mathbf{q_2'}) \,, \tag{6.7}$$

where $\mathbf{q_1'}$ and $\mathbf{q_2'}$ represent the four-momenta of the two decay photons.

On average, 3.1% of events in the exclusive region arise from this process and are mistaken for elastic BH/DVCS events. If the interaction positions of the two photons are too close together for the calorimeter to resolve, then only one trackless cluster will be reconstructed with the combined energy deposition of the two photons. The single cluster can also arise from a single decay photon with the second photon passing outwith the acceptance of the spectrometer.

In the first of these cases, the resultant asymmetry $A_{\text{sidis}}^{\gamma\gamma}$ is a direct measure of the neutral pion asymmetry $A_{\text{sidis}}^{\pi^0}$. In the second instance, the asymmetry $A_{\text{sidis}}^{\gamma}$ is not equal to $A_{\text{sidis}}^{\pi^0}$. However, studies have shown that the ratio of both extracted asymmetries is consistent with unity [65]. It was shown that $A_{\text{sidis}}^{\gamma}/A_{\text{sidis}}^{\pi^0} = 1.05 \pm 0.15$.

To correct for the semi-inclusive background asymmetry contribution, the asymmetry from the dominant π^0 process is extracted. It is assumed that the η^0 contribution to the overall semi-inclusive background asymmetry does not affect the π^0 asymmetry within statistical uncertainty. The event selection for the semi-inclusive π^0 data sample requires a DIS event as defined previously in Section 5.1, but with two trackless clusters reconstructed in the calorimeter. The same preshower energy and photon fiducial volume criteria used in the selection of a DVCS-candidate event are required for both of these photons. However, in addition, the following requirements are imposed on the photons in the lab frame:

- $E_1 > 5\,\text{GeV}$, *i.e.* the energy deposited in the calorimeter by the highest energy *i.e.* the 'leading' photon has to be greater than $5\,\text{GeV}$ as shown in Ref. [65].

- $E_2 > 1\,\text{GeV}$, *i.e.* the lowest energy photon must deposit at least $1\,\text{GeV}$ in the calorimeter.

There are two additional criteria that must be fulfilled. The energy fraction transferred from the virtual photon to the pion, denoted z_{π^0}, must be sufficiently large, and the invariant mass of the two-photon system is required to be close to the π^0 mass. These kinematics are defined as

$$z_{\pi^0} \quad \overset{\text{lab}}{=} \quad \frac{E_1 + E_2}{\nu}, \tag{6.8}$$

$$M_{\gamma\gamma}^2 \equiv (\mathbf{q'_1} + \mathbf{q'_2})^2 \quad \overset{\text{lab}}{=} \quad 2\,E_1 E_2 \left(1 - \cos\theta_{\gamma\gamma}\right), \tag{6.9}$$

where

$$\theta_{\gamma\gamma} = \cos^{-1} \left| \frac{\vec{q'_1} \cdot \vec{q'_2}}{\left|\vec{q'_1}\right| \left|\vec{q'_2}\right|} \right|, \tag{6.10}$$

is the polar angle between the two decay photons calculated from their positional three-vectors. The 'semi-inclusive' π^0 data sample is selected by imposing the following requirements on these kinematic variables:

- $z_{\pi^0} > 0.8$ introduces a check for a reasonable level of exclusivity, allowing for the poor photon energy resolution of the calorimeter.
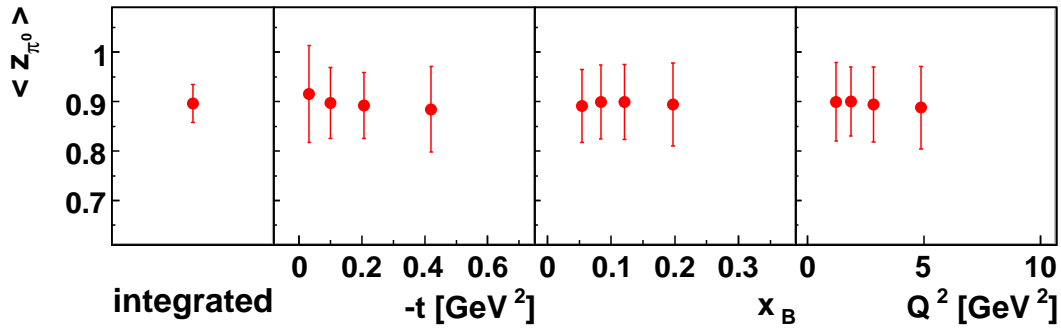
Figure 6.4: Values of the average energy fraction transferred to the neutral pion $\langle z_{\pi^0} \rangle$ from the virtual photon in each $-t$, x_B, and Q^2 bin.

- $0.10\,\mathrm{GeV} < M_{\gamma\gamma} < 0.17\,\mathrm{GeV}$ ensures the selected data sample has an invariant mass which corresponds to that of the neutral pion. These limits correspond to 2.5σ from the mean of the distribution.

As all final state particles are not detected, this sample may also contain exclusive π^0 events. However, this contribution is expected to be negligible.

The average energy transfer $\langle z_{\pi^0} \rangle$ to the pion, is shown in Fig. 6.4 to be large across all plotted kinematics. For the semi-inclusive π^0 analysis, the $M_{\gamma\gamma}$ criteria applied around the neutral pion mass, replaces the standard M_X^2 requirement. When this is also applied to the semi-inclusive π^0 data sample, the statistics drop such that it is no longer possible to extract an asymmetry for the exclusive π^0 process.

The resulting invariant mass $M_{\gamma\gamma}$ distribution of the two-photon system is presented in Fig. 6.5 with all selection criteria applied with the exception of the $M_{\gamma\gamma}$ constraint which is highlighted. A Gaussian fit has been performed within this region and the fit parameters shown indicate the mean is within one standard deviation of the neutral pion mass of $0.135\,\mathrm{GeV}$ [111].

The experimental kinematics are calculated by one of two different methods: using the four-momentum of the leading photon as $\mathbf{q}'$, or by using the four-momentum of the neutral pion itself, where for the latter case, $\mathbf{q}'$ is calculated as the vector sum of the four-momenta of the two detected photons. A comparison between these two approaches, shown in Fig. 6.6, shows that both sets of semi-inclusive π^0 asymmetry amplitudes are consistent, confirming the findings in Ref. [65]. For the correction which follows, the kinematic variables are determined using the four-momentum of the π^0.

The kinematic dependences of the semi-inclusive π^0 asymmetry amplitudes are presented
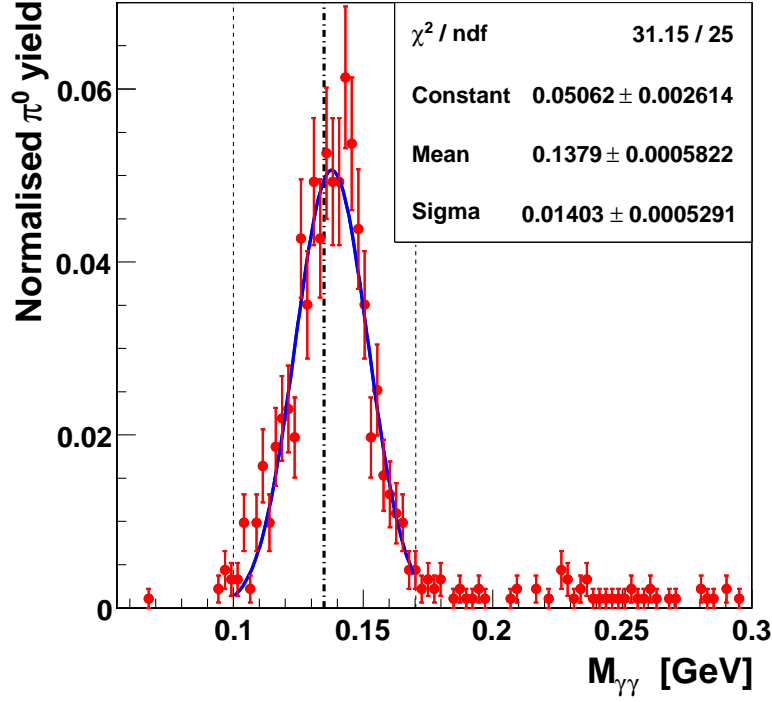
Figure 6.5: Reconstructed invariant mass of the semi-inclusive two-photon system. A Gaussian fit (solid line) is applied within the $0.10\,\mathrm{GeV} < M_{\gamma\gamma} < 0.17\,\mathrm{GeV}$ region (dotted lines). The mean of this fit agrees well with $M_{\pi^0} = 0.135\,\mathrm{GeV}$ [111] (dot-dashed line).

in Fig. 6.7 alongside the corresponding amplitudes extracted from the exclusive data sample. All background asymmetry amplitudes are consistent with zero with the exception of the $A_{\mathrm{UL},\pi^0}^{\sin\phi} = 0.161 \pm 0.064$. However, with the limited statistics available, it is difficult to comment on any dependence on $-t$, x_{B}, or Q^2.

For what follows, the semi-inclusive and exclusive π^0 processes will be labelled j and k for compactness. By considering Eq. 6.6 and propagating the statistical uncertainties from the two background asymmetries A_{sidis} and A_{excl}, their corresponding fractional contributions f_{sidis} and f_{excl}, and the extracted asymmetry from the exclusive data set A_{measured}, the revised statistical uncertainty δ_{stat} of the background-corrected amplitudes can be calculated as

$$\delta_{\mathrm{stat}} = \sqrt{(\delta A_{\mathrm{measured}})^2 + (\delta f_j)^2 + (\delta f_k)^2 + (\delta A_j)^2 + (\delta A_k)^2}\,, \qquad (6.11)$$
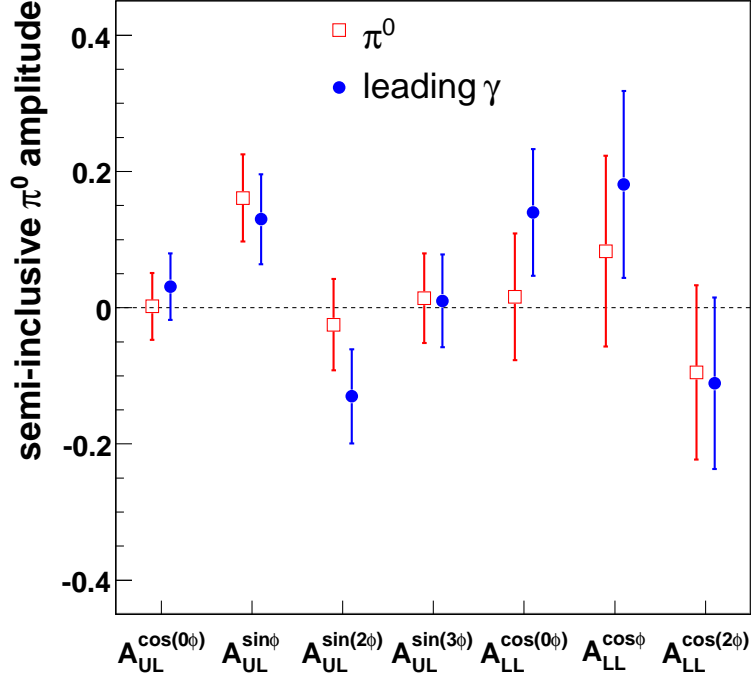
Figure 6.6: Comparison of the integrated asymmetry amplitudes extracted from the semi-inclusive π^0 data sample using kinematics calculated from either the four-momentum of the leading photon or from the four-momentum of the neutral pion. It is shown that both sets of amplitudes are consistent.

where

$$\delta f_{j(k)} = df_{j(k)} \cdot \frac{A_{\text{measured}} - A_{j(k)} - f_{k(j)} A_{k(j)} + f_{k(j)} A_{j(k)}}{(1 - f_j - f_k)^2}, \qquad (6.12)$$

$$\delta A_{j(k)} = dA_{j(k)} \cdot \frac{-f_{j(k)}}{1 - f_j - f_k}, \qquad (6.13)$$

$$\delta A_{\text{measured}} = dA_{\text{measured}} \cdot \frac{1}{1 - f_j - f_k}. \qquad (6.14)$$

Half of the effect the correction from Eq. 6.6 has on the extracted amplitudes is assigned as a systematic uncertainty, *i.e.*

$$\delta_{\text{Bg}} = \frac{|A_{\text{corrected}} - A_{\text{measured}}|}{2}. \qquad (6.15)$$

Figure 6.8 presents the kinematic dependences of the physics-motivated $\mathcal{A}_{\text{UL}}$ and $\mathcal{A}_{\text{LL}}$ amplitudes before and after applying the π^0 background correction from Eq. 6.6. The overall effect is observed to be small across the kinematic range, with the largest correction observed in low statistic bins, *e.g.* the final x_{B} bin which is also subject to the largest semi-inclusive π^0 background contribution. The systematic uncertainty assigned as a result of

this correction is also shown.

The corrected amplitudes shown in Fig. 6.8 thus arise from a combination of the elastic BH/DVCS and resonant processes only.
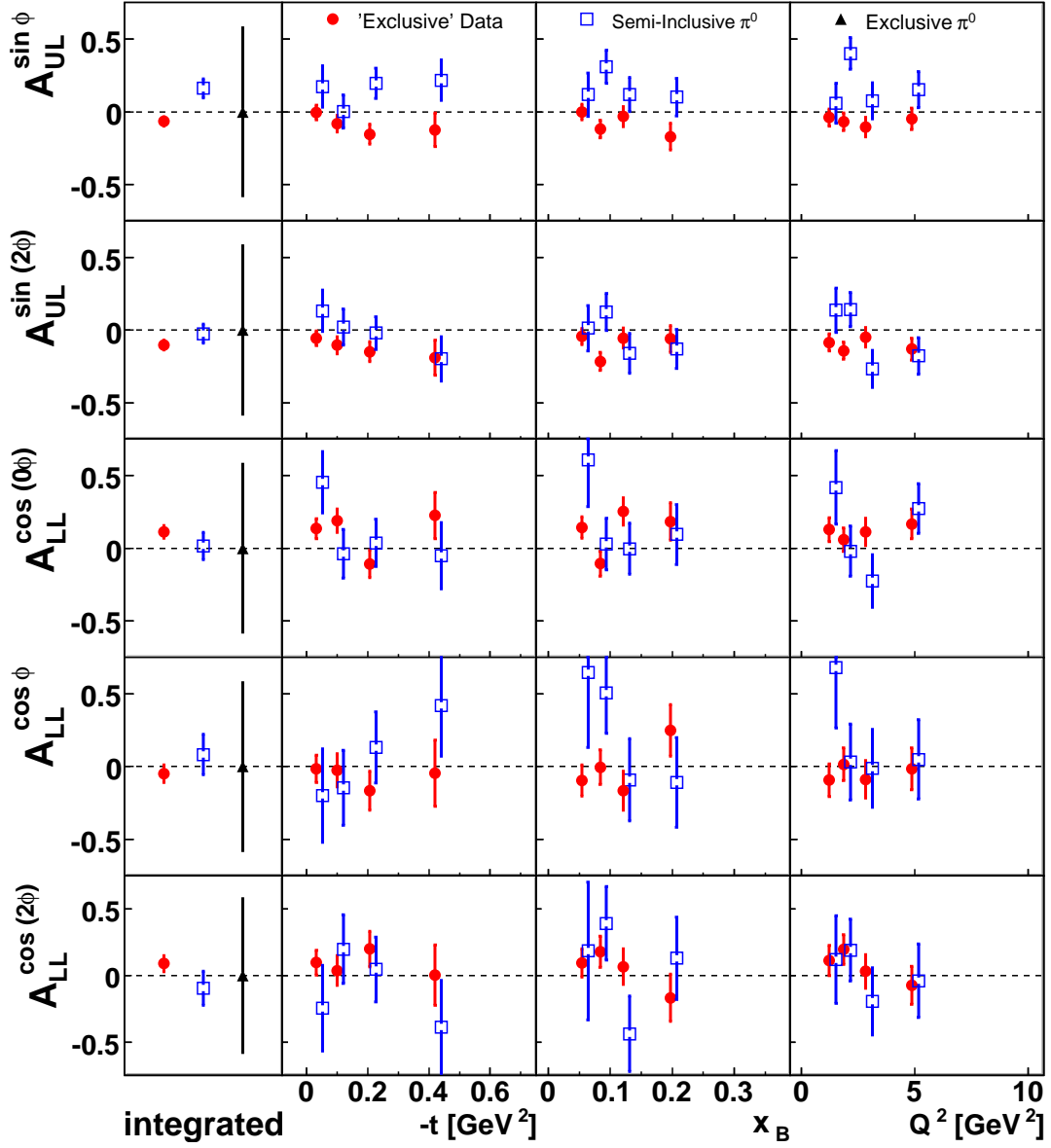
Figure 6.7: Comparison between the uncorrected $A_{\mathrm{UL}}^{\sin(n\phi)}$ and $A_{\mathrm{LL}}^{\cos(n\phi)}$ amplitudes (filled circles) extracted from the exclusive data sample and those extracted from the semi-inclusive π^0 sample (open squares) for each $-t$, x_{B}, and Q^2 bin. The black triangles represent the A_{excl} amplitudes explained in the text. Only the $A_{\mathrm{UL},\pi^0}^{\sin\phi}$ amplitude is observed to be non-zero.
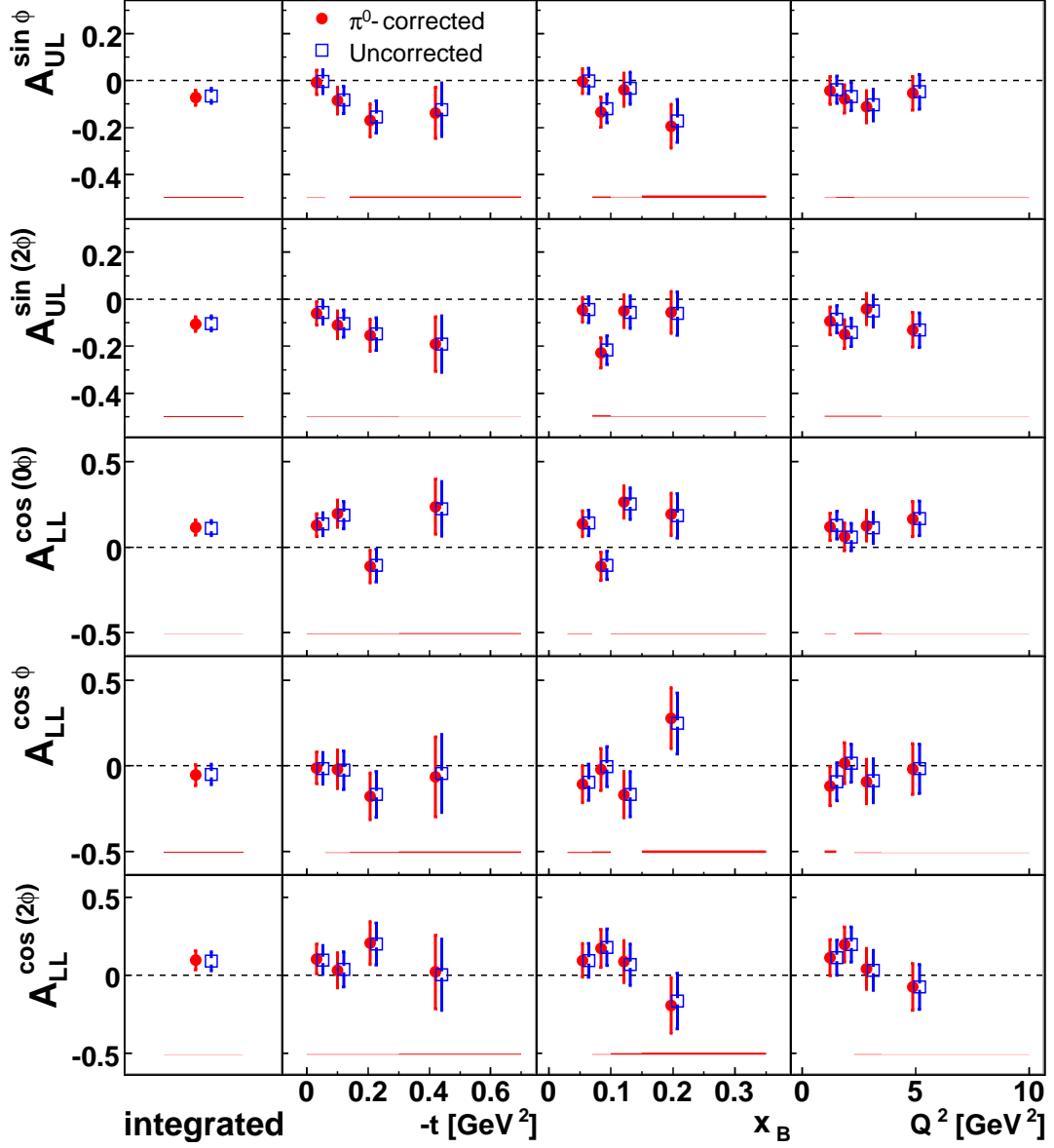
Figure 6.8: Comparison between the uncorrected (open squares) and π^0 background-corrected (filled circles) $A_{\mathrm{UL}}^{\sin(n\phi)}$ and $A_{\mathrm{LL}}^{\cos(n\phi)}$ amplitudes for each $-t$, x_{B}, and Q^2 bin. Small corrections are observed for the $A_{\mathrm{UL}}^{\sin\phi}$ amplitude and in kinematic bins which contain a higher fraction of semi-inclusive events. The bands show the corresponding systematic uncertainty contribution calculated from Eq. 6.15.

6.3   Four-in-One Systematic Uncertainty

The remaining sources of systematic uncertainty arise from detector acceptance and mis-alignment, smearing and finite bin-width effects in $-t$, x_B, and Q^2. These effects are described as:

- **Acceptance of the spectrometer** - The spectrometer (described in Section 4.3) does not provide 4π angular coverage. The effect of the limited acceptance must be accounted for in order to present a model comparison.

- **Misalignment of the detector setup** - Uncertainties in the alignment of the various subdetectors with respect to each other (internal misalignment) or with respect to the beam-line (external misalignment). These slight shifts and/or rotations may significantly affect the extracted amplitudes.

- **Smearing effects** - These arise from the limited resolution of the calorimeter. The 'smeared' signal results in an uncertainty in determining the interaction position of a particle with the calorimeter. This can have an adverse effect on the reconstructed kinematics and consequently introduces an uncertainty in the extracted asymmetry amplitudes.

- **Finite bin-width** - Although the EML method provides an unbinned fit in ϕ, all amplitudes presented are plotted in four bins of $-t$, x_B, and Q^2 at the average kinematics of each bin. Effects introduced from events smearing into an adjacent bin are taken into account.

Before the publication of Ref [22], each of these effects were accounted for separately and their corresponding uncertainties were combined in quadrature. However, subsequent studies have shown that the best estimate of these effects is to account for them as one combined uncertainty. This correlated '4-in-1' systematic uncertainty is now a standard part of the HERMES DVCS analysis process.

For this study, MC containing these four detrimental effects was generated for each beam and target polarisation state from 5 GPD-parametrisations based on the model from Ref. [57]. These models describe the relevant CFFs at leading-quark-twist level only and to leading-order in α_s. Table 6.3 outlines the different parameters implemented in each of these models. Here, a factorised t-ansatz is used and $b = b_{\text{valence}} = b_{\text{sea}}$.

Model	Factorised t-ansatz	Skewness	b-parameter	D Term
1	$\checkmark$	x	9	x
2	$\checkmark$	$\checkmark$	1	x
3	$\checkmark$	$\checkmark$	3	x
4	$\checkmark$	$\checkmark$	1	$\checkmark$
5	$\checkmark$	$\checkmark$	3	$\checkmark$

Table 6.3: Properties of the 5 GPD model parametrisations implemented in the Monte Carlo simulation.

By analysing the elastic BH and DVCS events passing all previous exclusive requirements from this MC production, the 'reconstructed' asymmetry amplitudes can be extracted for each model using an EML routine based on Eq. 5.39. These amplitudes were extracted in each kinematic bin as a function of the model-specific MC event weight w by minimising the fit function

$$-\ln \mathcal{L}(\theta) = -\sum_i^N w^2 \ln\left[1 + P_{\mathrm{L}}\mathcal{A}_{\mathrm{UL}}(\mathbf{x}_i;\theta) + P_\ell P_{\mathrm{L}}\mathcal{A}_{\mathrm{LL}}(\mathbf{x}_i;\theta)\right] + \mathcal{N}(\theta, w^2). \qquad (6.16)$$

The systematic uncertainty arising from the ith model is estimated as

$$\delta_i = \left|A_{\mathrm{generated}} - A_{\mathrm{reconstructed}}\right|, \qquad (6.17)$$

where the 'generated' asymmetry amplitudes are calculated from the corresponding GPD-parametrisation at the same average kinematics of each bin. As these have been calculated directly from the theoretical predictions they are free from any influence of the detector or finite binning effects. Figure 6.9 shows the generated and reconstructed amplitudes from one of the parametrisations (Model 1). The magnitude of the difference between these in each kinematic bin is also presented.

The predictions of a small $A_{\mathrm{UL}}^{\sin(2\phi)}$ amplitude, consistent with zero, by the GPD parametrisations have been artificially scaled to agree with the data to provide a more accurate estimation of this systematic uncertainty.

The combined systematic uncertainty from the 5 parametrisations is therefore calculated as

$$\delta_{\mathrm{4in1}} = \sqrt{\frac{1}{5}\sum_i^5 \delta_i^2}. \qquad (6.18)$$

This final 4-in-1 systematic uncertainty is presented in Fig. 6.10 alongside those arising from each of the five model parametrisations. All five models are shown to provide similar

Amplitude	$A \pm \delta_{\text{stat}} \pm \delta_{\text{syst}}$	$\delta_{M_X^2}$	δ_{Bg}	δ_{4in1}
$A_{\text{UL}}^{\sin\phi}$	$-0.073 \pm 0.032 \pm 0.007$	0.002	0.006	0.002
$A_{\text{UL}}^{\sin(2\phi)}$	$-0.106 \pm 0.032 \pm 0.008$	0.000	0.002	0.007
$A_{\text{UL}}^{\sin(3\phi)}$	$0.015 \pm 0.032 \pm 0.009$	0.000	0.001	0.009
$A_{\text{LL}}^{\cos(0\phi)}$	$0.115 \pm 0.044 \pm 0.004$	0.001	0.003	0.003
$A_{\text{LL}}^{\cos\phi}$	$-0.054 \pm 0.062 \pm 0.029$	0.002	0.003	0.028
$A_{\text{LL}}^{\cos(2\phi)}$	$0.095 \pm 0.062 \pm 0.007$	0.004	0.003	0.004

Table 6.4: Integrated values of the asymmetry amplitudes extracted in this analysis with the corresponding statistical and systematic uncertainties. For the latter, the different contributions outlined in the text are also presented. Not included are scale uncertainties of 4.2% (5.3%) arising from the target (beam and target) polarisation measurements which affect the $A_{\text{UL}}^{\sin(n\phi)}$ $\left(A_{\text{LL}}^{\cos(n\phi)} \right)$ amplitudes.

estimations of these four systematic effects.

The final systematic uncertainty affecting each extracted amplitude can then be determined in each kinematic bin as

$$\delta_{\text{syst}} = \sqrt{\delta_{M_X^2}^2 + \delta_{\text{Bg}}^2 + \delta_{4in1}^2} \,. \qquad (6.19)$$

The contributions from each uncertainty are shown in Table 6.4.
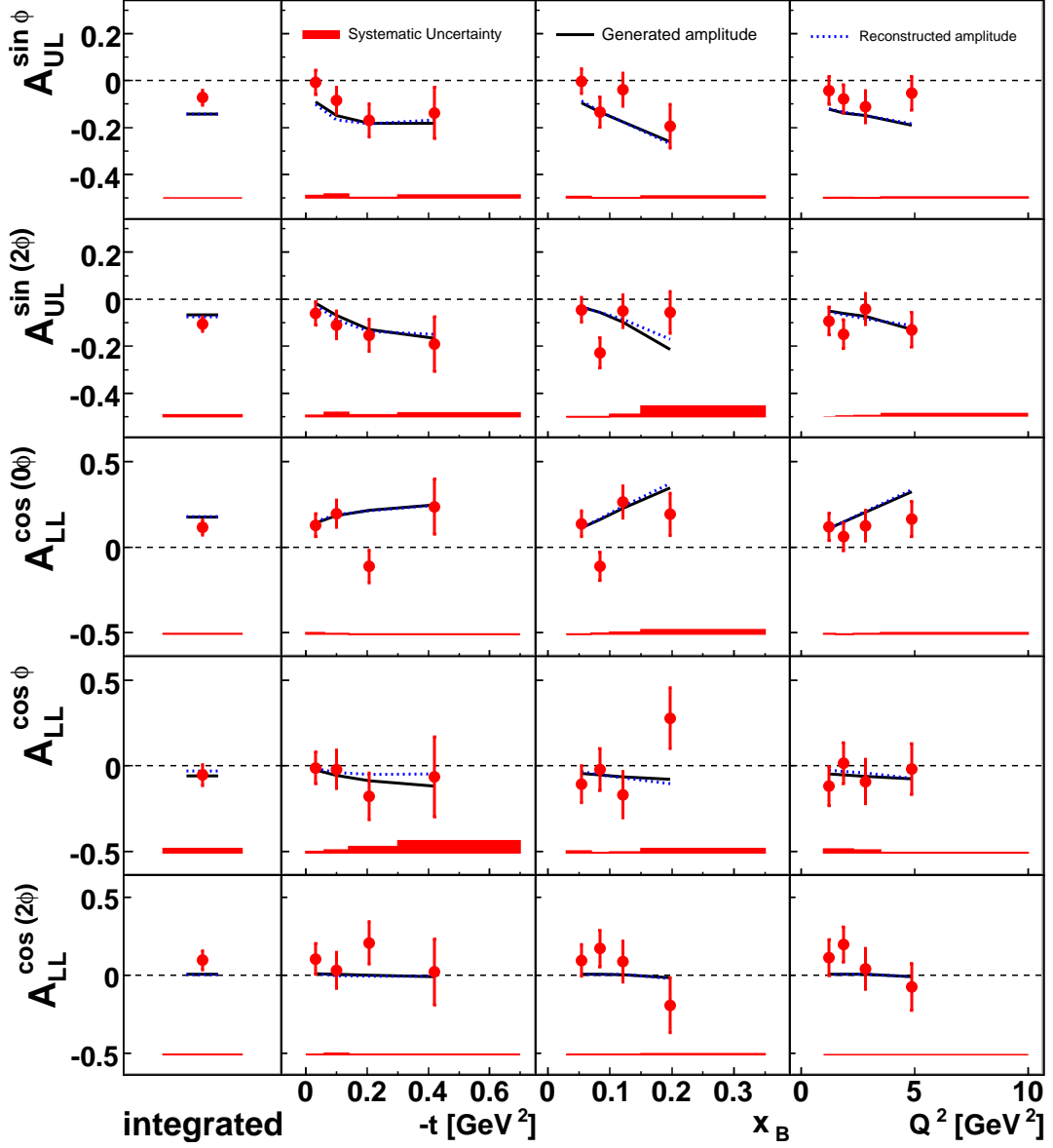
Figure 6.9: Comparison of the reconstructed (dotted line) and generated (solid line) $A_{\mathrm{UL}}^{\sin(n\phi)}$ and $A_{\mathrm{LL}}^{\cos(n\phi)}$
amplitudes from one of the GPD-parametrisations (Model 1) included in the MC. These are
compared to the corrected amplitudes, extracted from data for each $-t$, x_{B}, and Q^2 bin. The
bands represent the 4-in-1 systematic uncertainty arising from this model, determined using
Eq. 6.17.
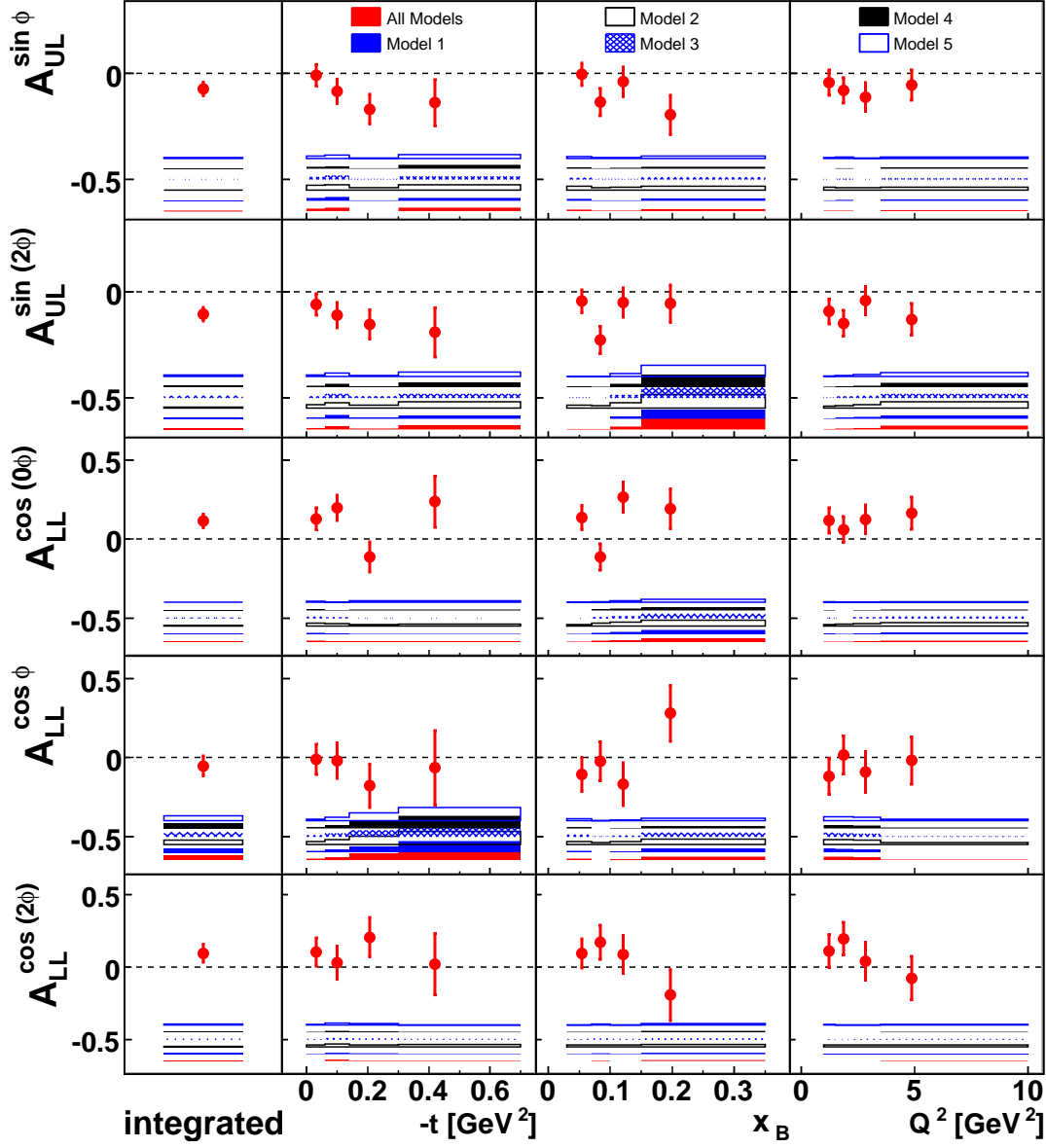
Figure 6.10: Comparison of the $A_{\mathrm{UL}}^{\sin(n\phi)}$ and $A_{\mathrm{LL}}^{\cos(n\phi)}$ extracted amplitudes and the 4-in-1 systematic uncertainty for each model in bins of $-t$, x_{B}, and Q^2. The bottom band represents the final 4-in-1 systematic uncertainty determined using Eq. 6.18.

Chapter 7

Final Results

The final asymmetry amplitudes are presented in Figs. 7.1 and 7.2 integrated over all kinematics in the HERMES acceptance, *i.e.* extracted in a single bin, and as a function of $-t$, $x_{\rm B}$, and Q^2 . Tables containing the asymmetry amplitude values and average kinematics of each bin are presented in Appendix C. The amplitudes presented have been corrected for semi-inclusive and exclusive π^0 background contributions and thus arise from a combination of BH, DVCS and resonant processes only. The effect that the latter have on the extracted amplitudes is not presently known. The results are presented alongside theoretical predictions from the GPD model parametrisation outlined in Section 2.6. These "VGG Regge" [49] predictions are calculated solely from the BH/DVCS process using the VGG computer code [48]. The input parameters to the model are given in Appendix D. Therefore, the average fractional contributions from the resonant process, calculated from MC simulation, are presented in the bottom panels to provide an indication of the potential differences between the data and the model calculations.

Figure 7.1 shows the $A_{\rm UL}^{\sin(n\phi)}$ amplitudes of the longitudinally polarised target-spin asymmetry $\mathcal{A}_{\rm UL}$. The $A_{\rm UL}^{\sin\phi}$ amplitude appears at leading-twist level via the interference term $\mathcal{I}$. It is shown to be non-zero when integrated over the kinematic range with a value of $-0.073 \pm 0.032({\rm stat}) \pm 0.007({\rm syst})$. The extracted amplitudes increase with increasing $-t$, $x_{\rm B}$, and Q^2, in agreement with the predicted trend. However, this may arise from the unknown asymmetry from resonance states which contaminate the data sample more at higher kinematics. As a result of this and from the statistical precision, no strong conclusion can be made regarding kinematic dependences.

In comparison, the twist–3 amplitude $A_{\rm UL}^{\sin(2\phi)}$ is expected to have opposite sign and suppression by a factor of $\frac{1}{Q^2}$. However this is not observed. Instead, the amplitude has an
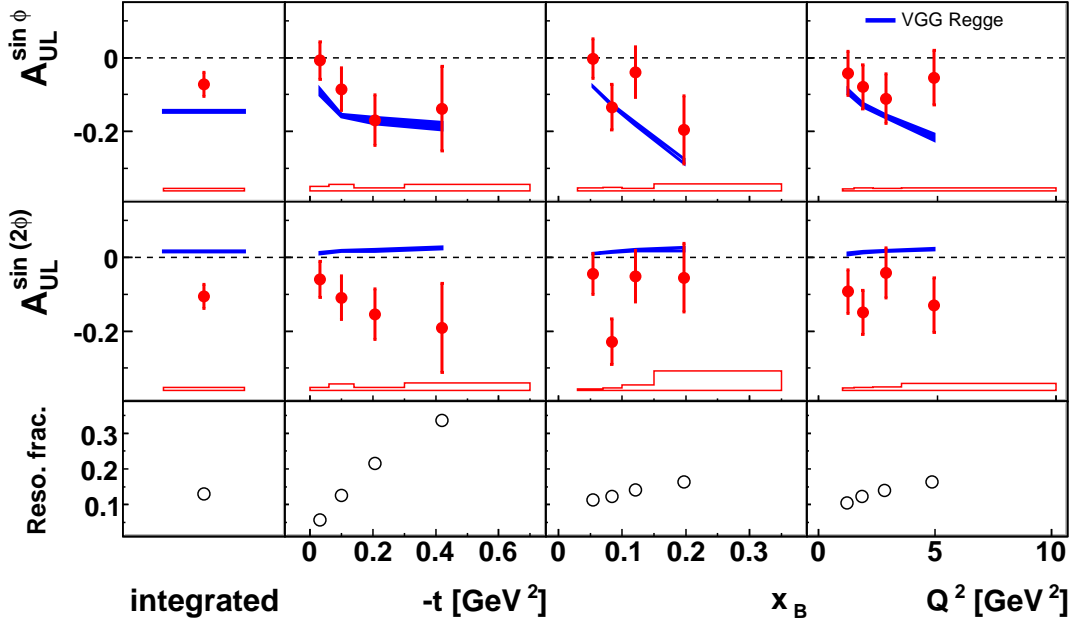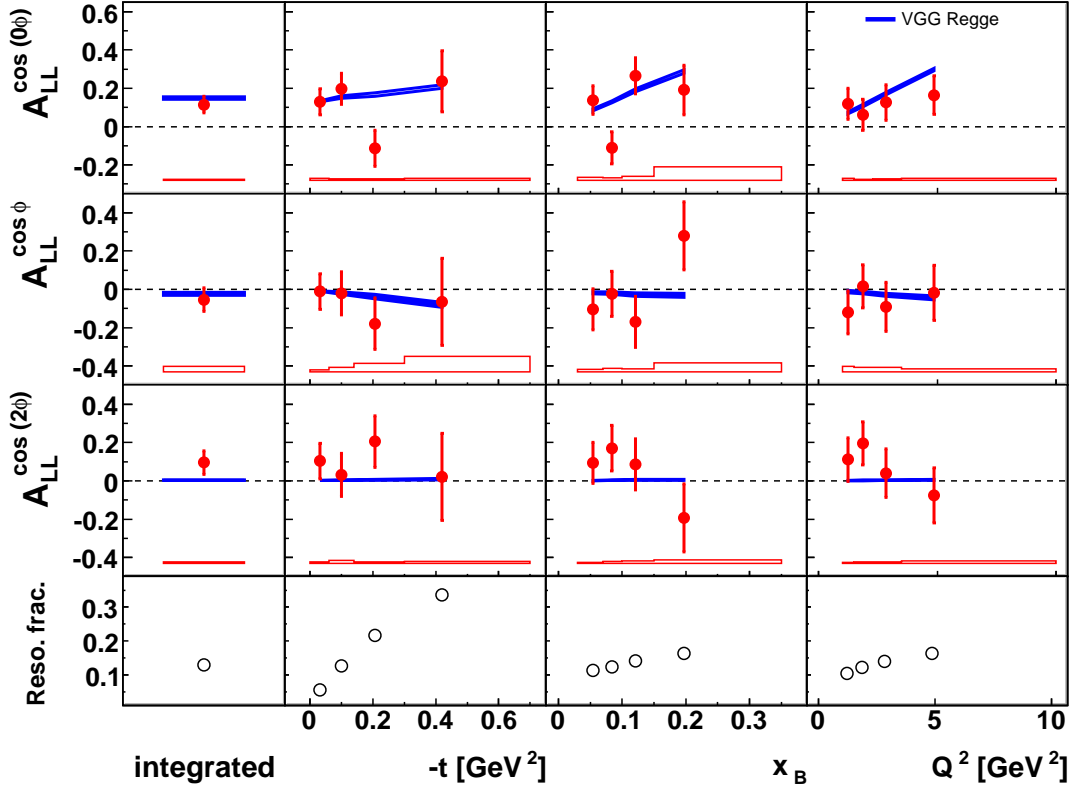
Figure 7.1: $A_{\mathrm{UL}}^{\sin(n\phi)}$ amplitudes of the longitudinally polarised target-spin asymmetry sensitive to the interference and squared-DVCS terms, from longitudinally polarised proton data, as a function of $-t$, x_{B}, and Q^2. The error bars and open bands show the statistical and systematic uncertainties respectively. There is an additional 4.2% scale uncertainty arising from the measurement of the target polarisation. The solid bands represent the theoretical predictions from a GPD model [49] ("VGG Regge"). The fractional contributions from resonance production ("Reso. frac.") are estimated from MC simulation and shown in the bottom panel.

unexpectedly large value of $-0.106 \pm 0.032 \pm 0.008$ with a similar t-dependence to the $A_{\mathrm{UL}}^{\sin\phi}$ amplitude. There is currently no theoretical explanation for the difference between the extracted values and the model prediction. However, the amplitude does agree with the theoretical calculation of this amplitude within uncertainty in all but the second x_{B} bin which has a large negative amplitude. Rebinning of this x_{B} region into multiple smaller bins revealed no additional explanation of this unexpectedly large amplitude.

Figure 7.2 shows the extracted $A_{\mathrm{LL}}^{\cos(n\phi)}$ amplitudes from the double-spin asymmetry $\mathcal{A}_{\mathrm{LL}}$. The pure twist–2 $A_{\mathrm{LL}}^{\cos(0\phi)}$ amplitude appears at leading-twist from both the squared-DVCS $|\tau_{\mathrm{DVCS}}|^2$ and $\mathcal{I}$ terms with an additional, dominating contribution from the Fourier coefficient $c_{0,\mathrm{LP}}^{\mathrm{BH}}$ appearing in the squared-BH term $|\tau_{\mathrm{BH}}|^2$. It is non-zero with an integrated value of $0.115 \pm 0.044 \pm 0.004$ and is in broad agreement with theoretical predictions across the kinematic range. The amplitude shows no dependence on $-t$, x_{B}, or Q^2.

As predicted, the leading-twist $A_{\mathrm{LL}}^{\cos\phi}$ amplitude is consistent with zero with an integrated

Figure 7.2: $A_{\text{LL}}^{\cos(n\phi)}$ amplitudes of the double-spin asymmetry sensitive to the interference and squared-DVCS and BH terms, from longitudinally polarised proton data, as a function of $-t$, x_{B}, and Q^2. The error bars and open bands show the statistical and systematic uncertainties respectively. There is an additional 5.3% scale uncertainty arising from the measurement of the beam and target polarisations. The solid bands represent the theoretical predictions from a GPD-model [49] ("VGG Regge"). The fractional contributions ("Reso. frac.") from resonance production are estimated from MC simulation and shown in the bottom panel.

value of $-0.054 \pm 0.062 \pm 0.029$. It also receives contributions from all three terms in the squared scattering amplitude with a dominant contribution from $c_{1,\text{LP}}^{\text{BH}}$. It does not exhibit any dependence on $-t$, x_{B}, or Q^2 and agrees with the prediction of a small, negative amplitude. The pure twist–3 amplitude $A_{\text{LL}}^{\cos(2\phi)} = 0.095 \pm 0.062 \pm 0.007$ is also consistent with zero, as expected, across the kinematic range.

All amplitudes provide information on CFFs $\mathcal{H}$, $\mathcal{E}$, $\widetilde{\mathcal{H}}$ and $\widetilde{\mathcal{E}}$ at differing levels of twist and kinematic suppression. From inspection of Table 5.2, the $A_{\text{UL}}^{\sin\phi}$ $\left(A_{\text{LL}}^{\cos\phi}\right)$ amplitude relates to the imaginary (real) part of dominant CFF $\widetilde{\mathcal{H}}$ at leading-twist level through the $s_{1,\text{LP}}^{\mathcal{I}}$ $\left(c_{1,\text{LP}}^{\mathcal{I}}\right)$ Fourier coefficient, with a kinematically-suppressed twist–3 contribution from $s_{1,\text{LP}}^{\text{DVCS}}$ $\left(c_{1,\text{LP}}^{\text{DVCS}}\right)$. These are expected to be dominated by coefficients from $\mathcal{I}$ which, in this instance, are all functions of $\mathcal{C}_{\text{LP}}^{\mathcal{I}}$. At HERMES kinematics this $\mathcal{C}$-function, in addition
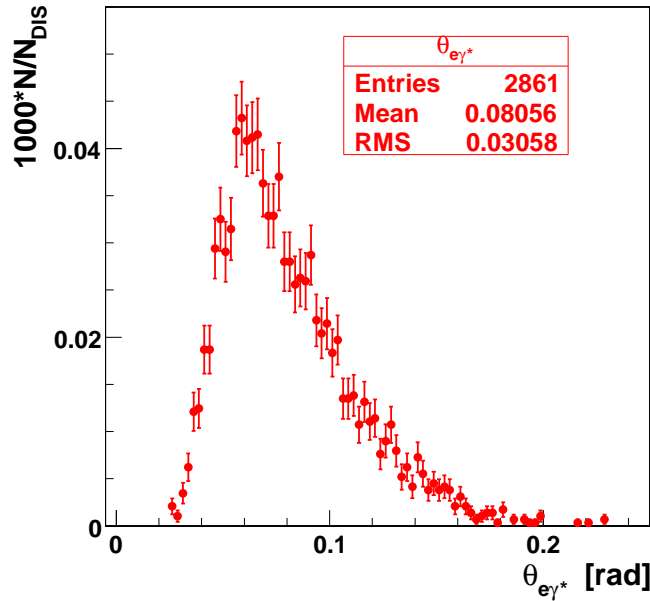
Figure 7.3: Polar angle $\theta_{e\gamma^*}$ between the incoming beam lepton and the virtual photon. On average they are offset by 0.08 rad.

to providing information on the real and imaginary parts of CFF $\widetilde{\mathcal{H}}$, also provides access to CFF $\mathcal{H}$ albeit suppressed by a factor of ξ.

The $A_{\mathrm{UL}}^{\sin(2\phi)}$ amplitude, the only amplitude the theoretical model fails to describe, relates to $\mathcal{C}_{\mathrm{LP}}^{\mathcal{I}}$ at twist–3 level with an additional dependence on leading-twist gluon-helicity-flip CFFs from $|\tau_{\mathrm{DVCS}}|^2$. Neither of these contributions are expected to be significant at HERMES kinematics. This large amplitude may arise from the gluon-helicity-flip GPD contributions from $|\tau_{\mathrm{DVCS}}|^2$. However, this is unlikely as the $A_{\mathrm{UL}}^{\sin(3\phi)}$ amplitude, which is solely related to gluon CFFs from the dominant $\mathcal{I}$ term, is consistent with zero across all kinematics.

The $A_{\mathrm{LL}}^{\cos(0\phi)}$ amplitude from the double-spin asymmetry relates to CFFs at twist–2 level from both $|\tau_{\mathrm{DVCS}}|^2$ and $\mathcal{I}$. The pure twist–3 $A_{\mathrm{LL}}^{\cos(2\phi)}$ amplitude, which is consistent with zero, is also related to the real part of CFF $\widetilde{\mathcal{H}}$.

7.1 Considering Transverse Target Polarisation

In Chapter 3, the Fourier expansion of the $e\,p \to e\,p\,\gamma$ differential cross-section was introduced neglecting contributions from transverse target polarisation. The virtual photon and incoming beam lepton were considered collinear $i.e.$ $\theta_{e\gamma^*} = 0$. In actuality, this is not

the case. Figure 7.3 shows the $\theta_{e\gamma^*}$ distribution for the exclusive data set. This is shown to be non-zero with a small mean value of approximately $80\,\mathrm{mrad}$.

In Ref. [112], the cross-section is Fourier expanded for an unpolarised lepton beam, considering transverse target components. The corresponding amplitudes, denoted $A_{\mathrm{UL,T}}^{\sin(n\phi)}$, are related to the extracted $A_{\mathrm{UL}}^{\sin(n\phi)}$ amplitudes as

$$
\begin{aligned}
A_{\mathrm{UL,T}}^{\sin\phi} - \cos\theta_{e\gamma^*}\, A_{\mathrm{UL}}^{\sin\phi} &= -\frac{1}{2}\sin\theta_{e\gamma^*}\left[2A_{\mathrm{UT},\mathcal{I}}^{\sin\varphi\cos(0\phi)}\right.\\
&\qquad\left. -A_{\mathrm{UT},\mathcal{I}}^{\sin\varphi\cos(2\phi)} + A_{\mathrm{UT},\mathcal{I}}^{\cos\varphi\sin(2\phi)}\right],
\end{aligned}
\tag{7.1}
$$

$$
\begin{aligned}
A_{\mathrm{UL,T}}^{\sin(2\phi)} - \cos\theta_{e\gamma^*}\, A_{\mathrm{UL}}^{\sin(2\phi)} &= -\frac{1}{2}\sin\theta_{e\gamma^*}\left[A_{\mathrm{UT},\mathcal{I}}^{\sin\varphi\cos\phi} + A_{\mathrm{UT},\mathcal{I}}^{\cos\varphi\sin\phi}\right.\\
&\qquad\left. -A_{\mathrm{UT},\mathcal{I}}^{\sin\varphi\cos(3\phi)} + A_{\mathrm{UT},\mathcal{I}}^{\cos\varphi\sin(3\phi)}\right],
\end{aligned}
\tag{7.2}
$$

where the $A_{\mathrm{UT},\mathcal{I}}$ amplitudes have been extracted from transversely polarised hydrogen data at HERMES [22]. The results show estimated transverse target polarisation relative corrections of 3.95% and 3.77% to the $\sin\phi$ and $\sin(2\phi)$ amplitudes respectively. This small influence justifies the initial decision to neglect transverse target polarisation contributions.

7.2 Comparison with HERMES Hydrogen Measurements

A PhD thesis performing the extraction of the $\mathcal{A}_{\mathrm{UL}}$ at HERMES, which also used the 96d0 and 97d1 data productions, was published in 2006 [61]. The analysis presented in this thesis has been performed with improved analytical techniques allowing the simultaneous extraction of $\mathcal{A}_{\mathrm{LL}}$ and $\mathcal{A}_{\mathrm{LU}}$ also. The ϕ-binned least-squares method used for the initial analysis in Ref. [61] was limited to the extraction of the $\mathcal{A}_{\mathrm{UL}}$ only. The data selection differs negligibly between the two analyses. The $A_{\mathrm{UL}}^{\sin(n\phi)}$ amplitudes are compared in Fig. 7.4. Only negligible differences are observed over the kinematic range. The initial analysis ("Kopytin") extended the extraction to five bins in x_{B} and Q^2 providing more data points, but with poorer statistical precision across the kinematic range. However, four bins were used in the analysis outlined in this thesis to increase statistical precision and maintain consistency with Ref. [22]. The improved determination of the systematic uncertainties, detailed in Chapter 6, results in a significantly decreased overall uncertainty. In Section 5.8 the $A_{\mathrm{LU}}^{\sin(n\phi)}$ amplitudes of the beam-helicity asymmetry were also extracted to verify the result extracted from the $1996-2005$ HERMES hydrogen data set [23] of which the longitudinally polarised hydrogen data set is a small subset of. Figure 7.5 shows the comparison between the $A_{\mathrm{LU}}^{\sin(n\phi)}$ amplitudes extracted from this small polarised
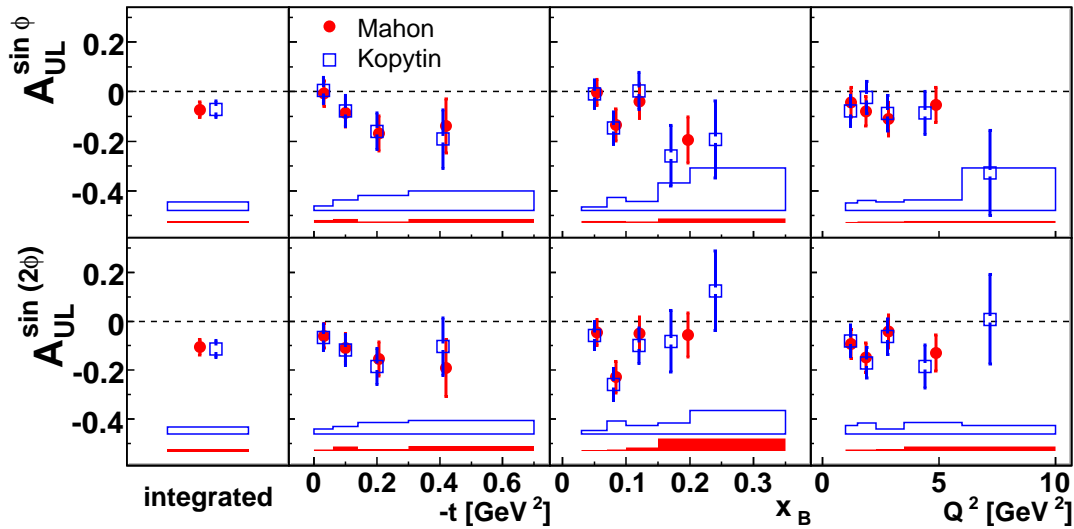
Figure 7.4: Comparison of the $A_{\text{UL}}^{\sin(n\phi)}$ amplitudes extracted from this analysis (Mahon) and the original, singly-extracted amplitudes (Kopytin) integrated over the HERMES acceptance and in kinematics bins of $-t$, x_{B}, and Q^2. Systematic uncertainties are also presented. Both sets of amplitudes agree well with only minor differences observed.

subset and the $A_{\text{LU},\mathcal{I}}^{\sin(n\phi)}$ amplitudes extracted from the larger data set. As the $A_{\text{LU}}^{\sin(n\phi)}$ amplitudes are extracted from positron data only, the dominant contributions from $\mathcal{I}$ cannot be disentangled from the suppressed $|\tau_{\text{DVCS}}|^2$ contributions. This suppression has been verified by the results from Ref. [23].

All amplitudes are shown to be consistent within experimental uncertainty although the $A_{\text{LU}}^{\sin\phi}$ amplitude was found to have a smaller integrated value than $A_{\text{LU},\mathcal{I}}^{\sin\phi}$. No kinematic dependences are observed from either data set. As expected, the twist–3 $A_{\text{UL}}^{\sin(2\phi)}$ amplitude is kinematically-suppressed with respect to the leading-twist $A_{\text{UL}}^{\sin\phi}$ amplitude and is consistent with zero. The results from both analyses agree well across the kinematic range.

7.3   Comparison with HERMES Deuterium Measurements

Recent HERMES measurements of DVCS off a longitudinally polarised deuterium target are presented in Refs. [60,113]. The asymmetry amplitudes arising from the spin 1 deuteron target receive additional contributions from Fourier coefficients relating to the target tensor polarisation P_{zz} which is defined as

$$P_{zz} = \frac{N^+ + N^- - 2N^0}{N^+ + N^- + N^0} \, . \tag{7.3}$$
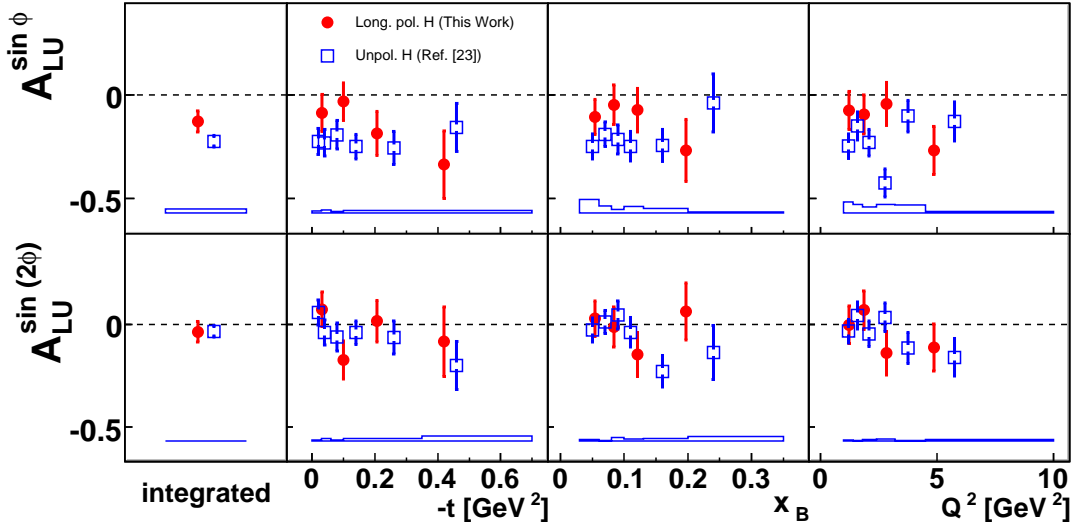
Figure 7.5: $A_{\mathrm{LU},\mathcal{I}}^{\sin(n\phi)}$ ($A_{\mathrm{LU}}^{\sin(n\phi)}$) amplitudes of the beam-helicity asymmetry sensitive to $\mathcal{I}$ ($|\tau_{\mathrm{DVCS}}|^2$ and $\mathcal{I}$), from the entire (longitudinally polarised only) proton data set, as a function of $-t$, x_{B}, and Q^2. The open squares (filled circles) represent the results from HERMES unpolarised proton data [23] (this analysis). The error bars show the statistical uncertainties and the open bands represent the systematic uncertainty from the entire data set only.

Here N^-, N^0 and N^+ are the relative populations of spin states with corresponding spin projections of $-1, 0$ and $+1$ respectively.

The results of the $\mathcal{A}_{\mathrm{UL}}$ extraction from hydrogen and deuterium data are compared in Fig. 7.6. At low values of $-t$ the $A_{\mathrm{UL}}^{\sin(n\phi)}$ amplitudes agree. For the deuterium case this corresponds to the 'coherent-enriched' region in which approximately 40% of events involve scattering off the whole deuteron, which stays intact. In the highest two $-t$ bins, the 'incoherent-enriched' region, the scattering is predominantly off a constituent proton or neutron. The $A_{\mathrm{UL}}^{\sin(2\phi)}$ amplitudes reflect this agreement at low $-t$. The differences in the high $-t$ region could potentially be explained from the effects of scattering off the neutron. Across other kinematics the results are observed to be consistent in all but the second x_{B} bin.

The $A_{\mathrm{LL}}^{\cos(n\phi)}$ amplitudes are also compared in Fig. 7.6. Over the kinematic range there are no significant differences between the $A_{\mathrm{LL}}^{\cos(0\phi)}$ and $A_{\mathrm{LL}}^{\cos(2\phi)}$ amplitudes. The $A_{\mathrm{LL}}^{\cos\phi}$ from deuterium data is found to be small, non-zero and positive in agreement with theoretical calculations which predict an asymmetry of opposite sign to that from the hydrogen data.

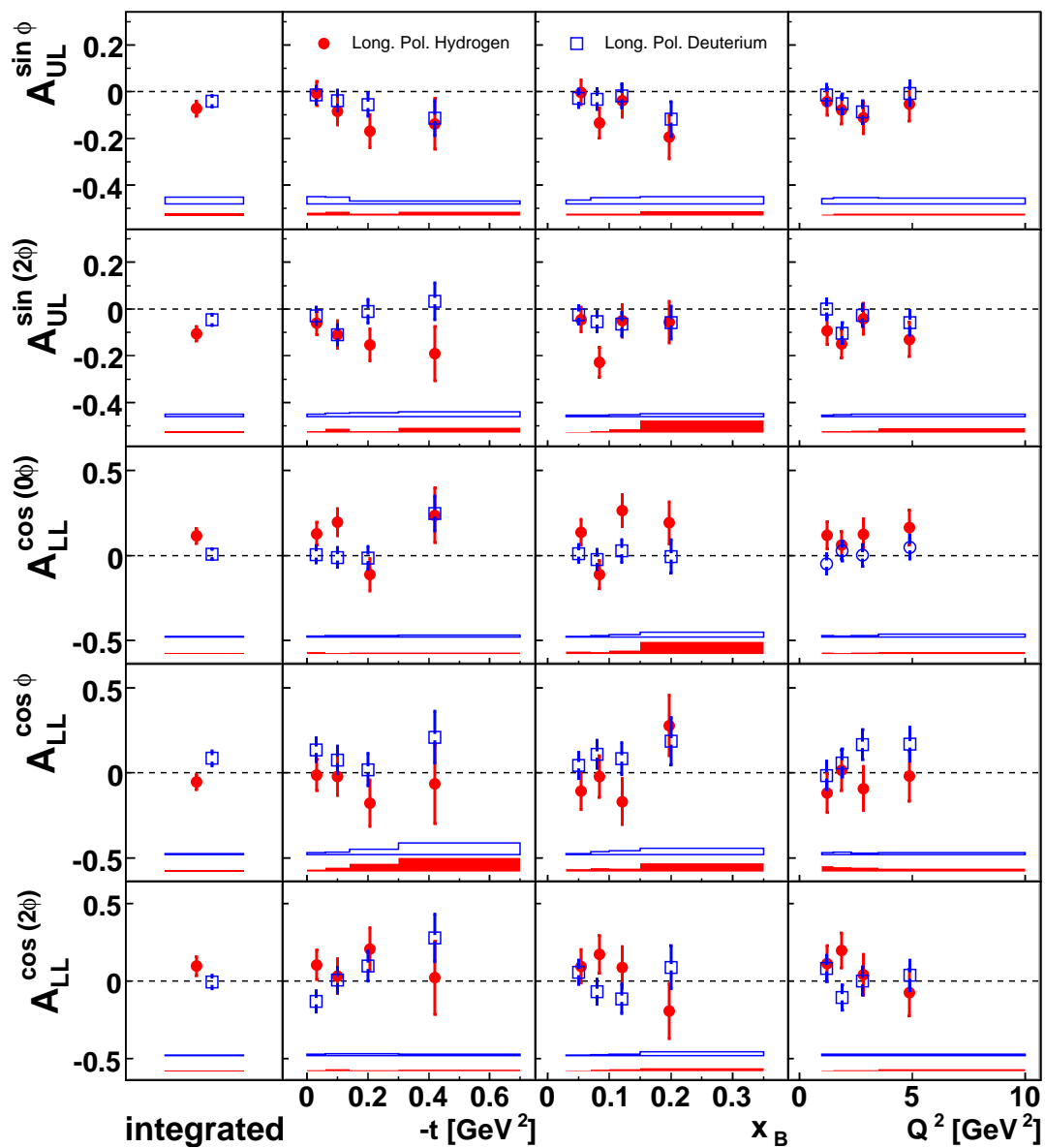**Figure 7.6:** Comparison of the $A_{\mathrm{UL}}^{\sin(n\phi)}$ and $A_{\mathrm{LL}}^{\cos(n\phi)}$ amplitudes extracted from longitudinally polarised hydrogen (filled circles) and deuterium data (open squares) as a function of $-t$, x_{B}, and Q^2.

	$\langle -t \rangle$	$\langle x_{\mathrm{B}} \rangle$	$\langle Q^2 \rangle$	$A_{\mathrm{UL}}^{\sin\phi}$	$A_{\mathrm{UL}}^{\sin(2\phi)}$
	$[\mathrm{GeV}^2]$	-	$[\mathrm{GeV}^2]$	$\pm \delta_{\mathrm{stat.}} \pm \delta_{\mathrm{syst.}}$	$\pm \delta_{\mathrm{stat.}} \pm \delta_{\mathrm{syst.}}$
HERMES	0.12	0.10	2.46	$-0.073 \pm 0.032 \pm 0.007$	$-0.106 \pm 0.032 \pm 0.008$
CLAS	0.31	0.28	1.82	$-0.252 \pm 0.042 \pm 0.020$	$-0.022 \pm 0.045 \pm 0.021$

Table 7.1: Comparison of the $A_{\mathrm{UL}}^{\sin(n\phi)}$ amplitudes extracted from HERMES and CLAS longitudinally polarised proton data. The values shown have been integrated over the kinematic ranges of each experiment and the average kinematics are presented.

7.4 Comparison with CLAS Measurements

The CLAS experiment [101] at JLAB has also published results of their $\mathcal{A}_{\mathrm{UL}}$ from a longitudinally polarised proton-rich NH_3 target [114]. This result was extracted from data taken in $2000 - 2001$ using a $5.7\,\mathrm{GeV}$ electron beam. This result was extracted using a least-squares fit of functional form $\mathcal{A}_{\mathrm{UL}}(\phi) \simeq \alpha \sin\phi + \beta \sin(2\phi)$ where $\alpha\,(\beta)$ is analogous to $A_{\mathrm{UL}}^{\sin\phi} \left(A_{\mathrm{UL}}^{\sin(2\phi)} \right)$. The extracted results are:

$$\alpha = -0.252 \pm 0.042(\mathrm{stat}) \pm 0.020(\mathrm{syst})$$
$$\beta = -0.022 \pm 0.045(\mathrm{stat}) \pm 0.021(\mathrm{syst})$$

The average CLAS kinematics are shown in Table 7.1 alongside those obtained from HERMES. Here, the sign of the CLAS results have been manipulated for consistency with the sign of the HERMES beam charge and ϕ-convention.

The $-t$ and x_{B} dependences and integrated values of the $A_{\mathrm{UL}}^{\sin\phi}$ amplitudes from HERMES and CLAS are compared in Fig. 7.7. Both are presented alongside theoretical calculations from Ref. [49] with $b_{\mathrm{valence}} = b_{\mathrm{sea}} = 1$. The integrated CLAS amplitude was found to be significantly larger. However, both results are in similar agreement with predictions from the same GPD model across the relative $-t$ and x_{B} ranges. This can possibly be explained by the different kinematic regions of the two experiments. The lower beam energy of CLAS allows them to access higher values of ξ and x_{B} which also increases the relative contributions from other CFFs to $\mathcal{A}_{\mathrm{UL}}$. This is observed in Eqs. 3.32 and 3.33. In particular the sensitivity to $\mathcal{H}$ and $\widetilde{\mathcal{E}}$ are increased, especially at higher average values of $-t$ reached by CLAS. It should also be noted from Eq. 3.16 that as different beam charges have been used, the asymmetry amplitudes extracted at both experiments differ from each other with respect to the sign of the contribution from $\mathcal{I}$.
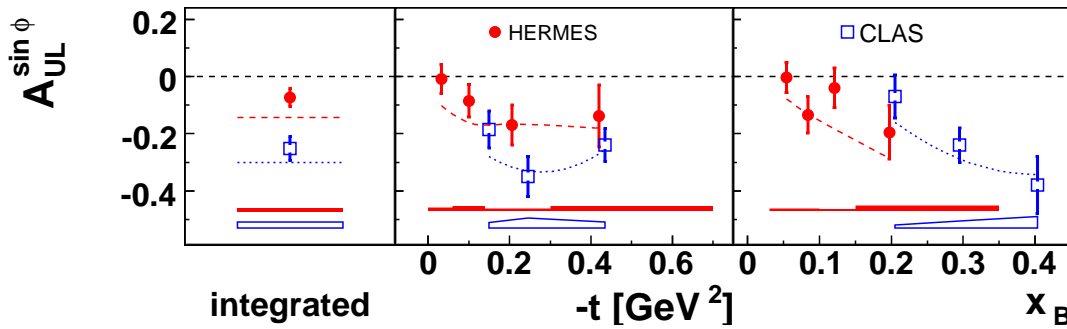
Figure 7.7: The $A_{UL}^{\sin\phi}$ amplitudes extracted from proton data at the HERMES (filled circles) and CLAS (open squares) experiments in bins of $-t$ and x_B. The error bars and bands represent the statistical and systematic uncertainties respectively. These are presented in comparison to a GPD model prediction [49] with $b_{\text{valence}} = b_{\text{sea}} = 1$ for HERMES (dashed lines) and CLAS (dotted lines) kinematics.

Unfortunately CLAS does not provide Q^2-dependences or any kinematic dependence of the $A_{UL}^{\sin(2\phi)}$ amplitude to enable further comparison.

7.5 Future Measurements

In the near-future, measurements of the single-spin $\mathcal{A}_{UL}$ and double-spin $\mathcal{A}_{LL}$ asymmetries from longitudinally polarised proton data are planned at CLAS using their $5.7\,\text{GeV}$ electron beam [115]. Figure 7.8 shows the expected statistical precision of the $A_{UL}^{\sin\phi}$ amplitude from these forthcoming measurements in comparison with the results from this work and those previously measured at CLAS. This experiment will not only provide measurements with significantly increased statistical precision, it will also provide complimentary results of $\mathcal{A}_{LL}$ across a different range in x_B which will also be used in future extractions of $\widetilde{\mathcal{H}}$.

Several measurements of the beam-helicity asymmetry $\mathcal{A}_{LU}$ have already been made by HERMES. In addition to those shown in Fig. 7.5, the analysis performed in Ref. [116] has extracted, for the first time, results taken using the $2006 - 2007$ unpolarised hydrogen data set. These data, taken after the installation of the Recoil Detector, represent over twice the statistics of the $1996 - 2005$ data set. The simultaneous extraction of $\mathcal{A}_C$, $\mathcal{A}_{LU}^{\mathcal{I}}$ and $\mathcal{A}_{LU}^{\text{DVCS}}$ from the $2006 - 2007$ data was performed in a similar way to the analysis of the $1996 - 2005$ hydrogen data. Both results were found to be consistent. Further studies are required before the first measurements can be made using Recoil Detector information. It is anticipated that the detection of the recoiling proton will decrease the resonance contamination in the exclusive sample to below 1% [96]. This will allow the extraction
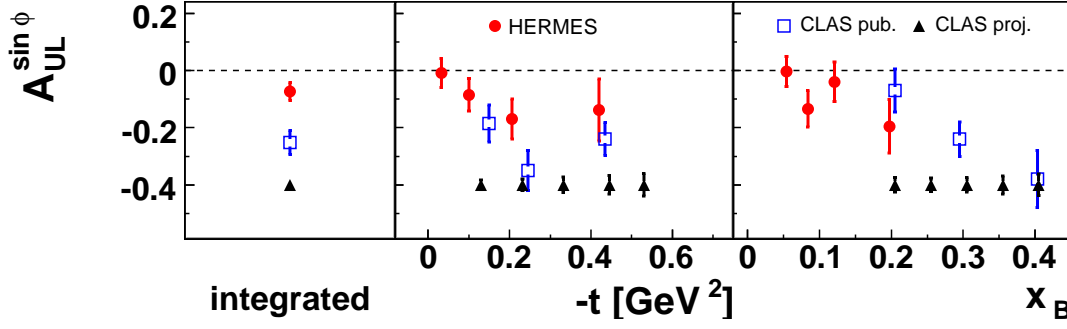
Figure 7.8: Projected statistical precision of the upcoming $A_{\mathrm{UL}}^{\sin\phi}$ amplitude extraction at CLAS [115] (triangles) in comparison with published HERMES results from this thesis (circles) and CLAS [114] (squares) in bins of $-t$ and x_{B}. An arbitrary amplitude value has been chosen for these projected results.

of asymmetries solely from the BH/DVCS process, and will enable a clearer comparison with the GPD model.

After the proposed CLAS 12 GeV upgrade, their DVCS programme [44] will also aim to provide high statistics measurements of both $\mathcal{A}_{\mathrm{UL}}$ and $\mathcal{A}_{\mathrm{LU}}$. At this higher beam energy, their kinematic range will be extended in x_{B} (down to 0.1 and up to 0.7) and Q^2 (up to $9\,\mathrm{GeV}^2$). These future measurements will be vital in the attempt to better understand GPDs H and $\widetilde{H}$.

Chapter 8

Conclusions and Outlook

Three polarisation-dependent asymmetries in the $e\,p \to e\,p\,\gamma$ cross-section are presented. They arise from the hard exclusive leptoproduction of real photons, *i.e.* Deeply Virtual Compton Scattering (DVCS), and its interference with the Bethe-Heitler (BH) process. The extracted asymmetry amplitudes are related to different combinations of Compton Form Factors (CFFs) entering at differing levels of suppression. Each CFF conveys information on the corresponding Generalised Parton Distribution (GPD) which provides a multi-dimensional description of the partonic structure of the nucleon.

The data were taken using a 27.57 GeV longitudinally polarised positron beam incident on a longitudinally polarised hydrogen gas target at HERMES. The amplitudes presented were corrected for contributions from semi-inclusive and exclusive π^0 background processes, and also contained an average contribution of 12.9% from resonance production which could not be separated from the analysed data sample.

The asymmetry amplitudes extracted in a single bin at average kinematics of $\langle -t \rangle = 0.115\,\mathrm{GeV}^2$, $\langle x_\mathrm{B} \rangle = 0.096$ and $\langle Q^2 \rangle = 2.459\,\mathrm{GeV}^2$ are shown in Fig. 8.1 in comparison with similar measurements, described in Chapter 7, taken at HERMES and CLAS. The single-spin asymmetry $\mathcal{A}_\mathrm{UL}$ dependent on the polarisation of the target, was found to have a non-zero, leading-twist $A_\mathrm{UL}^{\sin\phi}$ amplitude. The kinematic trends are in agreement with predictions from a GPD model outlined in Ref. [49]. The $A_\mathrm{UL}^{\sin(2\phi)}$ amplitude was found to be unexpectedly large. This twist–3 amplitude was expected to be suppressed with respect to $A_\mathrm{UL}^{\sin\phi}$ and to be consistent with zero. This disagreement, so far, has not been explained. These two amplitudes provide information on the imaginary part of CFF $\widetilde{\mathcal{H}}$, and thus GPD $\widetilde{H}$, at different levels of twist and kinematic suppression.

The double-spin asymmetry $\mathcal{A}_\mathrm{LL}$ is dependent on the product of the beam and target
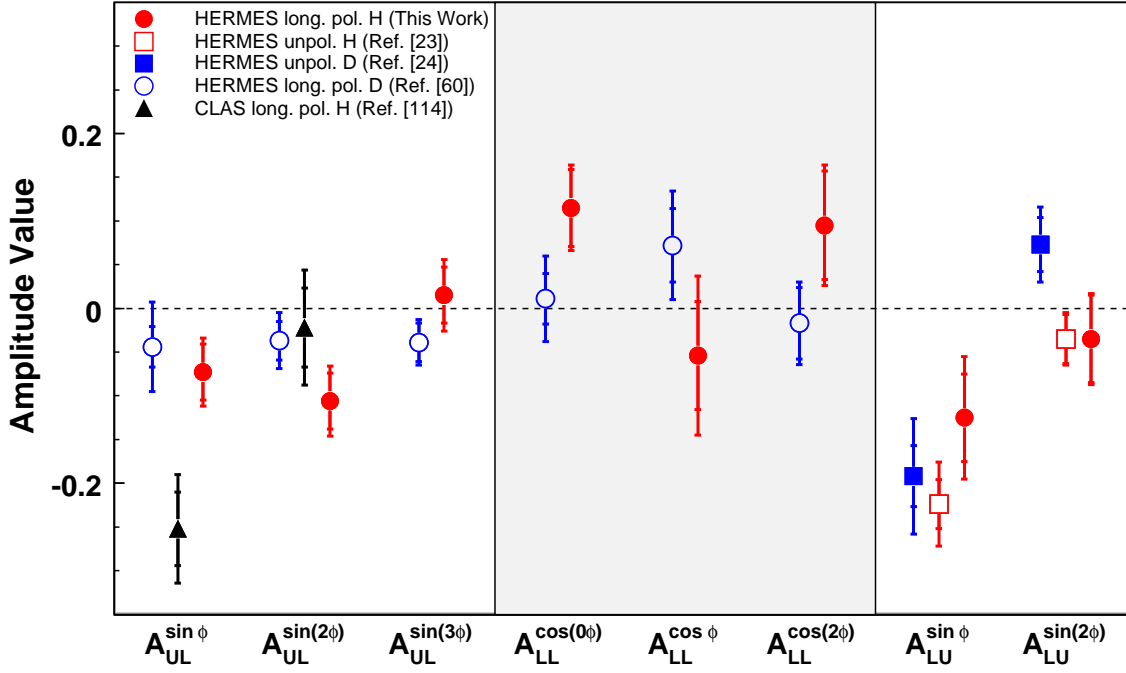
Figure 8.1: Summary of the $A_{\mathrm{UL}}^{\sin(n\phi)}$, $A_{\mathrm{LL}}^{\cos(n\phi)}$ and $A_{\mathrm{LU}}^{\sin(n\phi)}$ amplitudes extracted in this analysis (red filled circles) integrated over all kinematics in the HERMES acceptance. These are shown in comparison with HERMES measurements taken on a longitudinally polarised deuterium target [60] (open blue circles). The results from the $1996 - 2005$ HERMES hydrogen [23] (open red squares), deuterium [24] (filled blue squares), and longitudinally polarised CLAS [114] (filled black triangles) data sets are also shown. The CLAS data points are taken at different average kinematics and with the opposite beam charge as described in Section 7.4. The $A_{\mathrm{LU}}^{\sin(n\phi)}$ amplitudes from this work are assigned the same systematic uncertainty as the amplitudes from Ref. [23].

polarisations. This was extracted for the first time. A non-zero $A_{\mathrm{LL}}^{\cos(0\phi)}$ amplitude was observed. This arises at leading-twist from both the squared-DVCS $|\tau_{\mathrm{DVCS}}|^2$ and interference $\mathcal{I}$ terms of the $e\,p \to e\,p\,\gamma$ cross-section. The $A_{\mathrm{LL}}^{\cos(0\phi)}$ and $A_{\mathrm{LL}}^{\cos\phi}$ amplitudes differ from all other extracted amplitudes reported in this thesis in receiving an additional, and dominant, contribution from the squared-BH $|\tau_{\mathrm{BH}}|^2$ term. The leading-twist $A_{\mathrm{LL}}^{\cos\phi}$ and twist–3 $A_{\mathrm{LL}}^{\cos(2\phi)}$ amplitudes are both compatible with zero across all kinematics and in agreement with theoretical predictions sensitive to the real part of $\widetilde{\mathcal{H}}$. The statistical precision is such however, that no kinematic dependences can be discerned for this asymmetry.

The beam-helicity asymmetry $\mathcal{A}_{\mathrm{LU}}$ has previously been extracted from a significantly larger superset of HERMES data [23]. The result extracted in this thesis is consistent with the previous extraction within experimental uncertainty. Neither, however, are described by the GPD model which predicts an amplitude twice as large.
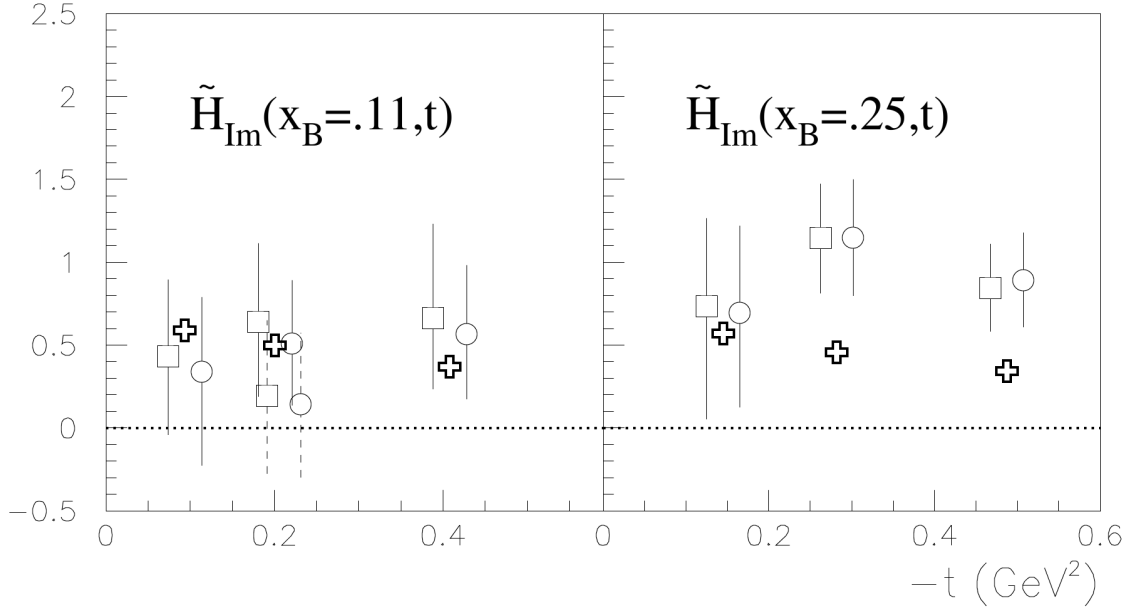
Figure 8.2: The t-dependence of the imaginary part of CFF $\widetilde{\mathcal{H}}$ (labelled $\tilde{H}_{Im}$) extracted from HERMES data, including the $A_{UL}^{\sin\phi}$ amplitude from this work, at $\langle x_B \rangle = 0.108$ (left) and from CLAS data at $\langle x_B \rangle = 0.250$ (right). The squares (circles) represent the results when the extraction is bound to five (three) times the VGG prediction, which are shown by the open crosses. The solid (dashed) error bars in the left plot represent the result excluding (including) the $\mathcal{A}_{LL}$ amplitudes. The data point at $\langle -t \rangle = 0.031$ has been omitted as the corresponding $A_{UL}^{\sin\phi}$ amplitude is too close to zero. Figure taken from Ref. [118].

First attempts at extracting CFF $\mathcal{H}$ have already been performed using HERMES [41] and CLAS [42] DVCS results, while an initial global fit to GPD H using experimental data has been published [40] which also used results from H1 and ZEUS. From CLAS measurements [62, 114], the imaginary part of CFF $\widetilde{\mathcal{H}}$ has also been extracted [117].

Whereas the results of $\mathcal{A}_{UL}$ and $\mathcal{A}_{LL}$ presented in this thesis are not particularly sensitive to $\mathcal{H}$, they do provide, for the first time, information on both the real and imaginary parts of $\widetilde{\mathcal{H}}$. Recently, the $A_{UL}^{\sin\phi}$ amplitude presented in this thesis has been used to extract the imaginary part of CFF $\widetilde{\mathcal{H}}$ (labelled $\tilde{H}_{Im}$), for the first time, at HERMES kinematics [118]. The t-dependence of this result is shown in Fig. 8.2 in comparison with the same CFF extracted in Ref. [117] using CLAS data. The results suggest that $\tilde{H}_{Im}$ increases with x_B and is flat across the range in t.

It is foreseen that this information, relating to GPD $\widetilde{H}$, will be used alongside more precise results from future measurements [44, 115] as input into GPD models which will be vital in providing a better understanding of GPD $\widetilde{H}$, and hence the internal structure of the nucleon.

Appendix A

Correlation Matrices
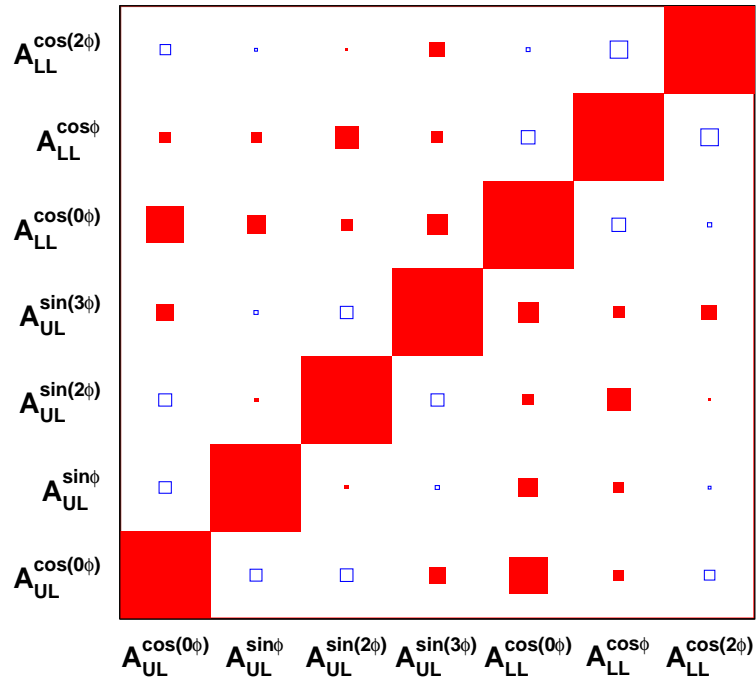
Figure A.1: Correlation matrix of the simultaneous extraction of the asymmetry amplitudes from Eqs. 5.43 and 5.44. Filled (Open) squares represent positive (negative) values and the area of the symbols represents the size of the correlation.
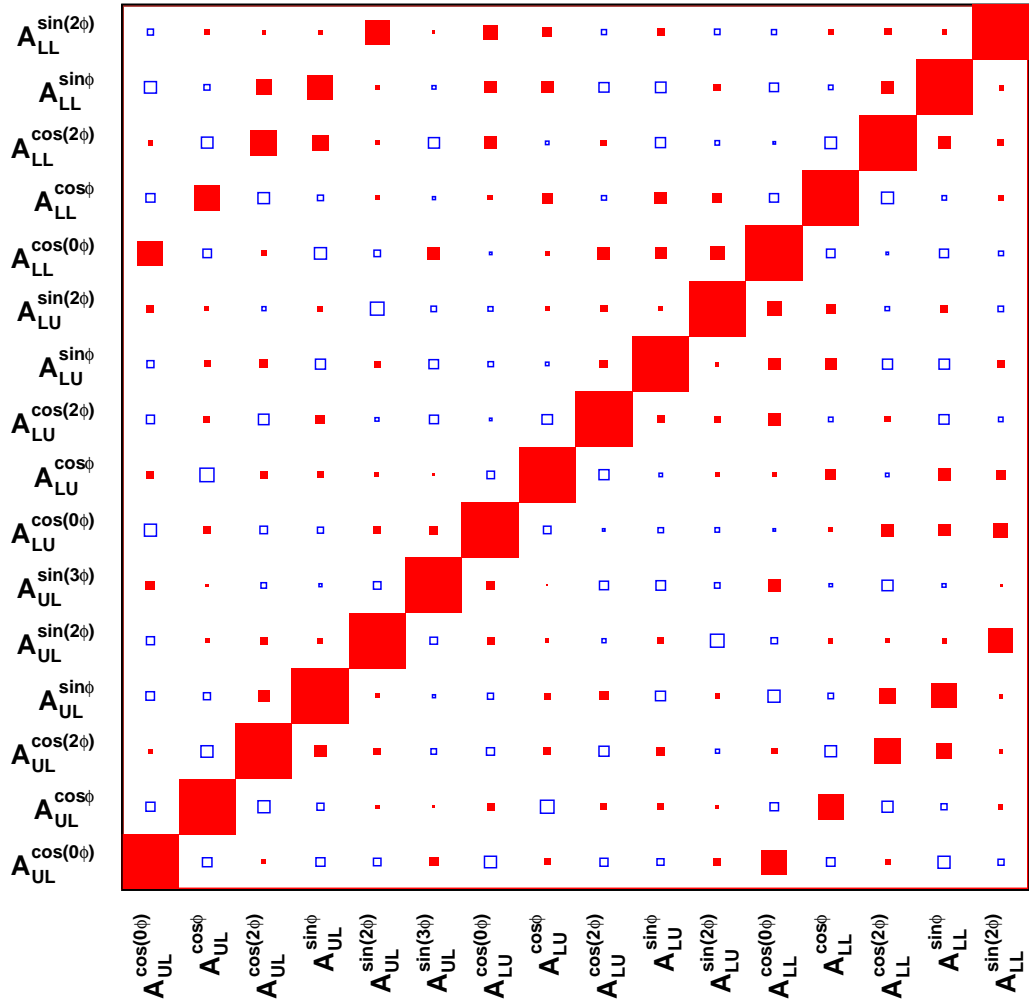
Figure A.2: Correlation matrix of the simultaneous extraction of the asymmetry amplitudes from Eqs. 5.40 − 5.42. Filled (Open) squares represent positive (negative) values and the area of the symbols represents the size of the correlation.

Appendix B

Consistency-Test Amplitudes

These amplitudes were extracted in Section 5.7 as a test of the extraction and normalisation methods. They are compatible with zero as expected.
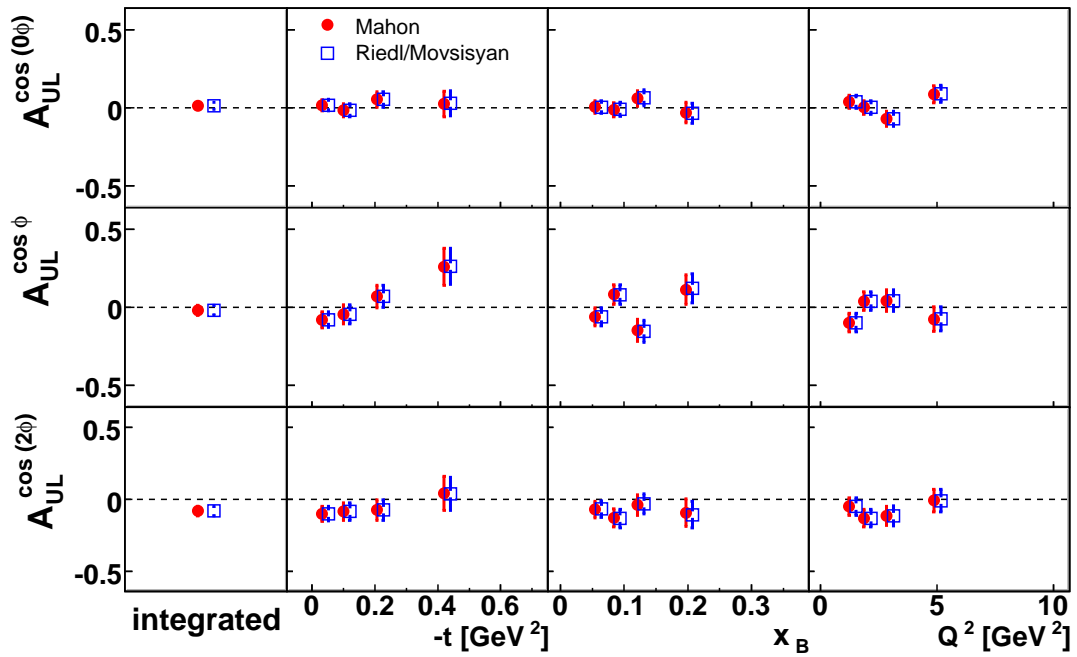
Figure B.1: Cross-check of the extracted $A_{\mathrm{UL}}^{\cos(n\phi)}$ amplitudes of the longitudinally polarised target spin asymmetry integrated over all kinematics in the HERMES acceptance and as a function of $-t$, x_{B}, and Q^2. These are consistency-test terms only.

Figure B.2: Cross-check of the extracted $A_{\mathrm{LL}}^{\sin(n\phi)}$ amplitudes of the double-spin asymmetry integrated over all kinematics in the HERMES acceptance and as a function of $-t$, x_{B}, and Q^2. These are consistency-test terms only.

Figure B.3: Cross-check of the extracted $A_{\mathrm{UL}}^{\cos(n\phi)}$ amplitudes of the beam-helicity asymmetry integrated over all kinematics in the HERMES acceptance and as a function of $-t$, x_{B}, and Q^2. These are consistency-test terms only.
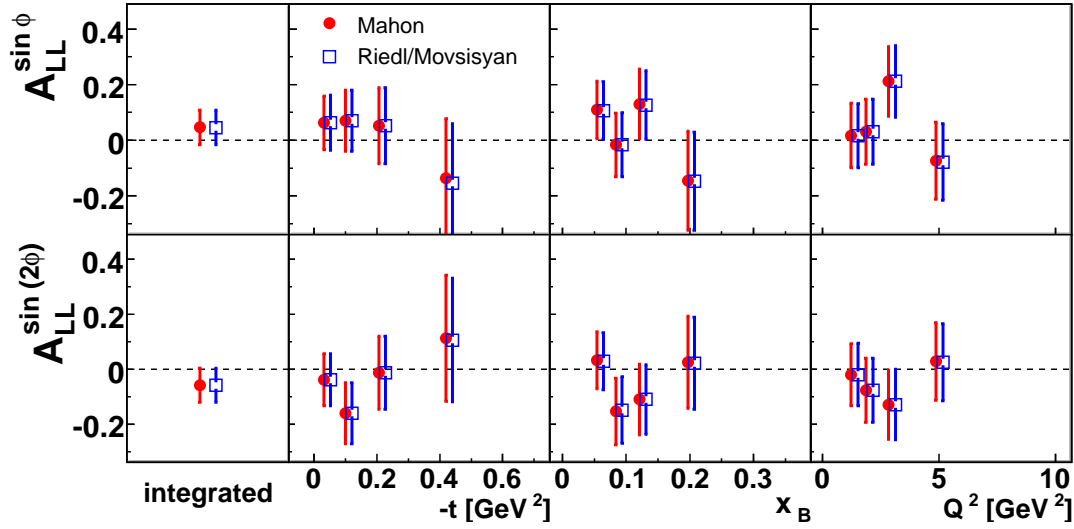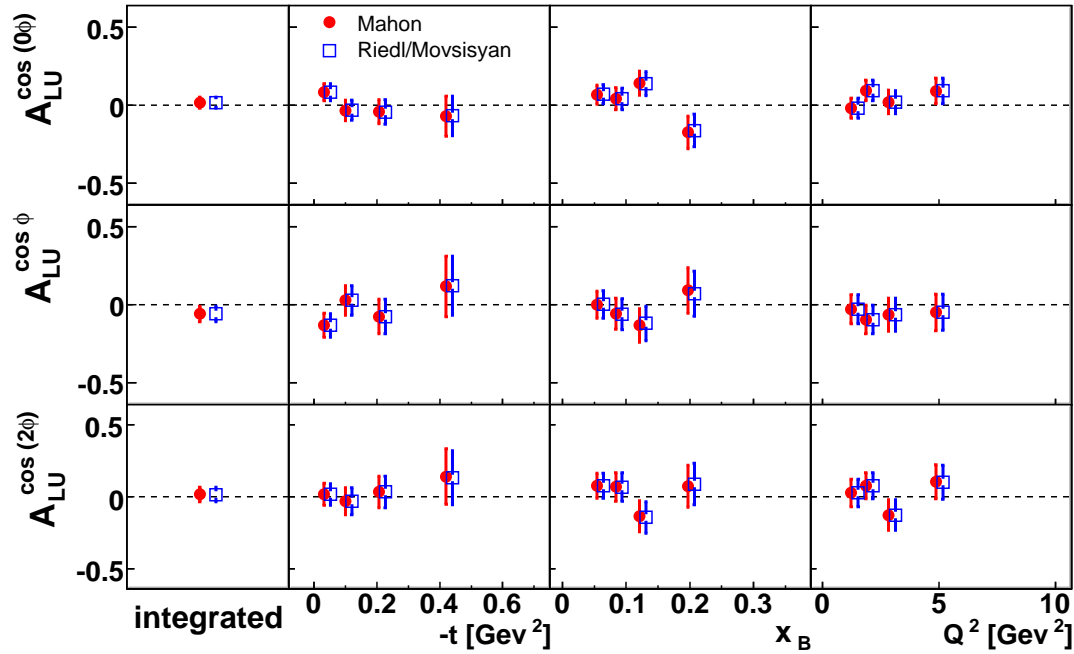
Appendix C

Tables of Results

Kinematic Bin	$\langle -t \rangle$ [GeV^2]	$\langle x_B \rangle$ -	$\langle Q^2 \rangle$ [GeV^2]	$A_{\mathrm{UL}}^{\sin\phi}$ $\pm \delta_{\mathrm{stat}} \pm \delta_{\mathrm{syst}}$	$A_{\mathrm{UL}}^{\sin(2\phi)}$ $\pm \delta_{\mathrm{stat}} \pm \delta_{\mathrm{syst}}$	$A_{\mathrm{UL}}^{\sin(3\phi)}$ $\pm \delta_{\mathrm{stat}} \pm \delta_{\mathrm{syst}}$
integrated	0.115	0.096	2.459	$-0.073 \pm 0.032 \pm 0.007$	$-0.106 \pm 0.032 \pm 0.008$	$0.015 \pm 0.032 \pm 0.009$
$0.00 \leq -t \leq 0.06$	0.031	0.079	1.982	$-0.008 \pm 0.051 \pm 0.012$	$-0.060 \pm 0.050 \pm 0.007$	$0.024 \pm 0.049 \pm 0.005$
$0.06 < -t \leq 0.14$	0.094	0.103	2.531	$-0.085 \pm 0.057 \pm 0.017$	$-0.110 \pm 0.059 \pm 0.018$	$-0.016 \pm 0.059 \pm 0.009$
$0.14 < -t \leq 0.30$	0.201	0.110	2.883	$-0.169 \pm 0.070 \pm 0.007$	$-0.154 \pm 0.069 \pm 0.008$	$0.020 \pm 0.069 \pm 0.016$
$0.30 < -t \leq 0.70$	0.408	0.123	3.587	$-0.138 \pm 0.109 \pm 0.017$	$-0.191 \pm 0.116 \pm 0.021$	$0.014 \pm 0.115 \pm 0.017$
$0.03 < x_B \leq 0.07$	0.096	0.054	1.437	$-0.003 \pm 0.053 \pm 0.008$	$-0.045 \pm 0.053 \pm 0.004$	$0.031 \pm 0.053 \pm 0.004$
$0.07 < x_B \leq 0.10$	0.099	0.084	2.115	$-0.134 \pm 0.064 \pm 0.008$	$-0.228 \pm 0.064 \pm 0.007$	$-0.077 \pm 0.060 \pm 0.009$
$0.10 < x_B \leq 0.15$	0.123	0.121	3.108	$-0.039 \pm 0.070 \pm 0.007$	$-0.051 \pm 0.069 \pm 0.015$	$0.080 \pm 0.069 \pm 0.013$
$0.15 < x_B \leq 0.35$	0.188	0.198	4.934	$-0.195 \pm 0.093 \pm 0.018$	$-0.056 \pm 0.089 \pm 0.052$	$0.101 \pm 0.090 \pm 0.012$
$1.0 < Q^2 \leq 1.5$	0.085	0.056	1.236	$-0.043 \pm 0.059 \pm 0.004$	$-0.093 \pm 0.059 \pm 0.007$	$0.016 \pm 0.058 \pm 0.006$
$1.5 < Q^2 \leq 2.3$	0.098	0.079	1.862	$-0.079 \pm 0.060 \pm 0.007$	$-0.149 \pm 0.061 \pm 0.007$	$-0.036 \pm 0.060 \pm 0.007$
$2.3 < Q^2 \leq 3.5$	0.123	0.108	2.829	$-0.111 \pm 0.068 \pm 0.007$	$-0.042 \pm 0.067 \pm 0.009$	$0.059 \pm 0.066 \pm 0.009$
$3.5 < Q^2 \leq 10.0$	0.178	0.170	4.865	$-0.054 \pm 0.071 \pm 0.008$	$-0.130 \pm 0.074 \pm 0.019$	$0.034 \pm 0.074 \pm 0.010$

Table C.1: Results of the $A_{\mathrm{UL}}^{\sin(n\phi)}$ amplitudes with statistical and systematic uncertainties and average kinematics from polarised hydrogen data for each $-t$, x_B, and Q^2 bin.

Kinematic Bin	$\langle -t \rangle$ [GeV^2]	$\langle x_{\mathrm{B}} \rangle$ -	$\langle Q^2 \rangle$ [GeV^2]	$A_{\mathrm{LL}}^{\cos(0\phi)}$ $\pm \delta_{\mathrm{stat}} \pm \delta_{\mathrm{syst}}$	$A_{\mathrm{LL}}^{\cos \phi}$ $\pm \delta_{\mathrm{stat}} \pm \delta_{\mathrm{syst}}$	$A_{\mathrm{LL}}^{\cos(2\phi)}$ $\pm \delta_{\mathrm{stat}} \pm \delta_{\mathrm{syst}}$
integrated	0.115	0.096	2.459	$0.115 \pm 0.044 \pm 0.004$	$-0.054 \pm 0.062 \pm 0.029$	$0.095 \pm 0.062 \pm 0.007$
$0.00 \leq -t \leq 0.06$	0.031	0.079	1.982	$0.129 \pm 0.068 \pm 0.010$	$-0.012 \pm 0.094 \pm 0.010$	$0.104 \pm 0.097 \pm 0.006$
$0.06 < -t \leq 0.14$	0.094	0.103	2.531	$0.197 \pm 0.080 \pm 0.007$	$-0.021 \pm 0.112 \pm 0.022$	$0.031 \pm 0.114 \pm 0.014$
$0.14 < -t \leq 0.30$	0.201	0.110	2.883	$-0.113 \pm 0.095 \pm 0.008$	$-0.179 \pm 0.137 \pm 0.044$	$0.206 \pm 0.136 \pm 0.007$
$0.30 < -t \leq 0.70$	0.408	0.123	3.587	$0.237 \pm 0.162 \pm 0.009$	$-0.065 \pm 0.235 \pm 0.079$	$0.020 \pm 0.211 \pm 0.009$
$0.03 < x_{\mathrm{B}} \leq 0.07$	0.096	0.054	1.437	$0.137 \pm 0.076 \pm 0.014$	$-0.108 \pm 0.108 \pm 0.013$	$0.094 \pm 0.102 \pm 0.003$
$0.07 < x_{\mathrm{B}} \leq 0.10$	0.099	0.084	2.115	$-0.111 \pm 0.083 \pm 0.012$	$-0.023 \pm 0.123 \pm 0.018$	$0.171 \pm 0.117 \pm 0.008$
$0.10 < x_{\mathrm{B}} \leq 0.15$	0.123	0.121	3.108	$0.265 \pm 0.095 \pm 0.020$	$-0.169 \pm 0.135 \pm 0.016$	$0.087 \pm 0.132 \pm 0.012$
$0.15 < x_{\mathrm{B}} \leq 0.35$	0.188	0.198	4.934	$0.192 \pm 0.125 \pm 0.070$	$0.279 \pm 0.178 \pm 0.047$	$-0.193 \pm 0.176 \pm 0.017$
$1.0 < Q^2 \leq 1.5$	0.085	0.056	1.236	$0.118 \pm 0.080 \pm 0.009$	$-0.120 \pm 0.114 \pm 0.029$	$0.111 \pm 0.115 \pm 0.004$
$1.5 < Q^2 \leq 2.3$	0.098	0.079	1.862	$0.061 \pm 0.082 \pm 0.005$	$0.015 \pm 0.120 \pm 0.024$	$0.196 \pm 0.113 \pm 0.006$
$2.3 < Q^2 \leq 3.5$	0.123	0.108	2.829	$0.126 \pm 0.091 \pm 0.008$	$-0.092 \pm 0.130 \pm 0.023$	$0.040 \pm 0.130 \pm 0.005$
$3.5 < Q^2 \leq 10.0$	0.178	0.170	4.865	$0.164 \pm 0.102 \pm 0.010$	$-0.019 \pm 0.149 \pm 0.016$	$-0.076 \pm 0.149 \pm 0.013$

Table C.2: Results of the $A_{\mathrm{LL}}^{\cos(0\phi)}$, $A_{\mathrm{LL}}^{\cos \phi}$, and $A_{\mathrm{LL}}^{\cos(2\phi)}$ amplitudes of the double-spin asymmetry with statistical and systematic uncertainties and average kinematics from polarised hydrogen data for each $-t$, x_{B}, and Q^2 bin.

Appendix D

Input to the VGG Code

The extracted asymmetry amplitudes presented in this thesis are compared to calculations from the computer code [48] implementation of the VGG model outlined in Section 2.6 and Ref. [49]. It uses a Double-Distribution (DD) formalism of Generalised Parton Distributions (GPDs) from Ref. [50] with a Regge-inspired t-dependence, and the b-parameter which controls the dependence on ξ. This b-parameter is varied between 1 and 9 $i.e.$ between unity and ∞, in the computer code. The Wandzura-Wilczek (WW) approximation is chosen to include twist–3 contributions. The amplitudes presented in this thesis, which are mainly sensitive to polarised GPD $\widetilde{H}$ at HERMES kinematics, are not particularly sensitive to the D term. However, this has been included to provide as comprehensive a theoretical prediction as possible.

The input parameters used in this thesis were chosen from those which best described data that were previously published by HERMES. These are:

- **4**: 2-body doubly-polarised cross-sections for (D)DVCS using a polarised lepton beam and a polarised target

- **3**: Bethe-Heitler + DVCS contribution

- **1**: Proton target

- **36**: GPD Model: ξ-dependent parametrisation with MRST02 NNLO distribution

- **2**: Evolution with scale Q^2 rather than fixed $Q^2 = 2\,\mathrm{GeV}^2$

- **1 and 9**: b_{valance} - valence quark contribution

- **1 and 9**: b_{sea} - sea quark contribution

- **1**: Factorised model for t-dependence

  2: Regge-inspired ansatz for t-dependence with $\alpha' = 0.8$

- **0**: Exclude D term

  1: Include D term

- **2**: Evaluate GPD E using Double-Distribution (DD) and D term

- **2**: Model for the DD part of GPD E considering valence quark contributions

- **0.2**: J_u value from lattice QCD

- **0.0**: J_d value from lattice QCD

- **1**: Evaluate the π^0 pole contribution, i.e. GPD $\widetilde{E}$

- **2**: Include twist-3 corrections in WW-approximation (*i.e.* correlations between antiquarks, gluons and quarks in the nucleon)

- **1**: Include GPD $\widetilde{H}$

- **3**: Proton polarised along z-axis (along the direction of the virtual photon) *i.e.* longitudinally polarised

- **2**: Positron beam (HERMES)

- **27.57**: Beam energy in GeV

- **3**: Cross-sections extracted as a function of ϕ

- **2.459**: Average Q^2 value from data

- **0.096**: Average x_{B} value from data

- **0.0**: Average Q_0^2 value from data - DDVCS only

- **0.115**: Average $-t$ value from data

- **0**: ϕ_{start} in degrees

- **10**: ϕ_{step} in degrees

- **180**: ϕ_{end} in degrees
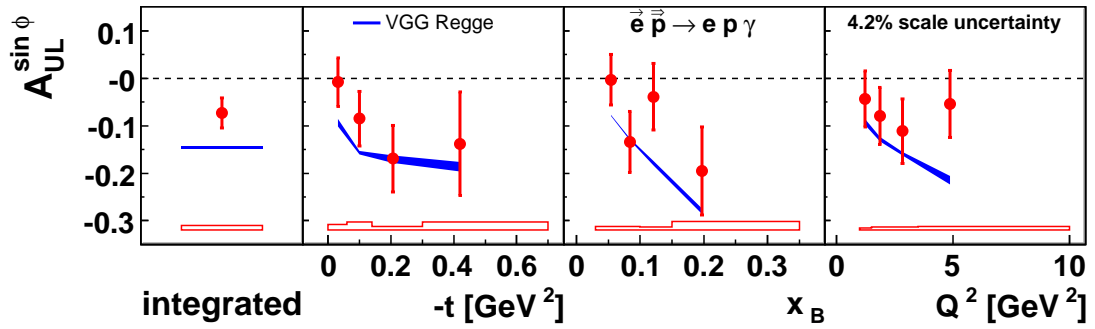
Appendix E

Single Panel and Overview Plots
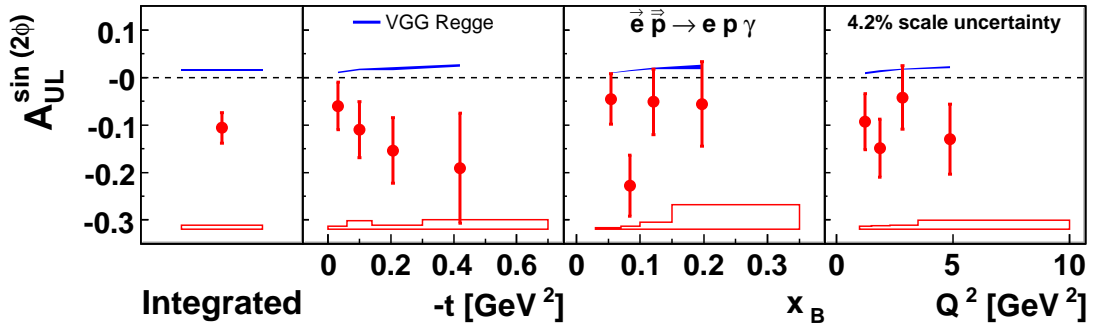

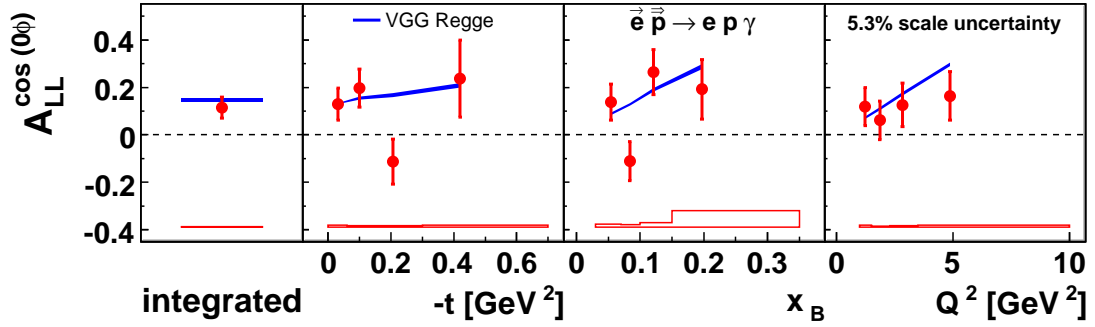**Figure E.1:** $A_{\mathrm{UL}}^{\sin\phi}$ amplitude.

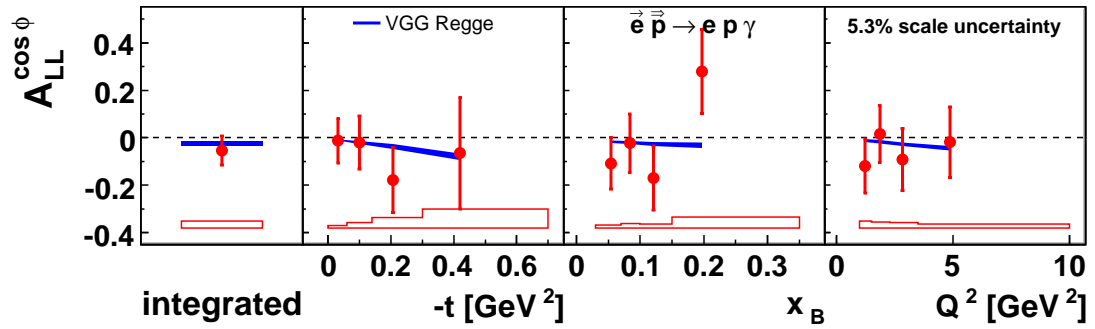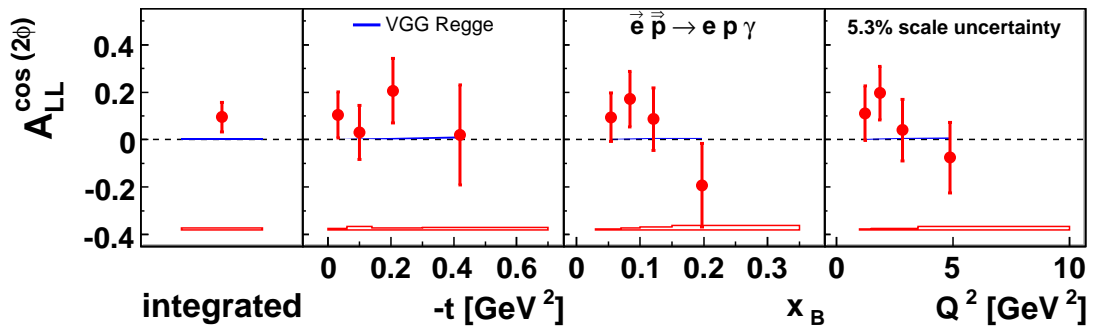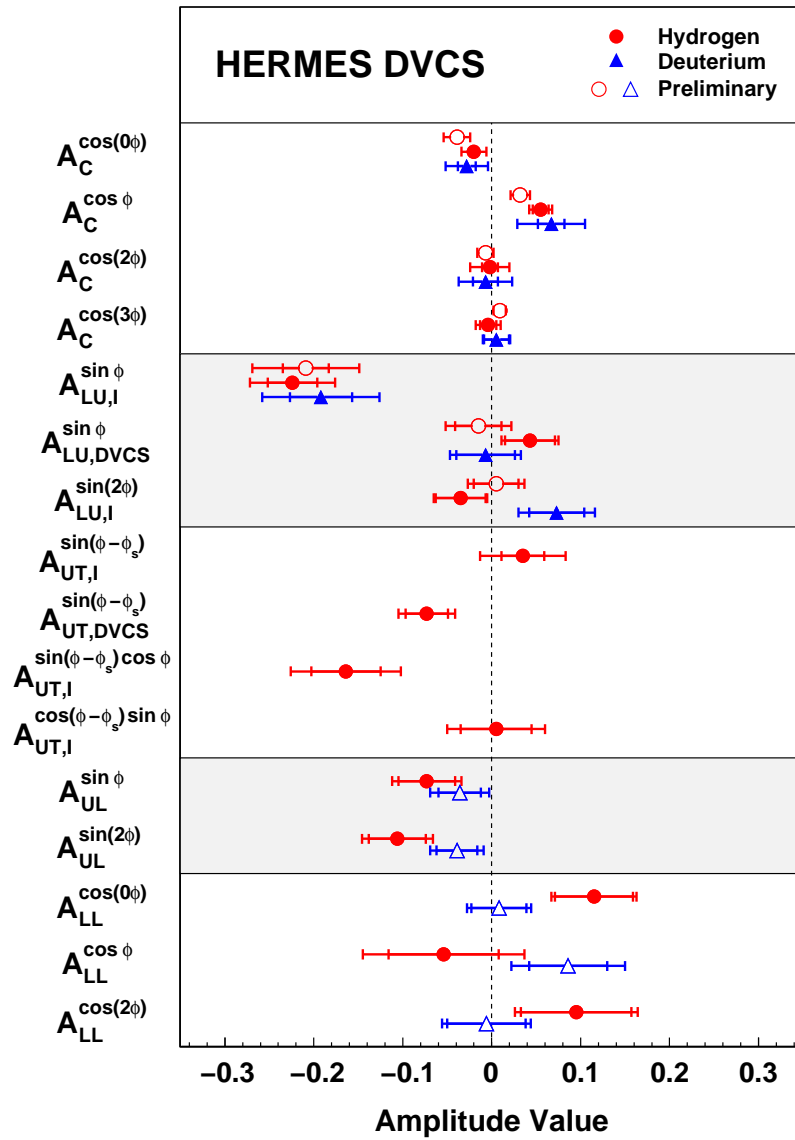**Figure E.2:** $A_{\mathrm{UL}}^{\sin(2\phi)}$ amplitude.

Figure E.3: $A_{LL}^{\cos(0\phi)}$ amplitude.

Figure E.4: $A_{LL}^{\cos\phi}$ amplitude.

Figure E.5: $A_{LL}^{\cos(2\phi)}$ amplitude.

Figure E.6: Overview of recent HERMES DVCS-related results. All amplitudes have been previously presented in Figs. 3.4 and 7.6, with the exception of the preliminary hydrogen results from Ref. [116].

Bibliography

[1] D. M. Dennison, *A Note on the Specific Heat of the Hydrogen Molecule, Proc. R. Soc.* **115** (1927) 483.

[2] R. P. Feynman, *Very high-energy collisions of hadrons, Phys. Rev. Lett.* **23** (1969) 1415.

[3] X. Ji, *Gauge-Invariant Decomposition of Nucleon Spin, Phys. Rev. Lett.* **78** (1997) 610.

[4] R. L. Jaffe and A. Manohar, *The g_1 problem: Deep inelastic electron scattering and the spin of the proton, Nucl. Phys.* **B337** (1990) 509.

[5] S. V. Bashinsky and R. L. Jaffe, *Quark and gluon orbital angular momentum and spin in hard processes, Nucl. Phys.* **B536** (1998) 303.

[6] M. Burkardt and B. C. Hikmat, *Angular Momentum Decomposition for an Electron, Phys. Rev.* **D79** (2009) 071501.

[7] **European Muon** Collaboration, J. Ashman *et al.*, *A measurement of the spin asymmetry and determination of the structure function g_1 in deep inelastic muon proton scattering, Phys. Lett.* **B206** (1988) 364.

[8] **European Muon** Collaboration, J. Ashman *et al.*, *An investigation of the spin structure of the proton in deep inelastic scattering of polarized muons on polarized protons, Nucl. Phys.* **B328** (1989) 1.

[9] **HERMES** Collaboration, *Technical Design Report, HERMES Internal Report* (1993) 93–021.

[10] E. Leader and M. Anselmino, *A Crisis In The Parton Model: Where, Oh Where Is The Proton's Spin?, Z. Phys.* **C41** (1988) 239.

[11] **HERMES** Collaboration, A. Airapetian *et al.*, *Quark helicity distributions in the nucleon for up, down, and strange quarks from semi-inclusive deep-inelastic scattering*, Phys. Rev. **D71** (2005) 012003.

[12] **HERMES** Collaboration, A. Airapetian *et al.*, *Precise determination of the spin structure function g_1 of the proton, deuteron and neutron*, Phys. Rev. **D75** (2007) 012007.

[13] R. Kaiser. Private Communication.

[14] U. Elschenbroich. HERMES Internal.

[15] F. M. Dittes *et al.*, *The Altarelli-Parisi Kernel as Asymptotic Limit of an Extended Brodsky-Lepage Kernel*, Phys. Lett. **B209** (1988) 325.

[16] D. Müller *et al.*, *Wave Functions, Evolution Equations and Evolution Kernels from Light-Ray Operators of QCD*, Fortschr. Phys. **42** (1994) 101.

[17] X. Ji, *Off-forward parton distributions*, J. Phys. **G24** (1998) 1181.

[18] A. V. Radyushkin, *Scaling limit of deeply virtual compton scattering*, Phys. Lett. **B380** (1996) 417.

[19] M. Diehl, *Generalized parton distributions*, Phys. Rept. **388** (2003) 41.

[20] **HERMES** Collaboration, A. Airapetian *et al.*, *Measurement of the Beam-Spin Azimuthal Asymmetry Associated with Deeply-Virtual Compton Scattering*, Phys. Rev. Lett. **87** (2001) 182001.

[21] **HERMES** Collaboration, A. Airapetian *et al.*, *Beam-charge azimuthal asymmetry and deeply virtual Compton scattering*, Phys. Rev. D **75** (2007) 011103.

[22] **HERMES** Collaboration, A. Airapetian *et al.*, *Measurement of Azimuthal Asymmetries With Respect To Both Beam Charge and Transverse Target Polarization in Exclusive Electroproduction of Real Photons*, JHEP **06** (2008) 066.

[23] **HERMES** Collaboration, A. Airapetian *et al.*, *Separation of contributions from deeply virtual Compton scattering and its interference with the Bethe–Heitler process in measurements on a hydrogen target*, JHEP **11** (2009) 083.

[24] **HERMES** Collaboration, A. Airapetian *et al.*, *Measurement of azimuthal asymmetries associated with deeply virtual Compton scattering on an unpolarized deuterium target, Nucl. Phys.* **B829** (2010) 1.

[25] **HERMES** Collaboration, Airapetian *et al.*, *Nuclear mass dependence of azimuthal beam helicity and beam charge asymmetries in deeply virtual Compton scattering, Phys. Rev.* **C81** (2010) 035202.

[26] A. V. Belitsky and D. Müller, *Nucleon hologram with exclusive leptoproduction, Nucl. Phys.* **A711** (2002) 118.

[27] A. V. Belitsky, D. Müller, and A. Kirchner, *Theory of deeply virtual Compton scattering on the nucleon, Nucl. Phys.* **B629** (2002) 323.

[28] R. L. Jaffe, *Spin, twist and hadron structure in deep inelastic processes, Lectures at QCD in Erice, Italy* (1995) [`hep-ph/9602236`].

[29] M. Diehl, *Azimuthal distributions: the Simple, the Complicated and the Beautiful, Talk given at the Symposium on Hadronic Structure Physics, University of Glasgow* (2010).

[30] Y. L. Dokshitzer *Sov. Phys JETP.* **46** (1977) 641.

[31] V. N. Garibo and L. N. Lipatov *Sov. J. Nucl. Phys.* **15** (1972) 438.

[32] L. N. Lipatov *Sov. J. Nucl. Phys.* **20** (1975) 94.

[33] G. Altarelli and G. Parisi, *Asymptotic freedom in parton language, Nucl. Phys.* **B126** (1977) 298.

[34] A. V. Efremov and A. V. Radyushkin, *Factorization and asymptotic behaviour of pion form factor in QCD, Phys. Lett.* **B94** (1980) 245.

[35] G. P. Lepage and S. J. Brodsky, *Exclusive Processes in Perturbative Quantum Chromodynamics, Phys. Rev.* **D22** (1980) 2157.

[36] J. Blümlein, B. Geyer, and D. Robaschik, *The virtual Compton amplitude in the generalized Bjorken region: Twist-2 contributions, Nucl. Phys.* **B560** (1999) 283.

[37] A. V. Belitsky and D. Mueller, *Twist-three effects in two-photon processes, Nucl. Phys.* **B589** (2000) 611.

[38] A. V. Belitsky, A. Freund, and D. Muller, *Evolution kernels of skewed parton distributions: method and two-loop results*, Nucl. Phys. **B574** (2000) 347.

[39] A. V. Belitsky and D. Mueller, *Broken conformal invariance and spectrum of anomalous dimensions in QCD*, Nucl. Phys. **B537** (1999) 397.

[40] K. Kumericki and D. Mueller, *Deeply virtual Compton scattering at small x_B and the access to the GPD H*, `arXiv:0904.0458`.

[41] M. Guidal and H. Moutarde, *Generalized Parton Distributions from Deeply Virtual Compton Scattering at HERMES*, Eur. Phys. J. **A42** (2009) 71.

[42] H. Moutarde, *Extraction of the Compton form factor $\mathcal{H}$ from deeply virtual Compton scattering measurements at Jefferson Lab*, Phys. Rev. **D79** (2009) 094021.

[43] **CLAS** Collaboration, *Deeply Virtual Compton Scattering at 6 GeV with transversely polarized target using the CLAS Detector*, Jefferson Lab PAC **33** (2008) PR–08–021.

[44] **CLAS** Collaboration, *Deeply Virtual Compton Scattering with CLAS at 11 GeV*, Jefferson Lab PAC **30** (2006) PR12–06–119.

[45] **COMPASS** Collaboration, *Study of Generalized Parton Distributions (GPD) with COMPASS at CERN*, Letter of Intent (January 2009) SPSC–I–238.

[46] K. Goeke, M. V. Polyakov, and M. Vanderhaeghen, *Hard exclusive reactions and the structure of hadrons*, Prog. Part. Nuc. Phys. **47** (2001) 401.

[47] S. Wandzura and F. Wilczek, *Sum rules for spin-dependent electroproduction- test of relativistic constituent quarks*, Phys. Lett. **B72** (1977) 195.

[48] M. Guidal, M. Vanderhaeghen, and P. Guichon, *Computer code for the calculation of DVCS and BH processes in $ep \rightarrow ep\gamma$*, Private Communication (2007).

[49] M. Vanderhaeghen, P. A. M. Guichon, and M. Guidal, *Deeply virtual electroproduction of photons and mesons on the nucleon: Leading order amplitudes and power corrections*, Phys. Rev. **D60** (1999) 094017.

[50] A. V. Radyushkin, *Double distributions and evolution equations*, Phys. Rev. **D59** (1999) 014030.

[51] M. V. Polyakov and C. Weiss, *Skewed and double distributions in the pion and the nucleon*, Phys. Rev. **D60** (1999) 114017.

[52] E. R. Berger, M. Diehl, and B. Pire, *Timelike Compton scattering: Exclusive photoproduction of lepton pairs*, Eur. Phys. J. **C23** (2002) 675.

[53] M. Guidal and M. Vanderhaeghen, *Double Deeply Virtual Compton Scattering off the Nucleon*, Phys. Rev. Lett. **90** (2003) 012001.

[54] M. Guidal, *Generalized Parton Distributions and deep virtual Compton scattering*, Prog. Part. Nucl. Phys. **61** (2008) 89.

[55] K. Rith, *Spin asymmetries in deep-inelastic electron-nucleon scattering - selected HERMES results*, Prog. Part. Nuc. Phys. **49** (2002) 245.

[56] A. H. Compton, *A Quantum Theory of the Scattering of X-rays by Light Elements*, Phys. Rev. **21** (1923) 483.

[57] V. A. Korotkov and W. D. Nowak, *Future Measurements of Deeply Virtual Compton Scattering at HERMES*, Eur. Phys. J. **C23** (2002) 455.

[58] A. Bacchetta *et al.*, *Single-spin asymmetries: The Trento conventions*, Phys. Rev. **D70** (2004) 117504.

[59] F. Ellinghaus, *Beam Charge and Beam Spin Azimuthal Asymmetries in Deeply Virtual Compton Scattering*. PhD thesis, Humboldt University Berlin, 2004. DESY-THESIS-2004-005.

[60] **HERMES** Collaboration, Airapetian *et al.*, *Measurement of azimuthal asymmetries associated with deeply virtual Compton scattering on a longitudinally polarized deuterium target*, Awaiting publication (2010).

[61] M. Kopytin, *Longitudinal target-spin azimuthal asymmetry in deeply- virtual Compton scattering*. PhD thesis, Humboldt University Berlin, 2006. DESY-THESIS-2006-100.

[62] **CLAS** Collaboration, S. Stepanyan *et al.*, *Observation of Exclusive Deeply Virtual Compton Scattering in Polarized Electron Beam Asymmetry Measurements*, Phys. Rev. Lett. **87** (2001) 182002.

[63] D. Zeiler, *Deeply Virtual Compton Scattering off an Unpolarized Hydrogen Target at the HERMES Experiment.* PhD thesis, University of Erlangen-Nürnberg. DESY-THESIS-2009-024.

[64] G. D. Hill, *Deeply virtual compton scattering off unpolarised deuterium at HERMES.* PhD thesis, University of Glasgow. DESY-THESIS-2008-035.

[65] Z. Ye, *Transverse target-spin asymmetry associated with deeply virtual Compton scattering on the proton and a resulting model-dependent constraint on the total angular momentum of quarks in the nucleon.* PhD thesis, University of Hamburg. DESY-THESIS-2007-005.

[66] M. J. Murray, *DVCS at HERMES: The recoil detector and transverse target spin asymmetries.* PhD thesis, University of Glasgow. DESY-THESIS-2008-006.

[67] M. Dueren, *The HERMES experiment: From the design to the first results.* PhD thesis. DESY-THESIS-1995-002.

[68] A. A. Sokolov and I. M. Ternov, *On Polarization and Spin Effects in Synchrotron Radiation Theory, Sov. Phys. Doklady* **8** (1964) 1203.

[69] E. C. Aschenauer. HERMES Internal.

[70] D. Barber *et al.*, *The HERA polarimeter and the first observation of electron spin polarization at HERA, Nucl. Instrum. Meth.* **A329** (1993) 79.

[71] J. Buon and K. Steffen, *HERA variable-energy spin rotator and head-on ep collision scheme with choice of electron helicity, Nucl. Instrum. Meth.* **A245** (1986) 248.

[72] W. Lorenzon. HERMES Internal.

[73] M. Beckmann *et al.*, *The Longitudinal Polarimeter at HERA, Nucl. Instrum. Meth.* **A479** (2002) 334.

[74] T. Benisch *et al.*, *The luminosity monitor of the HERMES experiment at DESY, Nucl. Instrum. Meth.* **A471** (2001) 314.

[75] **HERMES** Collaboration, *Shift Primer, DESY Internal Note* (2007).

[76] P. Lenisa. HERMES Internal.

[77] **HERMES** Collaboration, A. Airapetian *et al.*, *The HERMES Polarized Hydrogen and Deuterium Gas Target in the HERA Electron Storage Ring*, Nucl. Instrum. Meth. **A540** (2005) 68.

[78] A. Nass *et al.*, *The HERMES Polarized Atomic Beam Source*, Nucl. Instrum. Meth. **A505** (2003) 633.

[79] C. Baumgarten *et al.*, *An atomic beam polarimeter to measure the nuclear polarization in the HERMES gaseous polarized hydrogen and deuterium target*, Nucl. Instrum. Meth. **A482** (2002) 606.

[80] C. Baumgarten *et al.*, *A gas analyzer for the internal polarized target of the HERMES experiment*, Nucl. Instrum. Meth. **A508** (2003) 268.

[81] C. Baumgarten *et al.*, *Measurements of atomic recombination in the HERMES polarized hydrogen and deuterium storage cell target*, Nucl. Instrum. Meth. **A496** (2003) 263.

[82] B. Tipton, *Analysis of Positron Beam Polarization Measured by the Transverse Polarimeter in 1997*, HERMES Internal Report (1998) 98–090.

[83] M. Beckmann, *Target polarisation values and their uncertainties used by the Δq analysis group for the 1996 to 2000 running periods*, HERMES Internal Report (2003) 03–005.

[84] **HERMES** Collaboration, K. Ackerstaff *et al.*, *The HERMES Spectrometer*, Nucl. Instrum. Meth. **A417** (1998) 230.

[85] J. J. M. Steijger *et al.*, *The lambda wheels, a silicon vertex detector for HERMES*, Nucl. Instrum. Meth. **A453** (2000) 98.

[86] D. Ryckbosch *et al.*, *The HERMES RICH detector*, Nucl. Instrum. Meth. **A433** (1999) 98.

[87] U. Elschenbroich and E. C. Aschenauer. HERMES Internal.

[88] R. Kaiser, *Particle Identification at HERMES*, HERMES Internal Report (1997) 97–025.

[89] D. de Schepper *et al.*, *The HERMES Čerenkov Detector*, HERMES Internal Report (2000).

[90] G. Charpak *et al.*, *The use of multiwire proportional counters to select and localize charged particles*, *Nucl. Instrum. Meth.* **A62** (1968) 262.

[91] R. B. Kaiser, *Measurement of the spin structure of the neutron using polarised deep inelastic scattering.* PhD thesis, Simon Fraser University, 1997. DESY-THESIS-1997-017.

[92] H. Avakian *et al.*, *Performance of the electromagnetic calorimeter of the HERMES experiment*, *Nucl. Instrum. Meth.* **A417** (1998) 69.

[93] A. Andreev *et al.*, *Multiwire Proportional Chambers in the HERMES Experiment*, *HERMES Internal Report* (1998) 98–012.

[94] G. Rakness, *Study of Front Drift Chanmber Resolution and Efficiencies*, *HERMES Internal Report* (1998) 98–037.

[95] W. Wander, *Reconstruction of High Energy Scattering Events in the HERMES Experiment.* PhD thesis, University of Erlangen-Nürnberg, 1997. DESY-THESIS-1997-031.

[96] **HERMES** Collaboration, *HERMES Recoil Detector*, *Technical Design Report* (2003).

[97] X.-G. Lu, *The Maximum Likelihood Estimation Method*, *Lecture at HERMES DVCS Week, unpublished* (2007).

[98] W. T. Eadie, D. Drijard, and F. E. James, *Statistical methods in experimental physics.* Amsterdam: North-Holland, 1971.

[99] **HERMES** Collaboration, A. Airapetian *et al.*, *Exclusive Leptoproduction of Real Photons on a Longitudinally Polarised Hydrogen Target*, *JHEP* **06** (2010) 019.

[100] X. Lu and Z. Ye, *Simultaneous Extraction of the BSAs and the BCA Associated with DVCS with the Extended Maximum Likelihood Method*, *HERMES Internal Report* (2007) 07–001.

[101] **CLAS** Collaboration, B. A. Mecking *et al.*, *The CEBAF large acceptance spectrometer (CLAS)*, *Nucl. Instrum. Meth.* **A503** (2003) 513.

[102] W. Wander, *DAD-Distributed ADAMO Database System at HERMES*, *Proceedings of CHEP95, Rio de Janeiro* (1995).

[103] B. Krauss, *Deeply virtual Compton scattering and the HERMES recoil- detector.* PhD thesis, University of Erlangen-Nürnberg. DESY-THESIS-2005-008.

[104] P. A. Nylander, *A Systematic Method for Unbinned Fitting and Statistical Analysis*, *Ohio University Internal Report* (1997).

[105] A. V. Afanasev, M. I. Kochatnij, and N. P. Merekov, *Single-Spin Asymmetries in the Bethe-Heitler process $e^- + p \to e^- + \gamma + p$ Induced by Loop Corrections*, *JETP* **102** (2006) 220.

[106] F. W. Brasse *et al.*, *Parametrization of the q^2 dependence of $\gamma_v p$ total cross sections in the resonance region*, *Nucl. Phys.* **B110** (1976) 413.

[107] D. Drechsel, O. Hanstein, S. S. Kamalov, and L. Tiator, *A unitary isobar model for pion photo- and electroproduction on the proton up to 1-GeV*, *Nucl. Phys.* **A645** (1999) 145.

[108] B. Krauss, *Statistical Errors and Monte Carlo*, *HERMES Internal Report* (2005) 05–023.

[109] S. V. Goloskokov and P. Kroll, *The target asymmetry in hard vector-meson electroproduction and parton angular momenta*, *Eur. Phys. J.* **C59** (2009) 809.

[110] A. Vandenbroucke, *Exclusive pi0 production at HERMES: Detection - simulation - analysis.* PhD thesis, University of Gent, 2007. DESY-THESIS-2007-003.

[111] C. Amsler *et al.*, *The review of particle physics*, *Phys. Lett.* **B667** (2008) 1.

[112] M. Diehl and S. Sapeta, *On the analysis of lepton scattering on longitudinally or transversely polarized protons*, *Eur. Phys. J.* **C41** (2005) 515.

[113] A. Movsisyan, *Deeply Virtual Compton Scattering off a Deuterium Target at the HERMES Experiment.* PhD thesis, Yerevan Physics Institute, 2010 (in preparation).

[114] **CLAS** Collaboration, S. Chen *et al.*, *Measurement of Deeply Virtual Compton Scattering with a Polarized-Proton Target*, *Phys. Rev. Lett.* **97** (2006) 072002.

[115] **CLAS** Collaboration, *Deeply Virtual Compton Scattering at 6 GeV with Polarized Target and Polarised Beam using the CLAS Detector*, *Jefferson Lab PAC* **28** (2001) PR05–114.

[116] J. Burns, *Deeply virtual compton scattering off an unpolarised hydrogen target at HERMES*. PhD thesis, University of Glasgow, 2010 (in preparation).

[117] M. Guidal, *Generalized Parton Distributions from Deep Virtual Compton Scattering at CLAS*, `arXiv:1003.0307`.

[118] M. Guidal, *Constraints on the $\tilde{H}$ Generalized Parton Distribution from Deep Virtual Compton Scattering Measured at HERMES*, `arXiv:1005.4922`.